

Diss. ETH No. 14489

A NEW APPROACH
TO
LONGITUDINALLY DETECTED
ELECTRON PARAMAGNETIC RESONANCE

DISSERTATION

submitted to the

SWISS FEDERAL INSTITUTE OF TECHNOLOGY
ZÜRICH

for the degree of

DOCTOR OF NATURAL SCIENCES

presented by

JOSEF GRANWEHR

Dipl. Chem. ETH

born December 24, 1971

citizen of Gaiserwald (SG)

accepted on the recommendation of
Prof. Dr. Arthur SCHWEIGER, examiner
Prof. Dr. Beat H. MEIER, co-examiner

Zürich, 2002

Für meine Mutter

Contents

| | |
|--|-----------|
| Symbols and Abbreviations | v |
| Abstract | ix |
| Zusammenfassung | xi |
| 1 Introduction | 1 |
| 2 EPR Basics | 7 |
| 2.1 The Electron Spin | 7 |
| 2.2 Quantum Mechanical Description of EPR | 8 |
| 2.3 Microscopic versus Macroscopic Interpretation | 9 |
| 2.4 Excitation of a Spin System | 11 |
| 2.4.1 Effect of an Alternating Magnetic Perturbation | 11 |
| 2.4.2 Ideal Pulse Experiment | 13 |
| 2.5 Relaxation | 14 |
| 2.5.1 Definitions | 14 |
| 2.5.2 Bloch Equations | 15 |
| 2.5.3 Longitudinal Relaxation in Solids | 17 |
| 2.5.4 Transverse Relaxation in Solids | 18 |
| 2.5.5 Diffusion Processes Contributing to Relaxation | 19 |
| 2.5.6 Problems of Relaxation Studies | 20 |
| 2.5.7 Measurement of Longitudinal Relaxation Times | 21 |

| | | |
|----------|---|-----------|
| 3 | Introduction to Longitudinal Detection | 27 |
| 3.1 | Principle of LOD | 27 |
| 3.2 | Simulation of the Detector | 28 |
| 3.3 | Theoretical Description of LOD Experiments | 30 |
| 3.3.1 | Quantum Mechanical Approach | 31 |
| 3.3.2 | Classical Description Assuming Fast Relaxation | 33 |
| 3.3.3 | Classical Description Assuming Low Modulation Depth | 36 |
| 3.4 | Instrumentation Used for LOD EPR | 41 |
| 3.4.1 | Generation of an Amplitude Modulated MW Field | 41 |
| 3.4.2 | Resonator and Pick-up Coil | 42 |
| 3.4.3 | Detector | 43 |
| 3.5 | Applications of LOD | 43 |
| 3.5.1 | Relaxation Time Measurements | 43 |
| 3.5.2 | EPR Measurements | 46 |
| 3.5.3 | LOD ESEEM | 48 |
| 3.5.4 | Conceptual Studies | 48 |
| 3.5.5 | EPR Imaging with LOD | 49 |
| 4 | Instrumentation | 51 |
| 4.1 | Spectrometer | 52 |
| 4.1.1 | Pulse Excitation | 52 |
| 4.1.2 | Continuous Wave Excitation | 52 |
| 4.2 | Probehead and Resonator | 52 |
| 4.3 | Detection Setup | 55 |
| 4.3.1 | Resonant Circuit | 55 |
| 4.3.2 | Impedance Matching | 56 |
| 4.3.3 | Rf Preamplifier | 57 |
| 4.3.4 | Recording Device | 57 |
| 4.4 | Quantization of the B_1 Inhomogeneity | 58 |
| 4.4.1 | Distribution of B_1 Over the Sample Volume | 58 |
| 4.4.2 | Deriving an Analytical Expression for the Spin Nutation | 60 |
| 4.5 | Sensitivity | 62 |
| 4.5.1 | Signal-to-Noise Ratio | 62 |

| | | |
|----------|---|------------|
| 4.5.2 | Number of Spins | 63 |
| 4.5.3 | Comparison Between Pulse and CW LOD Experiments . . | 64 |
| 5 | Measuring Polarization With Pulse LOD | 67 |
| 5.1 | Building Blocks for the Detection of Polarization | 67 |
| 5.1.1 | Short MW Pulse | 67 |
| 5.1.2 | Nutation Pulse | 69 |
| 5.1.3 | Refocused Nutation Pulse | 70 |
| 5.1.4 | B_1 Cycle | 73 |
| 5.2 | Signal Recording and Data Processing | 75 |
| 5.2.1 | Collecting Data with a Transient Recorder | 75 |
| 5.2.2 | Analysis of Transient Data | 76 |
| 5.2.3 | Collecting Data with a Boxcar Integrator | 77 |
| 5.2.4 | Signal Processing with a Lock-In Amplifier | 77 |
| 5.3 | Time-Resolved Polarization Measurement | 77 |
| 5.3.1 | Procedure | 78 |
| 5.3.2 | Experimental Example | 80 |
| 5.3.3 | Discussion of the Results | 84 |
| 6 | Field-Swept EPR Measurements | 87 |
| 6.1 | Transient-Nutation LOD EPR | 87 |
| 6.1.1 | Principle of the Experiment | 87 |
| 6.1.2 | Microwave Power Dependence of the Signal | 91 |
| 6.1.3 | Variation of the Detection Frequency | 93 |
| 6.2 | Pulse-Train LOD EPR | 94 |
| 6.3 | CW LOD EPR Methods | 97 |
| 7 | Spin-Lattice Relaxation Time Measurement | 101 |
| 7.1 | Data Processing | 101 |
| 7.1.1 | Determination of Relaxation Times by Curve Fitting . . . | 102 |
| 7.1.2 | Inversion of Multi-Exponential Decay Data | 103 |
| 7.1.3 | Selection of Analysis Method | 104 |
| 7.1.4 | Data Refinement | 105 |

| | | |
|----------|---|------------|
| 7.2 | Inversion and Saturation Recovery | 108 |
| 7.2.1 | Principle and Realization | 108 |
| 7.2.2 | Experimental Examples | 113 |
| 7.3 | Direct Measurement of T_1 | 116 |
| 8 | Outlook | 119 |
| 8.1 | Instrumentation | 119 |
| 8.2 | CW LOD EPR | 122 |
| 8.3 | Pulse LOD EPR | 123 |
| A | Forced Harmonic Oscillation of a Serial LCR Circuit | 125 |
| B | B_1 Field Distribution in a Dielectric Ring Resonator | 129 |
| C | Signal-to-Noise Ratio of CW LOD EPR | 135 |
| C.1 | Time Evolution of M_z | 135 |
| C.2 | Signal Induced by a Magnetization Changing in Time | 137 |
| C.3 | Detector Noise | 139 |
| C.4 | Signal-to-Noise Ratio | 139 |
| | References | 141 |
| | Index | 147 |
| | Acknowledgement | 151 |
| | Curriculum Vitae | 155 |

Symbols

Variables

| | |
|------------------|---|
| A | hyperfine interaction matrix |
| A | cross-sectional area of the detection coil |
| A_w | cross-sectional area of the wire used for the detection coil |
| a | saturation factor |
| B | magnetic field vector |
| B_0 | amplitude of static magnetic field |
| ΔB_0 | field offset |
| B_1 | amplitude of microwave field in [T] |
| \tilde{B}_1 | time-dependent amplitude of modulated mw field |
| B_{eff} | effective field |
| C | total capacitance of the detection circuit |
| D | zero-field splitting tensor, dipolar coupling tensor |
| d | ratio between the maximum and the minimum B_1 field on a sample |
| E | energy |
| F | noise figure |
| \mathcal{H} | Hamiltonian or total energy operator of a system |
| h | height of a sample fraction in the resonator |
| I | spin quantum number of the nuclear spin |
| J | total angular momentum |
| J | exchange coupling constant |
| k | resonator constant characterizing the B_1 distribution |
| L | inductance of the detection coil |
| M | vector of macroscopic magnetization (M_x, M_y, M_z) |
| M_0 | macroscopic magnetization at Boltzmann equilibrium |
| M_z | macroscopic longitudinal magnetization |
| m | modulation ratio |
| m_S | magnetic quantum number of the electron spin |
| N | number of spins |
| \mathcal{N} | noise (in an S/N calculation) |

| | |
|-------------------|--|
| n | generally used for sums or number of turns of detection coil, depending on context |
| \mathbf{P} | nuclear quadrupole tensor |
| p | probability |
| Q_l | loaded quality factor of the mw resonator |
| Q_{Ξ} | loaded quality factor of the resonant circuit |
| \mathbf{R} | relaxation matrix |
| R_S | serial resistance |
| R_P | shunt resistance |
| \mathbf{r}_{jk} | radius vector connecting two spins j and k |
| r_{jk} | distance between two spins j and k |
| \mathbf{S} | quantum mechanical angular momentum |
| S | spin quantum number of the electron spin |
| S | signal (in an S/N calculation) |
| s | measured signal in an experiment |
| T | evolution time or temperature, depending on context |
| T_1 | longitudinal relaxation time |
| T_2 | transverse relaxation time |
| T_S | sample temperature |
| T_m | phase memory time of electron spins |
| T_{Ξ} | modulation period of the resonant circuit |
| t_d | instrumental deadtime |
| t_p | pulse length |
| t_s | shot repetition time |
| t_w | length of the detection window |
| V | volume or voltage, depending on context |
| V_C | volume of the detection coil |
| V_{Ξ} | voltage across the capacitor C |
| V_{ind} | voltage induced in the detection coil |
| V_S | volume of the sample |
| w | weight function |
| Z | partition function |

| | |
|----------------------|---|
| β | rotation angle of mw pulse ('flip angle') or inverse spin temperature, depending on context |
| χ_0 | magnetic susceptibility |
| Δ | generally used for differences or Weiss constant, depending on context |
| ϵ | amplitude of modulated part of $M_z(t)$ in a cw LOD EPR experiment |
| μ | magnetic moment |
| Ω_S | frequency offset of the electron spin with respect to carrier frequency |
| Ω_m | difference between the two frequencies in an experiment with double irradiation |
| ω_1 | amplitude of microwave field in angular frequency units |
| ω_S | resonance frequency of the electron spin |
| ω_d | detection frequency |
| ω_{mw} | frequency of the exciting magnetic field |
| ω_{Ξ} | resonance frequency of the detection circuit |
| φ | signal phase |
| ψ | signal-to-noise ratio |
| σ | normalized density operator of a spin system |
| σ_0 | normalized density operator at Boltzmann equilibrium |
| τ_p | interpulse delay |
| τ_{Ξ} | time constant of the detection circuit |
| θ | angle between \mathbf{B}_{eff} and \mathbf{B}_0 |

Physical Constants

| | |
|-----------|--|
| g_e | g value of the free electron, 2.002319315 |
| h | Planck's constant (quantum of action), 6.626176×10^{-34} Js |
| \hbar | $\hbar = h/2\pi$ |
| k | Boltzmann constant, 1.380662×10^{-23} JK ⁻¹ |
| β_e | electron Bohr magneton, $9.2740154 \times 10^{-24}$ JT ⁻¹ |
| β_n | nuclear Bohr magneton, $5.0507866 \times 10^{-27}$ JT ⁻¹ |
| μ_0 | magnetic permeability of vacuum, $4\pi \times 10^{-7}$ Vs/Am |

Abbreviations

| | |
|--------------|--|
| AFG | arbitrary function generator |
| cw | continuous wave |
| DC | direct current |
| DPPH | α,α -diphenyl- β -picrylhydrazyl |
| eff | effective |
| EPR | electron paramagnetic resonance |
| ELDOR | electron-electron double resonance |
| ENDOR | electron nuclear double resonance |
| ESEEM | electron spin echo envelope modulation |
| EZ | electron Zeeman |
| FID | free induction decay |
| FT | Fourier transformation |
| fwhh | full width at half height |
| HFI | hyperfine interaction |
| hwhh | half width at half height |
| IR | inversion-recovery |
| IR-LOD T_1 | inversion-recovery LOD T_1 measurement |
| LOD | longitudinal detection or longitudinally detected |
| mav | moving average |
| mw | microwave |
| NMR | nuclear magnetic resonance |
| PEANUT | phase-inverted echo-amplitude detected nutation |
| PSD | phase-sensitive detector (usually a lock-in amplifier) |
| PT-LOD EPR | pulse-train excited longitudinally detected EPR |
| rf | radio frequency |
| S/N | signal-to-noise ratio |
| SR | saturation-recovery |
| SR-LOD T_1 | saturation-recovery LOD T_1 measurement |
| TN-LOD EPR | transient nutation longitudinally detected EPR |
| TWT | traveling-wave tube |

Abstract

This study presents an attempt to review and extend the possibilities with longitudinal detection (LOD) in EPR spectroscopy. Based on a novel instrumental setup, new pulse sequences for the detection of spin polarization are designed. These pulse schemes are then used to record field-swept EPR spectra and for the time-dependent determination of polarization in relaxation time measurements.

Setup. The first goal is the design of a new setup based on a commercially available spectrometer and probehead. It should be sensitive enough for routine measurements as well as sufficiently versatile that different classes of LOD experiments can be performed. The Bruker X-band pulse EPR spectrometer, equipped with an ElexSys console and an ENDOR probehead, is well suited for this task. If this probehead is rotated by 90° about the axis of the sample tube, the ENDOR coils are oriented along the direction of the polarizing magnetic field, and they can be directly used to measure spin magnetization changing in time. Because the dielectric ring resonator built into this probehead has a high quality factor if it is critically coupled, this setup can be used not only for pulse LOD EPR, but with few modifications also for continuous wave (cw) LOD EPR measurements.

Pulse LOD Applications. Two new pulse experiments for the measurement of field-swept EPR spectra are presented, the *transient nutation longitudinally detected EPR* (TN-LOD EPR) and the *pulse-train excited longitudinally detected EPR* (PT-LOD EPR) experiment. Longitudinally detected EPR spectra have in different aspects complementary properties than transversely detected cw EPR spectra. The most obvious one is that absorption spectra rather than their first derivatives are measured. Thus, there are no baseline problems with broad lines, and it is possible to measure samples with broad as well as narrow lines in the same spectrum. Another point is a different relaxation time dependence of the signal intensity of the two detection methods. In certain cases, this can be used to separate spectra of a sample mixture.

Relaxation time measurements. The most evident application of LOD is the measurement of spin-lattice relaxation times (T_1). This is often a difficult task with conventional detection techniques, especially since the temperature dependence is

one of the most important information sources of relaxation times. With LOD the range of T_1 that can be measured is increased considerably compared to the conventional methods, mainly for transition metal complexes with inhomogeneously broadened lines. Two experiments are proposed for this task. First the well-known inversion-recovery (IR) and saturation-recovery (SR) experiments are combined with an LOD polarization detector. Second it is shown how the signal that is induced directly by the relaxing magnetization can be recorded using a detection circuit with a high quality factor.

Zusammenfassung

In der EPR-Spektroskopie wurden diverse alternative Detektionsmethoden entwickelt, um die Nachteile der allgemein gebräuchlichen transversalen Detektion der Spinmagnetisierung zu umgehen. Eine der in der Literatur am häufigsten diskutierten Methoden ist die Verwendung einer Spule oder eines Spulenpaars, deren Achse parallel zum polarisierenden Magnetfeld ausgerichtet ist. Dies wird als z - oder longitudinale Detektion (LOD) bezeichnet. Die Eigenschaften dieser Art der Signalaufnahme sind zu einem grossen Teil komplementär zur konventionellen Methode, weshalb auch die Stärken und die Schwächen der beiden Ansätze bei unterschiedlichen Anwendungen zu finden sind. Der wichtigste Grund, warum LOD bisher nur in wenigen Arbeiten verwendet wurde, liegt in erster Linie darin, dass eigens für dieses Experiment konstruierte Spektrometer und Probenköpfe benötigt wurden. Deren Empfindlichkeit reichte im allgemeinen nicht aus, um die Methode für Routineanwendungen zu empfehlen.

In der vorliegenden Arbeit wird zunächst ein neuer Aufbau zur longitudinalen Detektion vorgestellt. Um dessen spezielle Eigenschaften bestmöglichst auszunützen, werden Pulssequenzen zur Detektion der Spinpolarisation darauf optimiert, welche verwendet werden zur Messung feldgesweepter EPR-Spektren sowie zur Bestimmung der Zeitabhängigkeit der Polarisation in Relaxationszeitmessungen.

Setup. Das erste Ziel dieser Arbeit ist es nun, einen Aufbau basierend auf einem kommerziell erhältlichen Spektrometer und Probenkopf zu realisieren, der empfindlich genug ist, um routinemässig Messungen durchführen zu können, und der trotzdem für unterschiedliche Anwendungen verwendet werden kann. Sehr gut geeignet für diese Aufgabe ist das Bruker X-Band Puls-EPR-Spektrometer, ausgerüstet mit einer ElexSys-Konsole, sowie der ENDOR-Probenkopf von der gleichen Firma. Wenn dieser um 90° um die Achse des Probenröhrchens gedreht wird, dann ist das ENDOR-Spulenpaar in z -Richtung orientiert, und man kann es direkt verwenden zur Messung einer sich zeitlich ändernden Magnetisierung. Da der verwendete dielektrische Resonator bei kritischer Kopplung eine hohe Güte besitzt, kann dieses Setup mit relativ wenig Änderungen auch für continuous wave (cw) LOD Messungen verwendet werden, wie sie bereits seit langem bekannt sind.

Puls LOD Anwendungen. Um die speziellen Eigenschaften dieses Aufbaus optimal auszunutzen, werden zwei neue Pulsmethoden vorgestellt – *transient nutation longitudinally detected EPR* (TN-LOD EPR) sowie *pulse-train excited longitudinally detected EPR* (PT-LOD EPR) – mit denen die Spinnmagnetisierung ausgelesen werden kann. Diese Sequenzen eignen sich zum einen zur Aufnahme von feld-gesweepen EPR-Spektren, können aber auch als Detektionssequenzen verwendet werden bei der Bestimmung von longitudinalen Relaxationszeiten. Die longitudinal detektierten Puls-EPR-Spektren haben etwas andere Eigenschaften als herkömmliche cw ERP-Spektren. Zum einen misst man das Absorptionsspektrum und nicht die erste Ableitung davon. Somit hat man keine Basislinienprobleme bei sehr breiten Spektren, und es ist möglich, Proben mit stark variierenden Linienbreiten in einer einzigen Messung zu charakterisieren. Zum anderen ist die Abhängigkeit des Signals von den Relaxationszeiten bei den beiden Methoden unterschiedlich, womit durch Vergleich der beiden Messungen unter Umständen sich überlagernde Signale aufgetrennt werden können.

Relaxationszeitmessungen. Die vielleicht wichtigste Anwendung von LOD ist die Bestimmung von Spin-Gitter-Relaxationszeiten (T_1). Während es zur Charakterisierung der magnetischen Eigenschaften einer Substanz im allgemeinen ohne Verzerrung der Resultate möglich ist, die Messung bei sehr tiefen Temperaturen durchzuführen, ist einer der wichtigsten Informationsträger bei Relaxationszeiten deren Temperaturabhängigkeit. T_1 von Übergangsmetallkomplexen kann mit den bisher gebräuchlichen Methoden oft nur bei tiefen Temperaturen bestimmt werden. Falls die Relaxationskurve nicht durch eine monoexponentielle Funktion beschrieben werden kann oder das Spektrum stark inhomogen verbreitert ist, so dass es nicht möglich ist, cw-Methoden zur T_1 -Messung zu verwenden, wird der Temperaturbereich weiter eingeschränkt, womit ein wichtiger Informationsanteil verlorengeht. Mit LOD kann der Bereich der messbaren T_1 -Relaxationszeiten deutlich vergrößert werden. Zwei Varianten werden dazu vorgeschlagen. Zum einen werden die bekannten inversion-recovery (IR) und saturation-recovery (SR) Experimente mit dem TN-LOD-Detektor kombiniert. Zum anderen wird gezeigt, wie das durch die relaxierende longitudinale Magnetisierung induzierte Signal mit einem Detektor mit hoher Güte direkt gemessen werden kann.

Chapter 1

Introduction

Electron paramagnetic resonance (EPR) is a technique that has been used for more than half a century to investigate the electronic and the spatial structure, the dynamics, concentrations, reaction mechanisms and the reactivity of paramagnetic species. To get a complete picture, several dedicated continuous wave (cw) and pulse methods have been developed. The main parameters of interest in EPR spectroscopy are on one side the different magnetic coupling constants, which provide information about the structure of a paramagnetic center, and on the other side the relaxation times, which give some information about dynamics and interactions between the analyte and its surroundings or between different paramagnetic centers. However, it is often a non-trivial task to obtain these data, and to get the full picture is like putting together a mosaic where every little piece of information is needed for interpretation. Pulse methods are much more flexible than cw methods because the magnetization can be manipulated to selectively amplify the desired information and because it is possible to correlate different parameters by recording spectra with more than one dimension. But it is necessary in most cases to perform pulse experiments at cryogenic temperatures because of the fast relaxation of magnetization at ambient temperature and the instrumental deadtime limiting the minimum time between the last pulse and the detection. Going to low temperatures does not significantly alter the magnetic parameters in most cases, but when the relaxation times are itself the target of the investigation, a method has to be chosen that is capable to measure them in the temperature range of in-

terest because the temperature dependence is one of the most important source of information for relaxation times. This prerequisite is often very difficult to fulfill. In many cases it is necessary to use an indirect procedure based on a model, for example regarding the homogeneity of the lines or the assumption that the relaxation is exponential, and only limited or sometimes even misleading information is obtained.

In the huge majority of experiments, detection is done at the same frequency as excitation, either by detecting the change of the reflected power at the cavity, as in cw EPR, or by creating electron coherence and detecting the transverse magnetization in the resonator caused by the spin moments, as in pulse EPR. These techniques are denominated with the expression *transverse detection* or *conventional detection*. A different possibility to detect an EPR signal has been developed already in the early days of EPR spectroscopy. BLOEMBERGEN and DAMON first published a method in 1952 where a coil oriented along the polarizing field direction, also called *longitudinal* or *z*-direction, is used to detect the spin polarization changing in time to study relaxation effects in ferromagnetic samples [1]. This general detection scheme is called *longitudinal detection* (LOD). Since then, it has been tested and used for different kinds of experiments. In 1957, WHITFIELD and REDFIELD checked the validity of the modified Bloch equations for large radio frequency (rf) fields with an LOD setup [2]. At the beginning of the sixties, PESCIA published his first paper about LOD [3]. During three decades he investigated systematically, both theoretically and experimentally, how an amplitude modulated excitation field induces a modulation of spin polarization [4], how this can be detected with an LOD setup [3], and how this can be used to measure spin-lattice relaxation times T_1 [5–7] or to separate spectra of two overlapping species [8]. In 1970, LEVANON, KWAN, and WEISSMAN observed the excitation of a triplet state via its spin polarization [9]. In the same year, MARTINELLI and his coworkers published a paper where they described the creation of multiple quantum transitions as a response of a nuclear spin system to irradiation with two nearly resonant rf fields [10]. Later they performed the same experiment with paramagnetic samples and explained the observations using a quantum mechanical approach based on second quantization [11]. They also presented a method

to determine spin-lattice relaxation times [12], and they separated spectra of two paramagnetic species with different relaxation times by comparing the LOD with the transversely detected cw EPR spectrum. In 1988, SCHWEIGER and ERNST established the connection between LOD and pulse EPR spectroscopy [13]. In this work, a series of new pulse schemes with LOD was presented for the measurement of field-swept EPR, relaxation times, and electron spin echo envelope modulation (ESEEM) spectra. In 1989, HYDE critically analyzed the potential of LOD both from a theoretical and a practical point of view, based on the knowledge and instrumental possibilities available at that time. He came to a rather disappointing conclusion, and this slowed down progress in the field in the following years. In 1994, NICHOLSON, ROBB, and LURIE presented a first study where LOD was used for EPR imaging [14]. In 1995, ATSARKIN *et al.* presented a method based on the ideas of HERVÉ and PESCIA to measure very short T_1 down to 10^{-10} s in semiconductors. From this list, of which some aspects will be discussed in more details later, one can see that LOD is useful especially in cases where other detection methods fail, for example to measure short T_1 or for detection during high-power excitation. It becomes evident that LOD is rather a supplement than a replacement for transverse detection techniques. This is not surprising because of completely different mechanisms responsible for the induced signal.

Although LOD has proved to be quite successful, widespread use has been prevented for different reasons. First of all, the sensitivity of an experiment usually increases with the detection frequency. LOD is done at frequencies at which the spin polarization is changed, which is in most cases more than three orders of magnitude lower than the frequency of the exciting magnetic field. Thus, the lack of sensitivity of LOD setups presented in the past is not surprising, especially if there is no other property that compensates at least partially for that drawback. Furthermore, some of the setups were instrumentally rather demanding, although the method itself is simple. In a field-swept EPR experiment with LOD, a periodic modulation of the magnetization is usually obtained by modulating the amplitude of the exciting magnetic field with the same frequency as detection is done. There are different possibilities to generate such an amplitude modulation. The one that seems easiest at a first glance, namely to modulate the amplitude of the source

power, is often not possible to implement. In fact, only few microwave (mw) sources allow to perform such a modulation, and arbitrary waveform generators that reach frequencies needed in a standard X-band experiment are not yet available. Another possibility is to use two frequency locked mw sources. This has been implemented by several groups. However, the frequency difference between the two sources has to be very stable, requiring a lot of experience in instrumentation. A much simpler approach is to use one mw source and a mixer to control the shape of the amplitude. This is the approach used in some of the experiments presented here.

Next to these technical reasons, there are a few non-physical reasons for the slow spreading of the method. One is that up to now, no commercially available spectrometer is factory-prepared for longitudinal detection, and only few EPR groups have the resources to build their own spectrometers and probeheads. Another reason, which might be rather unique for LOD, is the lack of continuity of the research¹. Several authors have published only one paper in this particular field, and others have worked on LOD for years without having an overview about other activities with this detection technique. A reason for this might be that the main field of application for LOD, the determination of longitudinal relaxation times, is a complicated topic and has found its way into routine EPR spectroscopy only recently and with the most simple methods that are available. Another reason might be that most articles published about the determination of relaxation times with LOD were methodological, which can be seen in the fact that mainly standard test samples have been investigated. LOD has been applied only exceptionally to problems of broader interest. Coming along with that, there exists no complete review about this field, although it has been mentioned in several monographs [15–18]. In the present study, this is the motivation to enlarge the general chapter about LOD somewhat over the usual size. An attempt is made to unify the different theoretical approaches to explain LOD experiments that use an amplitude modulated exciting field. This task is not performed with the most complete and general quantum mechanical method, but with one based on a perturbation treatment of the Bloch

¹An exception is the application of the LOD technique in EPR imaging, which is being developed relatively coherently and systematically.

equations that was originally published by HERVÉ and PESCIA [3]. The solution is general enough to explain the most relevant effects one observes in LOD experiments with continuous mw irradiation, but is simple enough that some physical insight can be gained from the obtained formulae.

The main goals for the work presented here are on the one hand to increase sensitivity of the detector to an extent that LOD becomes an interesting alternative to the established detection methods, even for every day use. On the other hand, new experimental schemes and pulse sequences should be developed that take full advantage of the setup. To achieve the desired sensitivity, it is necessary to use a new instrumental approach, because the previous approaches are too far away from being satisfactory that optimizing one of them would seem promising. The improvements are made on three items. The detection coil has a filling factor close to the theoretic maximum, it is integrated into a resonant circuit with a high quality factor, and the resonant frequency of this circuit is chosen as high as possible. By using a commercial spectrometer and probehead as the basis for this setup, even the demand for more general availability can be fulfilled. This new setup is then examined with respect to its performance and its flexibility to be used for different kinds of experiments.

In a next step, pulse schemes for LOD are presented that are optimized for the special properties of the probehead and the spectrometer. They can be used as building blocks to measure spin polarization in a pulse experiment. These schemes are free of instrumental deadtime, and data recording is even possible during high-power mw irradiation. In a first experiment to measure field-swept EPR spectra, spin nutation during mw excitation is used to induce a signal. This new experiment is called *transient nutation longitudinally detected EPR* (TN-LOD EPR). In a second experiment, spin magnetization is flipped by high-power mw pulses. This experiment is called *pulse-train excited longitudinally detected EPR* (PT-LOD EPR). For these new experiments, the mechanisms inducing the the signal are identified, possible problems and artifacts are addressed, and the situations are analyzed in which such experiments are a sensible supplement to established techniques.

The same building blocks to measure spin polarization are then used as detectors for the well-known inversion- and saturation-recovery experiments to measure

T_1 , without the shortcomings of the established detectors like a probe pulse or a two-pulse echo. It is shown how the experiments have to be performed and how the data can be processed to obtain the desired results. As a second possibility to measure T_1 , it is demonstrated that with the same setup the signal directly induced by the relaxing magnetization can be observed and analyzed to get the recovery curve in a single shot.

Chapter 2

EPR Basics

2.1 The Electron Spin

The spin is the quantum mechanical angular momentum \mathbf{S} which has to be added to the orbital angular momentum \mathbf{L} so that the total angular momentum $\mathbf{J} = \mathbf{L} + \mathbf{S}$ is conserved. Every angular momentum is coupled to a magnetic moment. For a free electron, we get

$$\boldsymbol{\mu}_S = -g_e\beta_e\mathbf{S} \quad (2.1)$$

with the BOHR magneton β_e of the electron and the so-called g factor of a free electron. The magnetic moment of an electron in a magnetic field \mathbf{B}_0 can take only discrete orientations. This leads to a quantization of the energy levels of the spin system. Their energy¹ depends on the magnetic quantum number m_S of the electron spin

$$E = m_S g_e \beta_e B_0 / \hbar. \quad (2.2)$$

B_0 is the amplitude of the static magnetic field along the laboratory z axis ($\mathbf{B}_0 = B_0\mathbf{e}_z$, where $(\mathbf{e}_x, \mathbf{e}_y, \mathbf{e}_z)$ is the basis of the cartesian coordinate system).

In EPR spectroscopy the sample is irradiated with a continuous or a pulsed oscillating magnetic field B_1 . If its energy matches the energy difference between two spin states, a transition between them may be induced. The resonant frequency

¹As far as not specifically indicated, energy values are given in angular frequency units throughout this thesis.

depends on the environment of the electron spins. A coupling between the spin and the orbital angular momentum leads to a derivation of the observed g value from g_e of the free electron. Furthermore, the magnetic moment of the observed electron spin interacts with magnetic moments of other electron and nuclear spins in its surrounding. Finally, an excited electron spin can transfer energy to its surrounding (lattice) which is called *spin-lattice relaxation*.

2.2 Quantum Mechanical Description of EPR

The energy levels of a quantum mechanical system can be described with a Hamiltonian operator \mathcal{H} . In most cases a spin system with an electron spin S coupled to n nuclear spins I_k can be described accurately by considering the electron Zeeman interaction, the zero-field splitting, the hyperfine interactions, the nuclear Zeeman interactions and the nuclear quadrupole interactions. The complete Hamiltonian for such a system can then be written as [19]

$$\mathcal{H}_0 = \mathcal{H}_{EZ} + \mathcal{H}_{ZFS} + \mathcal{H}_{HFI} + \mathcal{H}_{NZ} + \mathcal{H}_{NQ} \quad (2.3)$$

with the components

$$\mathcal{H}_{EZ} = \frac{\beta_e}{\hbar} \mathbf{B} \mathbf{g} \mathbf{S} \quad \text{electron Zeeman} \quad (2.4)$$

$$\mathcal{H}_{ZFS} = \mathbf{S} \mathbf{D} \mathbf{S} \quad \text{zero-field splitting} \quad (2.5)$$

$$\mathcal{H}_{HFI} = \sum_k \mathbf{S} \mathbf{A}_k \mathbf{I}_k \quad \text{hyperfine interaction} \quad (2.6)$$

$$\mathcal{H}_{NZ} = - \sum_k \gamma_k \mathbf{B}_0 \mathbf{I}_k \quad \text{nuclear Zeeman} \quad (2.7)$$

$$\mathcal{H}_{NQ} = \sum_{I_k > 1/2} \mathbf{I}_k \mathbf{P}_k \mathbf{I}_k \quad \text{nuclear quadrupole} \quad (2.8)$$

where \mathbf{g} denotes the electronic g tensor, \mathbf{D} the fine-structure tensor, \mathbf{A} the hyperfine tensors and \mathbf{P} the nuclear quadrupole tensors. If two electron spins are spatially close, the dipole-dipole and the exchange interaction between them also has to be considered. The dipole-dipole interaction can be expressed analogous to the

zero-field splitting

$$\mathcal{H}_{DD} = \frac{\mu_0}{2h} g_j g_k \beta_e^2 \left(\frac{\mathbf{S}_j \mathbf{S}_k}{r_{jk}^3} - \frac{3 (\mathbf{S}_j \mathbf{r}_{jk}) (\mathbf{S}_k \mathbf{r}_{jk})}{r_{jk}^5} \right) = 2\mathbf{S}_j \mathbf{D}_{jk} \mathbf{S}_k . \quad (2.9)$$

If electron j and k both have a finite expectation value in the same orbital corresponding to a weak bonding interaction, an exchange interaction can be observed of which normally only the isotropic part is considered

$$\mathcal{H}_J = -2J\mathbf{S}_j \mathbf{S}_k , \quad (2.10)$$

where J is the exchange coupling constant.

2.3 Microscopic versus Macroscopic Interpretation

By considering single spins, one has to deal with probabilities of the different states. This is difficult because we do not know the condition of a spin before the experiment, and our precision is limited by the uncertainty relation. But in a standard EPR experiment, we study a macroscopic ensemble of more than 10^{10} uniform spins². At thermal equilibrium, the probability $P(E_m)$ of a spin being in a state with energy E_m is given by the Boltzmann distribution [20]

$$P(E_m) = \frac{e^{-E_m/kT}}{\sum_n e^{-E_n/kT}} = \frac{e^{-E_m/kT}}{Z} = \frac{e^{-\beta E_m}}{\text{tr } e^{-\beta \mathcal{H}}} \quad (2.11)$$

with the Boltzmann constant k and the temperature T . Z is called a partition function, and β can be interpreted as the inverse spin temperature if considering only a quantum mechanical spin system. This distribution leads to a macroscopic magnetization \mathbf{M} which is defined as the magnetic moment per unit volume V [20]. At thermal equilibrium it is

$$\mathbf{M}_0 = \frac{1}{V} \sum_{i=1}^N \boldsymbol{\mu}_i = \frac{\mathbf{B}_0}{\mu_0} - \mathbf{H}_0 = \chi_0 \mathbf{H}_0 . \quad (2.12)$$

², 'uniform' means that the spins are described by the same Hamiltonian

where N is the number of spins in volume V , χ_0 is the magnetic susceptibility of the sample, \mathbf{H}_0 is the external magnetic field³, and $\mu_0 = 4\pi \cdot 10^{-7}$ Vs/Am is the permeability of vacuum. \mathbf{M}_0 is the physical property which is accessible by the detection setup. Its magnitude is given by

$$M_0 = \frac{N}{V} g \beta_e \frac{\sum_{m_S=-S}^S m_S e^{-m_S g \beta_e B_0 / kT}}{\sum_{m_S=-S}^S e^{-m_S g \beta_e B_0 / kT}} \approx \frac{N g^2 \beta_e^2 S(S+1)}{3V k(T + \Delta)} B_0 \approx \chi_0 B_0 / \mu_0, \quad (2.13)$$

where Δ is the Weiss constant. In magnetic resonance experiments, the assumption $\Delta \ll T$ usually holds. Therefore Δ will be neglected in the following.

The most convenient way to mathematically describe pure as well as non-pure states⁴ is by using a density operator σ [22]. In the eigenbasis of \mathcal{H} , the diagonal elements of σ denote the probability of finding the spin system in the corresponding eigenstate, which is the population of this state. Off-diagonal elements indicate a coherent superposition of eigenstates, usually abbreviated as coherence. In thermal equilibrium at temperature T we get

$$\sigma_0 = \frac{e^{-\beta \mathcal{H}}}{Z}. \quad (2.14)$$

In the eigenbasis of \mathcal{H} , the probability distribution of the eigenstates, $P_m = \sigma_{0,mm}$, describes a Boltzmann distribution.

The time evolution of σ can be described by the quantum mechanical master equation introduced by KARPLUS and SCHWINGER⁵ [23]

$$\frac{\partial}{\partial t} \sigma(t) = -i [\mathcal{H}, \sigma(t)] - \Gamma \{ \sigma(t) - \sigma_0 \}. \quad (2.15)$$

The relaxation superoperator Γ accounts for the dissipative interactions between the spin system and the lattice and drives $\sigma(t)$ towards σ_0 .

³The actual magnetic field is described by the magnetic induction \mathbf{B} , while \mathbf{H}_0 is the part of the field that is induced by macroscopic currents [21]. As is common in magnetic resonance, \mathbf{B} is referred to as the magnetic field throughout this thesis.

⁴Non pure states can arise as a mixture of pure states or as a restriction of a pure state onto a subsystem.

⁵ $[\cdot, \cdot]$ denotes the commutator $[A, B] = AB - BA$.

2.4 Excitation of a Spin System

2.4.1 Effect of an Alternating Magnetic Perturbation

The evolution of an electron-nuclear spin system in the presence of an mw field is usually described by the spin Hamiltonian [15]

$$\mathcal{H} = \mathcal{H}_0 + \mathcal{H}_1(t), \quad (2.16)$$

where \mathcal{H}_0 is given by Eq. (2.3) and \mathcal{H}_1 is an oscillating perturbation

$$\mathcal{H}_1(t) = \beta_e \mathbf{B}_{\text{mw}}(t) \mathbf{gS} / \hbar. \quad (2.17)$$

$\mathbf{B}_{\text{mw}}(t)$ is normally applied in the form of a linearly polarized mw field with frequency ω_{mw} ,

$$\mathbf{B}_{\text{mw}}(t) = 2B_1 \cos(\omega_{\text{mw}}t + \varphi) \mathbf{e}_x, \quad (2.18)$$

that can be decomposed into two counter-rotating components, of which only the field rotating in the same sense as the spins will be retained,

$$\mathbf{B}_{\text{mw}}(t) = B_1 (\cos(\omega_{\text{mw}}t + \varphi) \mathbf{e}_x + \sin(\omega_{\text{mw}}t + \varphi) \mathbf{e}_y). \quad (2.19)$$

Let us consider now a spin $S = 1/2$ with an isotropic g value. Its Hamiltonian \mathcal{H}_S becomes time-independent in a frame rotating with frequency ω_{mw} about the S_z axis and can be written as

$$\mathcal{H}'_S = \Omega_S S_z + \frac{g\beta_e}{\hbar} B_1 (\cos(\varphi) S_x + \sin(\varphi) S_y) \quad (2.20)$$

with the frequency offset $\Omega_S = \omega_S - \omega_{\text{mw}} = g\beta_e B_0 / \hbar - \omega_{\text{mw}}$. The equation of motion of the magnetic moment $\boldsymbol{\mu}$ of a spin packet including both the effect of \mathbf{B}_0 and \mathbf{B}_{mw} is given according to the classical theory by

$$\frac{d\boldsymbol{\mu}}{dt} = -\boldsymbol{\mu} \times \frac{g\beta_e}{\hbar} (\mathbf{B}_0 + \mathbf{B}_{\text{mw}}(t)). \quad (2.21)$$

In a rotating frame, the time dependence of \mathbf{B}_{mw} can be eliminated⁶

$$\begin{aligned} \frac{\delta \boldsymbol{\mu}^r}{\delta t} &= -\boldsymbol{\mu}^r \times \frac{g\beta_e}{\hbar} \left(\left(B_0 - \frac{\hbar \omega_{\text{mw}}}{g\beta_e} \right) \mathbf{e}_z^r + B_1 \mathbf{e}_x^r \right) \\ &= -\boldsymbol{\mu}^r \times \frac{g\beta_e}{\hbar} \mathbf{B}_{\text{eff}}^r = \boldsymbol{\mu}^r \times \boldsymbol{\omega}_{\text{eff}}^r, \end{aligned} \quad (2.22)$$

⁶ $\boldsymbol{\mu}$ in the laboratory frame and $\boldsymbol{\mu}^r$ in the rotating frame are related through the general law of relative motion $\delta \boldsymbol{\mu}^r / \delta t = d\boldsymbol{\mu} / dt - \boldsymbol{\omega} \times \boldsymbol{\mu}$

where

$$\mathbf{B}_{\text{eff}}^r = \left(B_0 - \frac{\hbar\omega_{\text{mw}}}{g\beta_e} \right) \mathbf{e}_z^r + B_1 \mathbf{e}_x^r. \quad (2.23)$$

Physically this means that $\boldsymbol{\mu}^r$ acts as though it experienced effectively a static magnetic field \mathbf{B}_{eff} and precesses, or nutates, at angular frequency

$$\omega_{\text{eff}} = g\beta_e B_{\text{eff}}/\hbar = \sqrt{\omega_1^2 + \Omega_S^2}, \quad (2.24)$$

the so-called nutation frequency, on a cone of fixed angle θ about \mathbf{B}_{eff} . This is shown in Fig. 2.1. θ is given by

$$\tan(\theta) = \frac{B_1}{B_0 - \frac{\hbar\omega_{\text{mw}}}{g\beta_e}} = \frac{\omega_1}{\omega_{\text{mw}} - \omega_S}. \quad (2.25)$$

For an arbitrary spin system, the nutation frequency is proportional to the product of the transition matrix element of the excited transition and B_1 [24, 25].

If the duration of the mw irradiation is much longer than the magnetization needs to relax, an effect called *saturation* may occur. This effect can be described

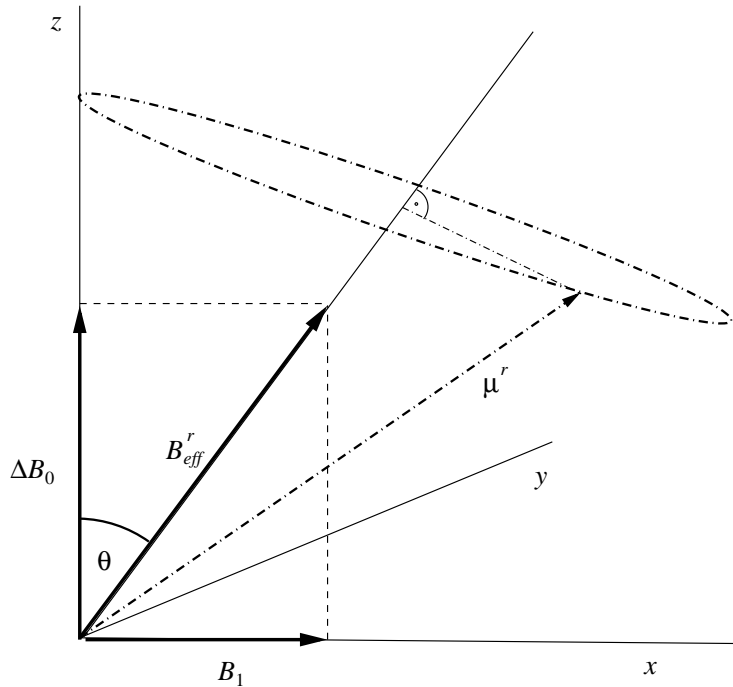


Figure 2.1: Effective field $\mathbf{B}_{\text{eff}}^r$ with $\Delta B_0 = B_0 - \hbar\omega_{\text{mw}}/g\beta_e$, and motion of the magnetic moment $\boldsymbol{\mu}^r$.

by the saturation factor

$$a = \omega_1^2 T_1 T_2, \quad (2.26)$$

where $\omega_1 = g\beta_e B_1/\hbar$ is the field intensity of the mw field in angular frequency units, T_1 is the longitudinal and T_2 the transverse relaxation time. If $a \ll 1$, the spin system is said to be far from saturation. If a approaches or even passes 1, the spin system is saturated. In cw EPR experiments, saturation manifests itself by a line broadening and a decrease of signal intensity. In pulse EPR, a saturation pulse might be used as a preparation pulse, for example in relaxation time studies.

2.4.2 Ideal Pulse Experiment

An mw pulse is considered ideal if it rotates the equilibrium magnetization \mathbf{M}_0 about the direction of the applied mw field \mathbf{B}_1 irrespective of the resonance offset [22]. This is fulfilled if

$$\|\mathcal{H}'_1\| \gg \|\mathcal{H}'_0\|. \quad (2.27)$$

In this case, the evolution of the system during the pulse can be neglected. For an ideal non-selective pulse of duration t_p , we get the pulse rotation angle

$$\beta = \omega_1 t_p. \quad (2.28)$$

Instrumental aspects like rise and fall time of the pulses are neglected. In experiments, this can be achieved only for narrow spectra of $S = 1/2$ species. In this case, we get

$$\omega_1 = \frac{g\beta_e}{\hbar} B_1, \quad (2.29)$$

assuming an isotropic g value.

The magnetization vector $\boldsymbol{\mu}^r(\Omega_S, t)$ of a spin packet in the rotating frame during mw irradiation can be calculated with respect to the initial magnetization $\boldsymbol{\mu}_0^r(\Omega_S) = \boldsymbol{\mu}^r(\Omega_S, t = 0)$ as [26]

$$\boldsymbol{\mu}^r(\Omega_S, t) = [\boldsymbol{\mu}_0^r \cdot \mathbf{b}^r] \mathbf{b}^r + (\boldsymbol{\mu}_0^r - [\boldsymbol{\mu}_0^r \cdot \mathbf{b}^r] \mathbf{b}^r) \cos(\omega_1 t) - [\mathbf{b}^r \times \boldsymbol{\mu}_0^r] \sin(\omega_1 t) \quad (2.30)$$

with the unit vector $\mathbf{b}^r = \mathbf{b}^r(\Omega_S)$ along $\mathbf{B}_{\text{eff}}^r(\Omega_S)$.

In EPR, a more distinct differentiation concerning ideal pulses can be made according to JESCHKE [27] if the possibility to neglect the effect of the static Hamiltonian during mw irradiation is the only condition for an ideal pulse. If so, the case described by Eq. (2.27) is called an *ideal non-selective pulse*. In addition, we can introduce *ideal selective pulses* where only one transition of the spectrum is excited and *ideal semi-selective pulses* where the transitions of a fictitious spin 1/2 [20], but no other transitions, are excited.

2.5 Relaxation

This section gives a short overview about relaxation in EPR and the mechanisms responsible for relaxation in solids. A detailed description of relaxation phenomena in EPR can be found in several textbooks [15, 17, 28, 29]. Some established methods using transverse detection to measure longitudinal relaxation times are listed because it is quite difficult to find a comprehensive and up-to-date list of the different techniques for this task.

2.5.1 Definitions

Interactions within a spin system and of a spin system with its surrounding cause coherence to dephase, which is called *transverse* or *spin-spin relaxation*, and polarization to approach its equilibrium value, called *longitudinal* or *spin-lattice relaxation*. These processes cannot be described by a spin Hamiltonian of the form (2.3). If longitudinal and transverse relaxation are mono-exponential, they are described by the relaxation times T_1 and T_2 , respectively. Thus, the return of \mathbf{M} towards its equilibrium value \mathbf{M}_0 following an excitation is described by

$$M_{xy}(t) = M_{xy}(0) e^{-t/T_2}, \quad (2.31)$$

$$M_z(t) = M_0 + (M_z(0) - M_0) e^{-t/T_1}, \quad (2.32)$$

with the transverse magnetization $M_{xy}(t)$ and the longitudinal magnetization $M_z(t)$ at time t after the exciting field has been switched off. In the general case, the only restriction for a function describing relaxation after excitation is that polarization must be monotonically decaying towards its equilibrium value. Because of the

handy notation, T_1 and T_2 will be used as a general acronym for longitudinal and transverse relaxation except for explicitly non-exponential relaxation curves.

Longitudinal Relaxation: Since spontaneous emission can usually be neglected to explain longitudinal relaxation at frequencies below 1 THz, we have to consider interactions of the spin system with its surrounding, where two prerequisites have to be fulfilled. The surrounding must have degrees of freedom to provide or accept energy for the spin flips, and there must be a relaxation pathway coupling these degrees of freedom with the magnetic moment of the spins, which can interact only with magnetic fields. Different processes are responsible for relaxation in gases or liquids and relaxation in solids. In concentrated systems the dipolar coupling between electron spins in different molecules provide further relaxation pathways that lead to a broadening of the EPR lines. The effect on T_1 can be evaluated through the interaction energy and the appropriate correlation function.

Transverse Relaxation: No transfer of energy with the surrounding is required for the decay of coherence between two states of a spin system. But it requires some kind of an interaction with the environment, otherwise the dynamics of the spin system would be coherent. A spin flip that leads to longitudinal relaxation destroys the correlation of the precession phase between the affected spin and the other spins, hence it contributes to transverse relaxation as well, as a result T_2 cannot be longer than T_1 .

Rotating Frame Relaxation: In the presence of a static magnetic field, the lattice is no longer magnetically and electrically isotropic. The spin-lattice relaxation times parallel and perpendicular to \mathbf{B}_0 differ from each other. Therefore, under spin-locking conditions T_1 and T_2 cannot provide a complete description of relaxation anymore. REDFIELD called the relaxation time parallel to \mathbf{B}_1 , but perpendicular to \mathbf{B}_0 , the *rotating frame relaxation time* $T_{1\rho}$ [30] and showed that $T_2/2 < T_{1\rho} \leq T_1$ holds for a single spin species. $T_{1\rho}$ is usually found to be closer to T_1 than to T_2 .

2.5.2 Bloch Equations

BLOCH introduced a set of coupled differential equations to describe the phenomenological behavior of magnetization during and after an excitation [31]. Ac-

According to this theory, the equation of motion of \mathbf{M} in the laboratory frame is

$$\frac{d\mathbf{M}}{dt} = -\frac{g\beta_e}{\hbar}\mathbf{M}(t) \times \mathbf{B}(t) - \mathbf{R}(\mathbf{M}(t) - \mathbf{M}_0) \quad (2.33)$$

with the relaxation matrix

$$\mathbf{R} = \begin{pmatrix} 1/T_2 & 0 & 0 \\ 0 & 1/T_2 & 0 \\ 0 & 0 & 1/T_1 \end{pmatrix}. \quad (2.34)$$

Eq. 2.33 can be rewritten in explicit notation, this time in the rotating frame, as

$$\begin{aligned} \frac{dM_x^r}{dt} &= -\Omega_S M_y^r - \frac{M_x^r}{T_2}, \\ \frac{dM_y^r}{dt} &= \Omega_S M_x^r - \omega_1 M_z - \frac{M_y^r}{T_2}, \\ \frac{dM_z}{dt} &= \omega_1 M_y^r - \frac{M_z - M_0}{T_1}. \end{aligned} \quad (2.35)$$

The steady-state solutions of these differential equations with continuous mw irradiation can be found by setting $d\mathbf{M}^r/dt = 0$ to be

$$M_x^r = \frac{\Omega_S \omega_1 T_2^2}{1 + (T_2 \Omega_S)^2 + \omega_1^2 T_1 T_2} M_0 = \frac{\Omega_S \omega_1 T_2^2}{1 + (T_2 \Omega_S)^2 + a} M_0, \quad (2.36)$$

$$M_y^r = -\frac{\omega_1 T_2}{1 + (T_2 \Omega_S)^2 + \omega_1^2 T_1 T_2} M_0 = -\frac{\omega_1 T_2}{1 + (T_2 \Omega_S)^2 + a} M_0, \quad (2.37)$$

$$\begin{aligned} M_z &= \left(1 - \frac{\omega_1^2 T_1 T_2}{1 + (T_2 \Omega_S)^2 + \omega_1^2 T_1 T_2} \right) M_0 \\ &= \left(1 - \frac{a}{1 + (T_2 \Omega_S)^2 + a} \right) M_0 = \frac{1 + (T_2 \Omega_S)^2}{1 + (T_2 \Omega_S)^2 + a} M_0. \end{aligned} \quad (2.38)$$

These equations are phenomenologically derived and not necessarily coupled to a physical process, so they are relatively generally applicable without knowing the exact relaxation mechanisms. Because of the simplicity of the Bloch equations, they are often used as the theoretical background for the derivation of methods

to measure relaxation times. As these methods do not provide the full relaxation pattern of the longitudinal or the transverse magnetization, but relaxation is monitored with an experimental property, *e.g.* the phase of the signal, ambiguous or even wrong results are obtained for multi-exponential or non-exponential relaxation curves. Equivalently, some of the methods for data analysis explicitly expect an exponentially relaxing magnetization, leading to wrong results if this is not fulfilled.

2.5.3 Longitudinal Relaxation in Solids

Phonons are appropriate energy quanta in the solid state for energy exchange. Therefore longitudinal relaxation leads to a temperature equilibrium between the lattice, which has the thermodynamic temperature, and the spins. The coupling between the phonons and the spin system is done by a modulation of the crystal field, which interacts with the spin-orbit coupling of the spins. The efficiency of these processes depends on the temperature dependent spectral density of the phonons at the transition frequency for the spin flips.

Direct Process: If the coupling between the spin system and the lattice phonons are treated with perturbation theory, the solution of a first order approximation is called a direct process. It involves the absorption or emission of one phonon of frequency ω_S . Its frequency and temperature dependence for an $S = 1/2$ system is given by

$$\frac{1}{T_{1D}} \propto \omega_0^3 B_0^2 \coth\left(\frac{\hbar\omega_0}{kT}\right). \quad (2.39)$$

In the high-temperature and high-field approximation, the relation $T_{1D} \propto B_0^{-4} T^{-1}$ can be derived for this process. Experimental results show that the direct process is only dominant for very low temperatures.

Raman Process: According to the nomenclature in optical spectroscopy, a two-phonon process where the difference between the two phonon energies matches the frequency of the EPR transition is called a Raman process. The spin system absorbs a high energetic phonon, going into a virtual excited state, and immediately emits another high-frequent phonon. This process becomes probable because

phonons are Boltzmann distributed. The maximum of the phonon density is approximately kT . At higher temperatures, the low probability of a two-phonon process is overcompensated by the higher density of high-energetic phonons. The temperature dependence of Raman processes is normally between $T_{1R} \propto T^{-5}$ and $T_{1R} \propto T^{-9}$.

Orbach Process: Two-phonon processes can become very efficient if not only a virtual, but a really existing excited state is involved. It is obvious that in this case the requirements on the coincidence of two matching phonons are not that rigid anymore. If the spectrum of the phonons is much broader than the inverse lifetime of the excited spin state, this process can even be considered as a direct process in a system with more than two spin states. If the excited state is by the amount Δ higher than the ground state of the system and if $kT \ll \Delta$, the temperature dependence is found to

$$\frac{1}{T_{1O}} \propto \exp\left(-\frac{\Delta}{kT}\right). \quad (2.40)$$

As a consequence, Δ can be determined from the temperature dependence of T_1 .

2.5.4 Transverse Relaxation in Solids

T_2 is often not well defined in solids as we deal with a virtually infinite network of coupled spins. Except for a few special cases it is impracticable to treat the infinite system, yet it is also impossible to make a clear cut between a finite spin system which behaves coherently and its environment. Because of a strong dependency of the actual experiment on the number of mutually coupled spins exhibiting coherent and reversible dynamics, characteristic decay times applying to widely used experiments are defined to quantify transverse relaxation in solids.

The phase-memory time T_m , associated with the decay of the primary echo when the time between the pulses is increased, is a useful empirical parameter. In the absence of instantaneous diffusion, T_m is often exponential. T_m corresponds to the inverse homogeneous linewidth and is sometimes simply called T_2 , although there are also other contributions to T_m than lifetime broadening ($1/2T_1$) and spin-spin relaxation ($1/T_2'$). A more detailed discussion is given in [15].

2.5.5 Diffusion Processes Contributing to Relaxation

To understand the dynamics of a spin system, it is usually necessary to identify all the involved relaxation pathways. By definition, relaxation times as previously described characterize only the lifetime of a non-equilibrium state with respect to relaxation processes between energy levels that are affected by the excitation. *Diffusion processes* form another important class of processes influencing the relaxation behaviour of a spin system [15].

Spectral Diffusion: If the width of the spectrum exceeds the excitation bandwidth of the mw pulse so that only spins with resonant frequency in the vicinity of ω_{mw} are excited, longitudinal or spin-spin relaxation of these spins changes the local field at spins that are not excited. This leads to a transfer of spin magnetization to parts of the spectrum where spins cannot be excited or detected directly. As a result, spins with non-equilibrium magnetization are replaced by spins that are still at thermal equilibrium. To an observer this manifests as a relaxation process. Spectral diffusion contributes to both longitudinal and transverse relaxation of the excited spins.

Instantaneous Diffusion: Even at the relatively low concentrations of paramagnetic centers used in most pulse EPR experiments, the interaction between the electron spins often cannot be neglected. If an mw pulse excites dipole-coupled spins, the spin flips lead to a change of the local field at each particular spin. In general, the spatial arrangement of the excited spins to adjacent spins is different (distance and angles), hence the changes of the local field are different as well. As a consequence, spins with the same resonant frequency before the mw pulse can have different resonant frequencies after the pulse. Since the duration of the pulse is often negligible compared to the relaxation times, this phenomenon can be considered as an instantaneous diffusion of magnetization in the spectral dimension.

Spin Diffusion: Even in the absence of molecular motion or additional pulses, magnetization can spread from the excited A spin to not excited B spins. For this to be significant, dipolar coupling between A and B spins of the same order of magnitude as the difference in their respective resonant frequencies is required. The flip-flop term $\omega_{\text{ff}} (S_x^A S_x^B + S_y^A S_y^B)$ of the dipolar coupling Hamiltonian then mixes A and B spins, and polarization on an A spin transition partially evolves to

polarization on B transitions. This process is called spin diffusion. The rate of spin diffusion is proportional to r^{-6} , where r is the distance between the A and the B spins. This is also the mechanism that establishes a common spin temperature for those spins which differ in their resonant frequency by less than the average dipolar coupling to the next neighbor. Such a group of spins is called a *spin bath*. Different spin baths may also exchange energy with each other if energy-conserving flip-flops between spins of different baths are made possible. This process is a form of cross relaxation.

Chemical Reactions: Decay or transfer of magnetization is also observed when chemical reactions occur on the time scale of an EPR experiment. In the simplest case the observed species reacts to a species that cannot be observed. For a first-order reaction with rate constant k_r , the apparent transverse relaxation time T_2^a is given by

$$T_2^a = \frac{T_2}{1 + k_r T_2}. \quad (2.41)$$

Polarization vanishes in the course of such a chemical reaction instead of approaching thermal equilibrium. This leads to a bi-exponential decay from which both T_1 and k_r can be determined. If the initially excited species reacts to another observable species, there is generally a change $\Delta\omega$ in the resonant frequency of a given transition. As chemical reactions are incoherent processes, this destroys coherence of transitions if $\Delta\omega \gg k_r$, while polarization survives but may be distributed among different transitions in the reaction product.

2.5.6 Problems of Relaxation Studies

The multitude of sophisticated approaches to relaxation theory indicates that the interpretation of relaxation data is usually more demanding than the interpretation of spin Hamiltonian parameters. Foremost, spin Hamiltonian parameters can usually be separated by generally applicable recipes, while relaxation curves are monotonous decays made up of several contributions which often cannot be easily identified or separated. Quite often these curves can be fitted within the error of the data by a single exponential, hence only one parameter, the relaxation time, can be obtained. Relaxation measurements are therefore most useful when a single pro-

cess dominates the relaxation rate. An example are strongly diluted paramagnetic spin species in liquid solution. If several processes significantly contribute to the relaxation rate, it is sometimes possible to separate them by varying the measurement temperature or frequency. But because the dominant relaxation process may change several times over the observed temperature and frequency range, special care has to be taken to collect enough data points in each dimension to avoid ambiguous results. Studying the orientation dependence of the relaxation times of solids is sometimes possible by introducing B_0 as a second dimension.

Another difficulty arises from the fact that relaxation not only depends on the parameters of the spin Hamiltonian of the free molecule, but also on the properties of the environment, in particular on lattice dynamics. This provides access to information which cannot be obtained from spin Hamiltonian parameters alone. But it may lead to a situation where the number of relevant parameters is very large and possibly not well known.

2.5.7 Measurement of Longitudinal Relaxation Times

In this section, an overview over the wide variety of methods based on transverse detection to determine longitudinal relaxation times with respective references is given. First some experiments with continuous mw irradiation are described, afterwards methods with pulse excitation are listed. Not included are the methods with longitudinal detection, which are summarized after the introduction of this detection technique.

Because it is usually impossible to determine T_1 from spectral features of a single EPR experiments, it is necessary to record several spectra, varying an experimental parameter which induces a T_1 dependent change. Most often, the saturation parameter a is changed by varying the mw field amplitude B_1 . A simple way is to record a series of EPR spectra with mw power ranging from far below saturation, *i.e.* $a \ll 1$, to very high saturation levels, $a \gg 1$, and then plot the saturation factor $a = \omega_1^2 T_1 T_2$ against B_1^2 [16]. The slope of this curve is equal to $T_1 T_2$. T_2 can be determined from the homogeneous linewidth far below saturation.

a can be calculated for a homogeneous Lorentzian line as

$$a(B_1) = \left(\frac{\Delta B_{pp}(B_1)}{\Delta B_{pp}^0} \right)^2 - 1, \quad (2.42)$$

where $\Delta B_{pp}(B_1)$ and ΔB_{pp}^0 are the peak-to-peak linewidth for a given mw field amplitude and in the limit of B_1 going to zero, respectively.

A similar proceeding is possible by measuring the peak-to-peak amplitude y'_m of the first-derivative EPR absorption signal as a function of B_1^2 . At low power levels, *i.e.* if $a \ll 1$, y'_m is proportional to B_1 . At very high saturation levels, y'_m becomes proportional to B_1^{-2} , *i.e.* to the inverse of the mw power. The maximum is reached for $a = 1/2$, and T_1 can be calculated as

$$T_1 = \frac{a\hbar^2}{T_2 g^2 \beta_e^2 B_1^2}. \quad (2.43)$$

It is as well possible to display saturation data by plotting y'_m relative to a standard y'_{ms} against the logarithm of the power P [32]. This gives for every sample a curve with a similar shape, shifted against each other in the $\log(P)$ dimension. Now the product $T_1 T_2$ of an unknown species can be determined relative to that of a known species, *e.g.* DPPH, as

$$T_1 T_2 = \frac{P_{\text{DPPH}}}{P} T_{1,\text{DPPH}}^2, \quad (2.44)$$

with $T_{1,\text{DPPH}} = T_{2,\text{DPPH}} = 6 \times 10^{-9}$ s [33], [34].

LIVSHITS *et al.* [35] used the ratio ρ'_1 of the 90° out-of-phase to the in-phase (doubly integrated) signal intensity at the first harmonic⁷ of the field modulation frequency ω_m as a function of B_1 to determine T_1 . With the assumption of experimental conditions usually found with nitroxide radicals, especially $T_2 \ll T_1$ and $\omega_m^2 T_1^2 \ll 1$, the approximate relation

$$\rho'_1 = \frac{\iint V'_1 d\Omega_S}{\iint V_1 d\Omega_S} \approx -\frac{\omega_m T_1}{2} \left(\frac{T_2}{T_1} + \frac{a}{2(1+a)} \right) \quad (2.45)$$

⁷The first harmonic of the signal has been used because ρ'_1 is less sensitive to molecular rotation and depends less on T_2 than, for example, the second harmonic.

can be used to estimate T_1 . V_1 and V_1' denote the first harmonic in-phase and the 90° out-of-phase signal amplitude, respectively. This formula is best valid for $a \ll 1$, thus it is not necessary to saturate a transition to determine T_1 . But this experiment is listed as a saturation method nonetheless because a is the varied parameter.

Two difficulties arise in the determination of relaxation times with a saturation method. The accurate measurement of the mw power and the conversion of the power incident on the cavity into B_1^2 values. A calibration of B_1^2 may be carried out experimentally from saturation data of a species such as DPPH whose relaxation properties are known. Furthermore, for inhomogeneously broadened lines the treatment is more complex since the Bloch equations, on which the derivation of these methods is based, does not generally apply.

Among the most popular pulse methods to measure spin-lattice relaxation times of paramagnetic species are the inversion-recovery (IR) [36] and the saturation-recovery (SR) [37] experiments. In an IR experiment, \mathbf{M}_0 is inverted by a π preparation pulse, and $M_z(t)$ is read out with an appropriate detector sequence generating transverse magnetization, usually a probe pulse or a two-pulse echo. In the case of echo detection, time T between inversion and detection is increased step by step, and the recovery is recorded point by point, while with probe-pulse detection the recovery is recorded in one shot, resulting in a shorter measuring time. The application of the IR experiment is restricted since only a few spectra are sufficiently narrow to be completely inverted by a π pulse. Otherwise IR is likely to be affected by spectral and spin diffusion. Inversion by adiabatic passage or a pulse train can solve this problem if the spectrum is not too broad or if spectral and spin diffusion are sufficiently slow. The bandwidth of the inverting pulse must be much larger than the bandwidth of the detection sequence. But even with these precautions IR is more affected by spectral and spin diffusion than SR, where a saturation instead of an inversion pulse is applied at the beginning of the sequence, while the detectors remain basically the same [34, 38]. This pulse should not only saturate transitions that lie within the narrow bandwidth of the probe pulse, but also those transitions that can exchange magnetization with this region on the time scale of T_1 by spectral diffusion or spin diffusion. A good result is obtained if the length

of the saturation pulse is on the order of T_1 [36]. Alternatively, the B_0 field can be swept during the saturation pulse to increase the excitation bandwidth [39]. To remove the free induction decay (FID) of the saturation pulse, which is superimposed to the signal, a $[(x) + (-x)]$ phase cycle should be applied. If no precautions are taken to exclude the influence of spectral and spin diffusion, the results should be cross-checked with a measurement of the stimulated echo decay where these processes are even more pronounced. On the other hand, spin diffusion processes can be studied by comparing results of IR with these of SR experiments [36].

In a *stimulated echo experiment*, a polarization grating is created by the first two mw pulses with interpulse delay τ_p [15]. The decay of the non-equilibrium polarization is determined by measuring the amplitude of the stimulated echo as a function of the recovery time T . The method is more susceptible to spectral and spin diffusion than any other method discussed so far because the grating is destroyed by diffusion of polarization over a frequency difference on the order of $1/\tau_p$, while in the other methods the relevant frequency difference is given by the excitation bandwidth of the first pulse. By varying τ_p , such contributions can be recognized and quantified.

If T_1 is longer than the maximum achievable shot repetition time t_s of the spectrometer, it can be estimated by observing the variation of the amplitude of a primary echo as a function of $1/t_s$, which is called *echo saturation by fast repetition*. For mono-exponential longitudinal relaxation, we find

$$\frac{s(t_s)}{s(t_s \rightarrow \infty)} = 1 - e^{-t_s/T_1}, \quad (2.46)$$

In this experiment it is not possible to avoid the admixture of spectral and spin diffusion.

Spectral diffusion can be separated from longitudinal relaxation with *spectral hole burning* by a soft selective mw pulse. The amplitude and shape of the spectral hole is observed after a mixing time by measuring the FID which follows a non-selective $\pi/2$ pulse [40]. Longitudinal relaxation causes a decrease of the amplitude of the hole with increasing mixing time, while the shape of the hole, which is obtained by Fourier transformation (FT) of the FID, remains constant. Spectral diffusion, on the other hand, broadens the hole which leads to a faster decay of

the FID. Formulae for hole broadening by longitudinal relaxation of remote spins, which are coupled to the observed spin, are given in [41].

Another possibility to investigate diffusion processes is *polarization-transfer electron-electron double resonance (ELDOR)* [42], where a small part of the spectrum is inverted or saturated with a pump pulse, and the build-up and decay of non-equilibrium polarization at a different spectral position is observed either with a probe pulse or a primary echo.

To disentangle the relaxation times of two spin species with similar T_1 , but different g value, the electron Zeeman resolved IR (EZ-IR) experiment was introduced to obtain the relaxation pattern as a function of the g value [43]. With this method, first an inversion pulse is applied, and then $M_z(T)$ is read out with a two-pulse echo. In a second dimension, a sinusoidal modulation of the B_0 field is applied. The pulses and thus the echo are at the zero-crossing of this modulation. The parameter that is varied is the amplitude of the modulation ΔB_0 . The echo accumulates the EZ phase

$$\varphi_{ez} = \frac{8g\beta_e}{h} \Delta B_0 \tau_p, \quad (2.47)$$

where τ_p is the difference between the pulses of the primary echo sequence. The frequency of the ΔB_0 modulation is on the order of 500 kHz, thus $\tau_p \approx 1 \mu\text{s}$. T_m must be on the same order of magnitude to obtain an echo. Therefore the number of samples or the temperature range for this method is rather restricted, but its features are unique and the method might be very helpful in certain cases, especially to identify the number of relaxation components.

The choice of the best method to analyze longitudinal relaxation depends on the number of independent contributions to the relaxation curve, the properties of the investigated spin system, the order of magnitude of the relaxation times, and on the available equipment. While simple cw methods might satisfy for radical species with a mono-exponential decay of $M_z(t)$, they are often useless for more complicated systems. Pulse methods, which give a transient of the relaxation pattern, are powerful and flexible, but it is necessary to have a suitable detector. This limits these methods to systems with T_m larger than the instrumental deadtime t_d . t_d is the time after the end of a pulse until the power incident on the mw detection device has fallen below the maximum value of this unit. t_d is thus determined by

the applied mw power, the quality factor of the resonator, the frequency band of the measurement and the switching time of the mw switches that form the pulses.

Chapter 3

Introduction to Longitudinal Detection

In this chapter, the principle of longitudinal detection (LOD) is described, the theoretical concepts used to explain LOD experiments are summarized, and previous work about this topic is reviewed.

3.1 Principle of LOD

With LOD the change of the M_z magnetization – in magnetic resonance usually referred to as polarization – induces a voltage

$$V_{\text{ind}} \propto -nA \frac{dM_z(t)}{dt} \quad (3.1)$$

in a pick-up coil oriented parallel to the polarizing magnetic field \mathbf{B}_0 , where n is the number of turns of the detection coil and A is its cross-section. Instead by n and A , a coil is usually characterized by its inductance L . This coil is then integrated into a serial LCR circuit, and the detected signal is the voltage V_{Ξ} across the capacity C . This is shown schematically in Fig. 3.1.

With LOD, other experiments have to be performed than with conventional detection. The most commonly used excitation scheme is irradiating the spin system with two mw fields with different frequencies ω_l and ω_r , differing by $\Omega_m = \omega_r - \omega_l \ll \omega_l, \omega_r$ [44, 45], or as an equivalent approach, amplitude-modulating the mw field with frequency Ω_m [3]. This induces a periodic modulation of $M_z(t)$. In this thesis, experiments with a continuous excitation, inde-

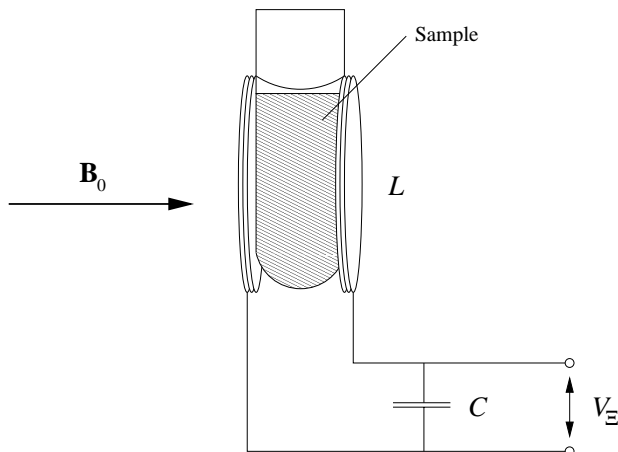


Figure 3.1: Schematic drawing of the setup for longitudinal detection. The detection coil with inductance L is oriented with its axis parallel to the polarizing magnetic field \mathbf{B}_0 and integrated into an LCR resonant circuit. The detected signal is the voltage V_E across the capacitor C .

pendent of its power, where magnetization is permanently in a non-equilibrium state, is called *cw LOD EPR*.

A different approach is the use of pulse excitation schemes [13] where, analogous to the well-known pulse experiments with transverse detection, magnetization is specifically brought into and manipulated in a non-equilibrium state and can, at least to a large extent, relax towards its Boltzmann equilibrium between the excitation sequences. This is called *pulse LOD EPR*. Between *cw* and *pulse LOD EPR* is a flowing boundary.

3.2 Simulation of the Detector

In principle, there is no difference in the simulation procedure of EPR experiments between longitudinal and transverse detection, except that the detection operator changes. But with transverse detection of the signal in pulse EPR experiments, the effect of the detector properties on the time-domain signal can be neglected to a large extent, because the detection frequency is equal to ω_{mw} , while the maximum frequency of the response after demodulation of the mw signal is set by the excitation bandwidth of the pulses, which cannot be broader than the width of

the resonator mode $\Delta\omega_{\text{mw}}$, and in most cases it is even somewhat below. $\Delta\omega_{\text{mw}}$ itself is a factor Q_l lower than ω_{mw} , which is usually about two orders of magnitude. Therefore the echo shape is hardly influenced by the quality factor of the resonator.

With LOD, not electron coherence is detected, but the change of $M_z(t)$, which usually has a frequency between a few kHz and about 100 MHz, depending on the experiment and the amplitude of the exciting field. Up to now, the highest detection frequency with LOD was approximately 30 MHz. Consequently, it is inevitable to consider instrumental properties when calculating the time-domain response of the detector to an excitation, especially because a narrowband rather than a broadband detector is used for sensitivity reasons. This detector is a linear input-output system with V_{ind} as its input. An equivalent circuit, which is shown in Fig. 3.2, can be mathematically described with the equation of motion of a harmonic oscillator. It has the form [21]

$$\frac{d^2}{dt^2}Q(t) + \frac{R_S}{L} \frac{d}{dt}Q(t) + \frac{1}{LC}Q(t) = \frac{V_{\text{ind}}(t)}{L}, \quad (3.2)$$

with the inductance L of the coil, the capacitance C and the serial resistance R_S . $+Q(t)$ and $-Q(t)$ are the electric charges on the two electrodes of the capacitor. $V_{\text{ind}}(t)$ is often periodic and can then be written as

$$V_{\text{ind}}(t) = V_0 \cos(\omega t). \quad (3.3)$$

The quantity that is recorded in an experiment is the voltage

$$V_{\Xi}(t) = \frac{Q(t)}{C} \quad (3.4)$$

across the capacitor. It is read out with high impedance and therefore does not influence the equation of motion of the detection circuit. Eq. (3.2) can be rewritten by using the resonant frequency ω_{Ξ} and the quality factor Q_{Ξ} of the LCR circuit instead of L , C and R_S with the relations

$$\omega_{\Xi} = \frac{1}{\sqrt{LC}}, \quad (3.5)$$

$$Q_{\Xi} = \frac{1}{R_S} \sqrt{\frac{L}{C}}. \quad (3.6)$$

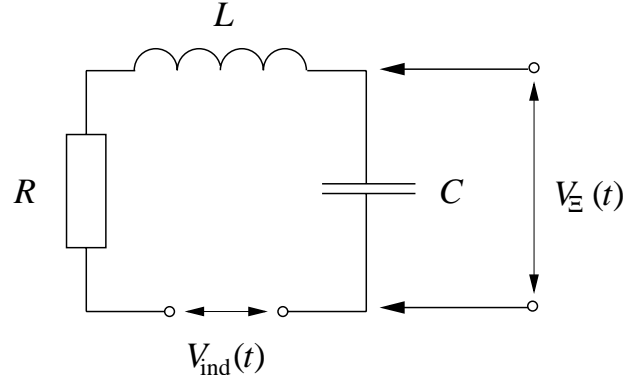


Figure 3.2: Equivalent circuit for the simulation of the response to an excitation V_{ind} .

Now we obtain

$$\frac{1}{\omega_{\Xi}^2} \frac{d^2}{dt^2} V_{\Xi}(t) + \frac{1}{Q_{\Xi} \omega_{\Xi}} \frac{d}{dt} V_{\Xi}(t) + V_{\Xi}(t) = V_0 \cos(\omega t). \quad (3.7)$$

Another important quantity is the time constant

$$\tau_{\Xi} = \frac{2Q_{\Xi}}{\omega_{\Xi}} = \frac{2L}{R_S}, \quad (3.8)$$

which is the ringing time of the LCR circuit. The properties of a serial LCR resonant circuit are summarized in more details in Appendix A.

The simulation of the time trace of a signal is performed by first calculating $M_z(t)$, which is then used to determine V_{ind} . The result is obtained by numerically solving the equation of motion of the detection circuit, using appropriate initial conditions like $V_{\Xi}(0) = 0$ and $dV_{\Xi}(0)/dt = 0$, which is correct if the simulation starts with a fully relaxed detection circuit and if $M_z(0) = M_0$.

3.3 Theoretical Description of LOD Experiments

It is known how to describe magnetic resonance experiments quantum mechanically and solve the corresponding equations numerically. But it is, except for the most simple cases, not possible to obtain analytical equations. Therefore different strategies are used to get some insight into the properties of an experimental scheme. One possibility is to use the classical Bloch equations. Another approach

is to use analytical quantum mechanical formulae for an $S = 1/2$, $I = 1/2$ system, disregarding relaxation. And for special problems, a strategy of starting from a general Hamiltonian and disregarding or simplifying less relevant terms might be successful.

3.3.1 Quantum Mechanical Approach

Attempts to quantum mechanically describe the response of a spin system to an excitation with one or more monochromatic electromagnetic fields without ignoring relaxation [46] make use of the quantized field formalism [47]. The main idea is that considering the external field as a quantized field and extend the system to include radiation makes the Hamiltonian time independent. The determination of the steady-state solution of the equation of motion for the density operator is reduced to the diagonalization of the total Hamiltonian \mathcal{H} of the “system+field” [46]. Using quantized fields is equivalent to the semi-classical treatment due to the exceedingly high number of photons present in all practical situations.

For a spin system irradiated with two mw fields with frequency ω_l and ω_r , the complete Hamiltonian [48]

$$\mathcal{H} = \mathcal{H}_S + \mathcal{H}_R + \mathcal{H}_I \quad (3.9)$$

consists of a Hamiltonian \mathcal{H}_S for the isolated spin system, a radiation Hamiltonian \mathcal{H}_R and an interaction \mathcal{H}_I between the l and r radiations and the spin system. The radiation Hamiltonian is given by

$$\mathcal{H}_R = \hbar \sum_i \omega_i a_i^\dagger a_i, \quad (3.10)$$

where a_i and a_i^\dagger are the annihilation and creation operators, respectively, of a photon with the frequency ω_i , and i being either l or r . The interaction Hamiltonian is

$$\mathcal{H}_I = - \sum_i \boldsymbol{\mu} \mathbf{B}_i = g\beta_e \sum_i (\omega_i/2V)^{1/2} (a_i^\dagger + a_i) S_x, \quad (3.11)$$

with the magnetic moment $\boldsymbol{\mu}$ of the system and the magnetic field \mathbf{B}_i of the i -th wave (again either l or r). V is the volume which contains the radiation field, and

we suppose the magnetic field of the waves to be directed along the x -axis. The density operator σ of the system becomes a dressed operator when the interaction \mathcal{H}_I is switched on, while the density operator σ_R of the radiation field can be considered as unchanged. σ can now be split in a part \mathbf{D} which is affected by relaxation, and a steady-state dressed state $\sigma_{0,D}$, thus becoming

$$\sigma = \sigma_{0,D} + \mathbf{D}. \quad (3.12)$$

Using Eq. (2.15), we get

$$i \left(\frac{\partial}{\partial t} + \Gamma \right) \mathbf{D} = [\mathcal{H}, \mathbf{D}] + [\mathcal{H}, \sigma_{0,D}]. \quad (3.13)$$

The problem is now to obtain the \mathbf{D} matrix. This is described in [11] for an $S = 1/2$ two-level system. The operators of interest are represented using a basis of the kind

$$|m_S, n_r, n_l\rangle, \quad (3.14)$$

with m_S being the magnetic spin quantum number and n_r and n_l are the occupation numbers for the two wave photons. Among the states (3.14), those nearly degenerate in energy are selected. They are then ordered in the succession

$$\cdots, |+\frac{1}{2}, n_r+1, n_l-1\rangle, |-\frac{1}{2}, n_r+1, n_l\rangle, |+\frac{1}{2}, n_r, n_l\rangle, |-\frac{1}{2}, n_r, n_l+1\rangle, \cdots, \quad (3.15)$$

labelling them with $\dots, -2, -1, 0, 1, \dots$. \mathbf{D} can now be written

$$\mathbf{D} = \sum D_{j,k;p,q} a_r^{+,j} a_r^k a_l^{+,p} a_l^q. \quad (3.16)$$

We get $g\beta_e(D_{0,2}-D_{1,3})+c$ for the first harmonic of Ω_m in $M_z(t)$, $g\beta_e(D_{0,4}-D_{1,5})+c$ for the second one, $g\beta_e(D_{0,6}-D_{1,7})+c$ for the third one, and so on, c being a non-relevant constant contribution. The equations for $D_{0,2}$ and $D_{1,3}$ are given by

$$\begin{aligned} (i/T_1)D_{0,2} &= \lambda_r(D_{1,4} - D_{0,1}) + \lambda_l(D_{1,2} - D_{0,3}) + (\omega_r - \omega_l)D_{0,2}, \\ (i/T_1)D_{1,3} &= \lambda_r(D_{0,1} - D_{1,4}) + \lambda_l(D_{0,3} - D_{1,2}) + (\omega_r - \omega_l)D_{1,3}. \end{aligned} \quad (3.17)$$

The different $D_{j,k}$ values are received numerically because especially when both ω_r and ω_l are very close in frequency to the resonant frequency ω_S , several many-quantum processes are excited, and it becomes too difficult to solve the system of

linear equations analytically. But it has been shown in [49] that if $\mathcal{H}_S \gg \mathcal{H}_I$, this approach is equivalent to the Bloch equations [49].

This theoretical approach has been validated first in a nuclear magnetic resonance (NMR) experiment with double rf irradiation to study the existence of multiple quantum transitions [10, 48]. Later, the periodic modulation of $M_z(t)$ with frequency Ω_m in an LOD EPR experiment with double mw irradiation could be explained [44]. Furthermore, it was used to analyze unusual line shape effects in LOD EPR spectra [11]. However, the same was possible more clearly using the Bloch equations [50].

3.3.2 Classical Description Assuming Fast Relaxation

To get a correct description of LOD EPR experiments, relaxation has to be considered in most cases, especially when the mw irradiation is continuous. On the other hand, several properties of this detection method can be explained by considering an $S = 1/2$ system. This permits to use the Bloch equations (2.33). Such a treatment results in analytical expressions, which are easier to analyze than those obtained with a quantum mechanical description, especially when the most relevant situations are considered separately with appropriate simplifications of the formulae.

The first example summarizes the description given by DAVIES [50] where – analogous to the situation in the previous chapter – the sample is irradiated with two mw frequencies, $\omega_r = \omega_0 + \Omega_m/2$ and $\omega_l = \omega_0 - \Omega_m/2$. They are both assumed to be linearly polarized along the laboratory x -axis and to be of equal amplitudes B_1 . The effective transverse field in the rotating frame is seen to be $B_1 \cos(\Omega_m/2t)$.

In one situation relevant in practice, relaxation is fast compared to the inverse of Ω_m ,

$$\Omega_m^{-1} \gg T_1 . \quad (3.18)$$

In this case, $M_z(t)$ can always be represented by its steady-state value, given by

Eq. (2.38). We find that

$$\begin{aligned} M_z(t) &= \frac{1 + (T_2\Omega_S)^2}{1 + (T_2\Omega_S)^2 + a \cos^2(\Omega_m t/2)} M_0 \\ &= \frac{1 + (T_2\Omega_S)^2}{1 + (T_2\Omega_S)^2 + 0.5a(1 + \cos(\Omega_m t))} M_0, \end{aligned} \quad (3.19)$$

where $a = (g\beta_e B_1/\hbar)^2 T_1 T_2$ is the saturation factor. The longitudinal magnetization is thus a periodic function in the difference frequency Ω_m and can be expressed as a Fourier series

$$M_z(t) = \sum_n A_n \cos(n\Omega_m t) + \sum_n B_n \sin(n\Omega_m t). \quad (3.20)$$

B_n are found to be zero because we neglected the phase shift caused by the relaxation, which is still observable even if Eq. (3.18) is fulfilled. According to Eq. (3.1), the signal induced in the detection coil is proportional to

$$-\frac{dM_z(t)}{dt} = \Omega_m \sum_n n A_n \sin(n\Omega_m t). \quad (3.21)$$

If the signal is detected with a lock-in amplifier with reference frequency $n\Omega_m$, it is proportional to $n\Omega_m A_n$. To express A_n , it is convenient to introduce

$$\xi = a/(1 + T_2^2\Omega_S^2). \quad (3.22)$$

For the first two harmonics, we get

$$A_1 = \frac{4}{\xi} \left(1 - \frac{2 + \xi}{2\sqrt{1 + \xi}} \right) M_0 \quad (3.23)$$

$$A_2 = - \left(\frac{4}{\xi} \right)^2 \left(1 - \frac{2 + \xi}{2\sqrt{1 + \xi}} + \frac{\xi}{2} \left(1 - \frac{2 + \xi/2}{2\sqrt{1 + \xi}} \right) \right) M_0. \quad (3.24)$$

This result has two interesting consequences. First, it shows that even when the sample is irradiated with two spectrally pure frequencies without any higher harmonics, the response from the spin system has non-vanishing Fourier components also for $n > 1$. Second, when the line shape is calculated as a function of a ,

not only line broadening, but also a line splitting can be observed at high saturation levels. With a detection frequency equal to Ω_m , this splitting occurs for $a > 2(1 + \sqrt{2}) = 4.828$. This can be fulfilled readily for radicals with long relaxation times, whereas for transition metal complexes at room temperature, line broadening or line splitting requires high mw power. For detection at $2\Omega_m$, the critical condition for line splitting is $a > 4(2 + \sqrt{5}) = 16.94$. Thus more power is required to produce a two-peak structure than with detection at the fundamental frequency.

Eq. (3.23) can now be used to calculate the dependence of $-dM_z(t)/dt$ on a for low mw power levels, *i.e.* $a \ll 1$ and correspondingly $\xi \ll 1$. For this purpose, $\sqrt{1 + \xi}$ is expanded in a Taylor series

$$\sqrt{1 + \xi} = 1 + \frac{\xi}{2} - \frac{\xi^2}{8} + \frac{\xi^3}{16} - \frac{5\xi^4}{128} + \dots \quad (3.25)$$

Then we can approximate

$$A_1 = \frac{4\sqrt{1 + \xi} - 4 - 2\xi}{\xi\sqrt{1 + \xi}} - \frac{2 + \xi}{2} M_0 \approx -\frac{\xi^2}{2\xi\sqrt{1 + \xi}} M_0 \approx -\frac{\xi}{2} M_0, \quad (3.26)$$

using terms up to ξ^2 in Eq. (3.25), and

$$A_2 = -\left(\frac{4}{\xi}\right)^2 \frac{2\sqrt{1 + \xi} - 2 - 2\xi + \xi\sqrt{1 + \xi} - \xi^2/4}{2\sqrt{1 + \xi}} M_0 \approx \frac{\xi^2}{8} M_0, \quad (3.27)$$

using terms up to ξ^4 in Eq. (3.25). Now we get by neglecting higher-order terms

$$-dM_z(t)/dt \approx \Omega_m \left(-\frac{\xi}{2} \sin(\Omega_m t) + \frac{\xi^2}{4} \sin(2\Omega_m t) \right) M_0. \quad (3.28)$$

The same results of the dependence of A_1 and A_2 from a have been obtained with the quantum mechanical methods described in the previous section [51], but it is much more difficult to follow the reasoning there.

From Eqs. (3.26) and (3.27) it is easy to obtain the width of a homogeneous

EPR line with Lorentzian shape. We get for the full width at half height (fwhh)

$$\Delta\omega_{1/2}(A_1) = \frac{2}{T_2} \quad (3.29)$$

$$\Delta\omega_{1/2}(A_2) = \frac{2\sqrt{\sqrt{2}-1}}{T_2} \approx \frac{1.3}{T_2} = 0.65\Delta\omega_{1/2}(A_1). \quad (3.30)$$

$\Delta\omega_{1/2}(A_1)$ corresponds to the natural linewidth, while $\Delta\omega_{1/2}(A_2)$ becomes lower because of the square dependency of the signal from a . In [51], a general expression has been derived for any harmonics

$$\Delta\omega_{1/2}(A_n) = \frac{2\sqrt{2^{1/n}-1}}{T_2}. \quad (3.31)$$

However, an analysis of the linewidth as a function of a is only given for detection at the fundamental frequency Ω_m and at the first harmonic because the signal becomes very weak at higher harmonics.

3.3.3 Classical Description Assuming Low Modulation Depth

A different approach, instrumentally and theoretically, was used by HERVÉ and PESCIA. As mw source, they used a carcinotron [6] with up to 20 W continuous mw power. The amplitude of the mw field

$$\tilde{B}_1 = B_1 (1 + m e^{i\Omega_m t}), \quad (3.32)$$

where m is the modulation ratio, was modulated with $\Omega_m/2\pi$ up to 30 MHz. Eq. (3.32) describes a modulation with a single sideband in the Fourier spectrum of the excitation. To illustrate the relationship between the different amplitude modulation schemes, their Fourier transform is shown in Fig. 3.3. For the theoretical description, a perturbation method was used based on the Bloch equations, assuming that $m \ll 1$. In spite of this assumption, we will see that the result is very generally applicable, and it will be used as foundation to explain the different LOD experiments with continuous mw irradiation and amplitude modulation. The time dependence of the spin magnetization can be approximated by

$$M_z(t) = (M_z)_0 + \epsilon e^{i\Omega_m t} \quad (3.33)$$

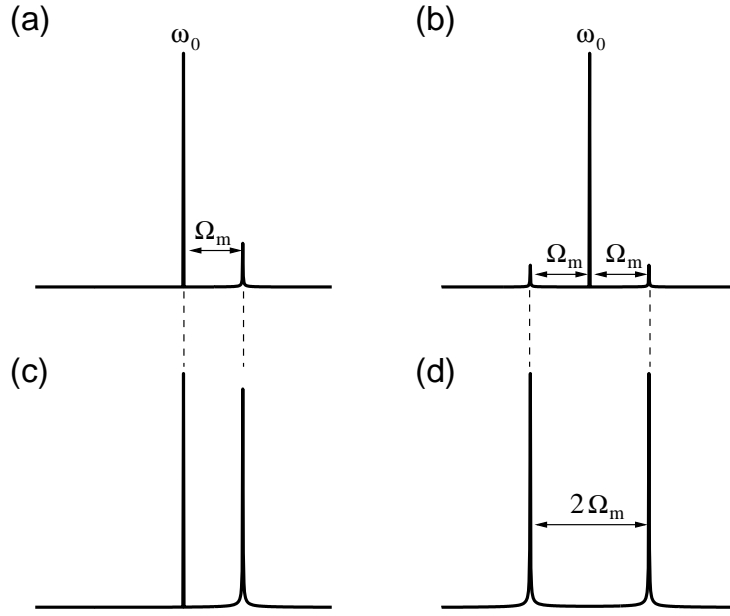


Figure 3.3: Relation between the different cw LOD EPR excitation schemes. Absolute value of the Fourier transform of a modulation of the mw amplitude according to (a) $\tilde{B}_1 = B_1 (1 + m \exp(i\Omega_m t))$ (weak modulation), (b) $\tilde{B}_1 = B_1 (1 + m \cos(\Omega_m t))$ (weak modulation), (c) $\tilde{B}_1 = B_1 (1 + \exp(i\Omega_m t))$ (full modulation), and (d) $\tilde{B}_1 = B_1 \cos(\Omega_m t)$ (modulation of the mw field with frequency Ω and suppressed carrier; analogous to the irradiation of two different mw fields of equal intensity with frequency difference $2\Omega_m$).

with the steady-state value $(M_z)_0$ for $m = 0$, given by Eq. (2.38). The only quantity of interest in (3.33) is ϵ to which our signal is directly proportional. ϵ can be evaluated for a homogeneous line as

$$\begin{aligned}
 \epsilon &= \frac{2amM_0 \left(1 + i\frac{\Omega_m T_2}{2}\right) \left(1 + \frac{\Omega_S^2 T_2^2}{1 + i\Omega_m T_2}\right)}{(1 + a + \Omega_S^2 T_2^2) \left[a + (1 + i\Omega_m T_1) \left(1 + i\Omega_m T_2 + \frac{\Omega_S^2 T_2^2}{1 + i\Omega_m T_2}\right) \right]} \\
 &= \frac{2amM_0}{1 + a + \Omega_S^2 T_2^2} \\
 &\quad \times \frac{0.5\Omega_m T_2(1 - X) + i [1 + X + 0.5\Omega_m^2 T_2^2 X]}{1 + a + X - \Omega_m^2 T_1 T_2(1 - X) + i [\Omega_m (T_1(1 + X) + T_2(1 - X))]}
 \end{aligned} \tag{3.34}$$

with

$$X = \frac{\Omega_S^2 T_2^2}{1 + \Omega_m^2 T_2^2}. \quad (3.35)$$

This formula can be separated into a real and an imaginary part, resulting in an expression of the general form

$$\epsilon = c \frac{\kappa}{\lambda} = c \frac{\kappa \lambda^*}{|\lambda|^2}, \quad (3.36)$$

where both $\kappa = \text{Re}(\kappa) + i \text{Im}(\kappa)$ and $\lambda = \text{Re}(\lambda) + i \text{Im}(\lambda)$ are complex expressions. c does not depend on Ω_m , since a is the average saturation factor and therefore independent of t or Ω_m . We get

$$\text{Re}(\kappa) = 1 + X + 0.5\Omega_m^2 T_2^2 X \quad (3.37)$$

$$\text{Im}(\kappa) = 0.5\Omega_m T_2 (1 - X) \quad (3.38)$$

$$\text{Re}(\lambda) = 1 + a + X - \Omega_m^2 T_1 T_2 (1 - X) \quad (3.39)$$

$$\text{Im}(\lambda) = \Omega_m (T_1 (1 + X) + T_2 (1 - X)) \quad (3.40)$$

$$c = -\frac{2amM_0}{1 + a + \Omega_S^2 T_2^2}. \quad (3.41)$$

To obtain the signal measured in an experiment, we must be aware that the detector is sensitive only to the real part of $M_z(t)$ in Eq. (3.33), which can be evaluated as

$$\text{Re} [(M_z)_0 + \epsilon e^{i\Omega_m t}] = (M_z)_0 + \text{Re}(\epsilon) \cos(\Omega_m t) - \text{Im}(\epsilon) \sin(\Omega_m t). \quad (3.42)$$

In our experiments, \tilde{B}_1 is modulated with $\cos(\Omega_m/2\pi)$, *i.e.* the Fourier spectrum of the excitation shows two sideband, one on each side of the carrier frequency. This can be treated as the sum of two independent modulations with $\exp(i\Omega_m t)$, one rotating with $+\Omega_m$, the other with $-\Omega_m$,

$$\tilde{B}_1 = B_1 (1 + m \cos(\Omega_m t)) = B_1 \left(1 + \frac{m}{2} (e^{i\Omega_m t} + e^{-i\Omega_m t}) \right). \quad (3.43)$$

By adding up the results from the the two perturbations, we get

$$\begin{aligned} M_z(t) &= (M_z)_0 + \frac{\epsilon}{2} e^{i\Omega_m t} + \frac{\epsilon^*}{2} e^{-i\Omega_m t} \\ &= (M_z)_0 + \text{Re}(\epsilon) \cos(\Omega_m t) - \text{Im}(\epsilon) \sin(\Omega_m t), \end{aligned} \quad (3.44)$$

which is identical to Eq. (3.42). The quality of Eq. (3.44) can be checked by comparing some results with $M_z(t)$ calculated by numerically solving the Bloch equations. In Fig. 3.4, this is done for one set of parameters. Fig. 3.4a shows the result for on-resonant excitation, and Fig. 3.4b shows the far off-resonant case. The main error for $a = 0.1$ as well as for $a = 1$ stems from higher-order harmonics

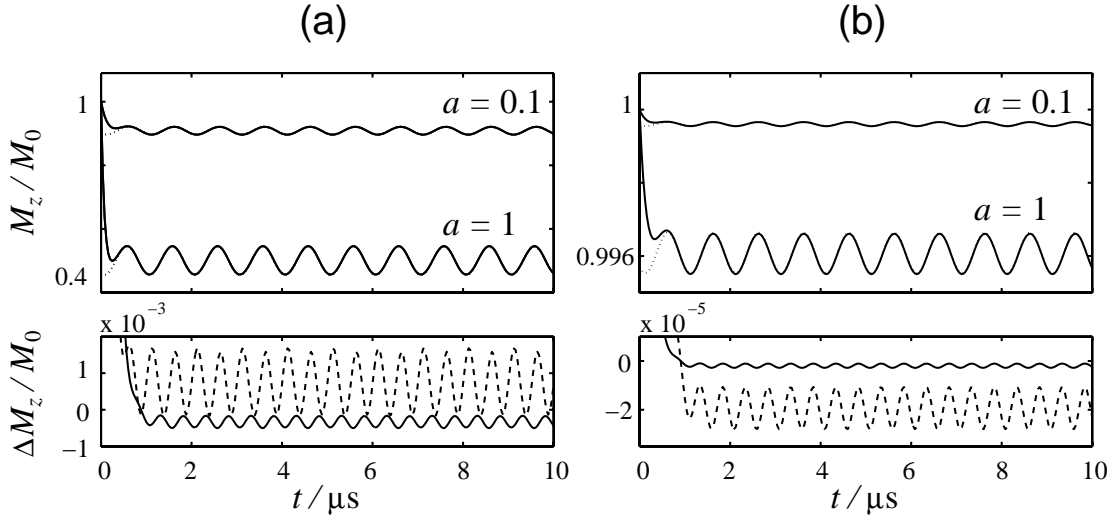


Figure 3.4: Comparison of the result obtained with Eq. (3.44) and numerical solutions of the Bloch equations. The parameters used for the simulations were $m = 0.1$, $\Omega_m/2\pi = 1$ MHz, $T_1 = 1/\Omega_m = 159$ ns, $T_2 = T_1/100 = 1.59$ ns. (a) On-resonant case. (b) Off-resonant case with $\Omega_S/2\pi = 1.6$ GHz. (*upper plots*) Graph of the numerical solution of Bloch equations (solid) and the result of Eq. (3.44) (dotted) far below ($a = 0.1$) and with considerable saturation ($a = 1$). (*lower plots*) Difference between the results with the two simulation methods for $a = 0.1$ (solid lines) and $a = 1$ (dashed lines).

which are neglected in Eq. (3.44) and the fact that this equation describes an oscillatory steady-state solution. Thus one has to wait until this state is reached with the numerical solution of the Bloch equations.

The next question is how Eq. (3.44) behaves for large modulation amplitudes up to $m = 1$. This has been simulated numerically with the same parameters as were used for Fig. 3.4, and from these time traces, the signal induced in the detector at the fundamental frequency was determined by calculating $dM_z(t)/dt$ according to Eq. (3.1). This way, the problem that the determination of $(M_z)_0$ using Eq. (2.38) becomes inaccurate for large m can be avoided because constant

contributions drop out when calculating the temporal derivative. The result is illustrated in Fig. 3.5 as the difference Δs between the signals of the two methods relative to the signal s_{HP} obtained with the formula of HERVÉ and PESCIA, whose time derivative can be determined as

$$\frac{dM_z(t)}{dt} = -\Omega_m (\text{Re}(\epsilon) \sin(\Omega_m t) + \text{Im}(\epsilon) \cos(\Omega_m t)) , \quad (3.45)$$

and the phase φ , ignoring phase shifts induced by the detection circuit or amplifiers, becomes

$$\tan(\varphi) = \frac{\text{Re}(\epsilon)}{\text{Im}(\epsilon)} = \frac{\text{Re}(\kappa) \text{Re}(\lambda) + \text{Im}(\kappa) \text{Im}(\lambda)}{\text{Re}(\lambda) \text{Im}(\kappa) - \text{Re}(\kappa) \text{Im}(\lambda)} . \quad (3.46)$$

Although Eq. (3.44) has been derived by explicitly assuming that $m \ll 1$, its result is still good for $m = 1$ far below saturation and acceptable up to $a \approx 1$ if the signal induced in the detector at the fundamental frequency Ω_m and not $M_z(t)$ is the property of interest. Therefore it will be used to discuss all the different variations of LOD EPR experiments with continuous excitation and amplitude modulation, not only the ones with a small cosinusoidal perturbation of the mw amplitude.

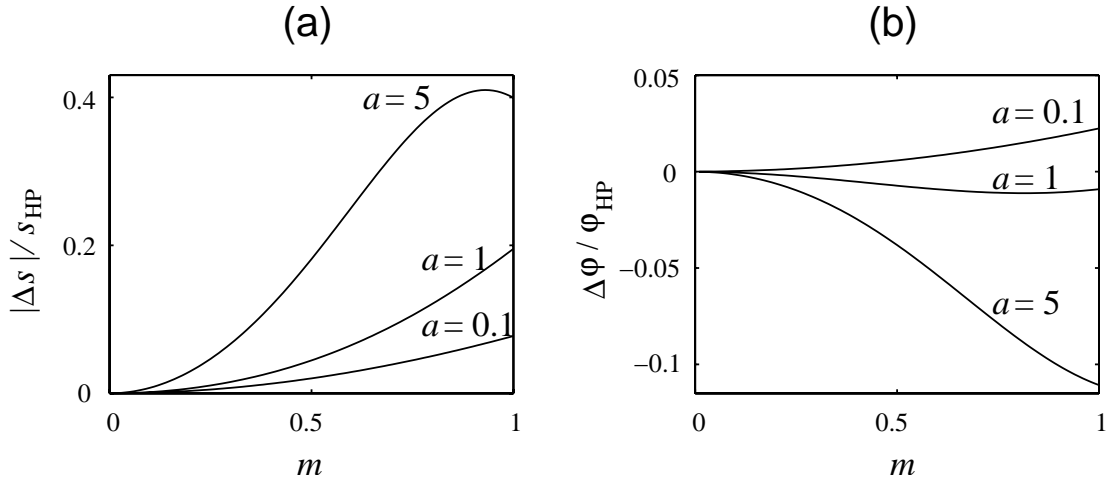


Figure 3.5: Relative error of Eq. (3.44) compared with the numerical solution of the Bloch equations as a function of m when the signal is detected at the fundamental frequency of the amplitude modulation Ω_m . The parameters used for the simulations were $\Omega_m/2\pi = 1$ MHz, $T_1 = 1/\Omega_m$, $T_2 = T_1/100$, and $\Omega_S = 0$. (a) Error of the signal at $a = 0.1$, $a = 1$, and $a = 5$. (b) Error of the phase with the same saturation factors.

3.4 Instrumentation Used for LOD EPR

3.4.1 Generation of an Amplitude Modulated MW Field

An amplitude modulated (am) mw field can be created in different ways. The least demanding is the use of a continuous mw source like a klystron, whose output is square-modulated with an mw switch. This switch can be controlled with an arbitrary function generator (AFG). If more power is required, a high-power mw amplifier can be inserted after the switch. The advantage of this setup is its simplicity, the disadvantage is its limited flexibility to produce arbitrary modulations of the mw amplitude.

A more advanced variation of this scheme uses an mw mixer with the IF input driven by an AFG to produce the amplitude modulation of the mw field. With this setup, an arbitrary modulation of the mw field is possible, including negative values corresponding to a phase inversion of the mw field when the voltage at the IF input is negative.

Equivalent to an amplitude modulated mw field is to use two frequency stabilized mw sources with frequencies ω_l , ω_r , differing by $\Omega_m \ll \omega_r, \omega_l$ [52]. The modulation depth can be adjusted easily by changing the relative amplitude of the two mw fields, but the modulation can be only cosinusoidal, and the relative stability of the two mw fields must be very high, making this method instrumentally more demanding than the previously described methods. As an alternative, a single Impatt diode, whose bias current is modulated, can be used [53].

Another possibility is to use a carcinotron [3, 6] – a high-power mw source whose output power can be directly modulated by applying an alternating cathode voltage. This setup has approximately the same flexibility than the one using two mw fields, without the need to frequency-stabilize two sources. But this setup cannot be used for transversely detected EPR experiments, thus its application is limited.

The situation is different for pulse LOD experiments [13]. In this case, several pulse channels, equipped with high-speed mw switches, are available. Like in transversely detected pulse EPR, the magnetization can be manipulated flexibly with pulses of different length, amplitude, and phase. The pulses can be controlled

in the usual way with a pulse programming unit. The problem is that most of these units allow only a limited number of pulses per shot, for example 31 pulses with a Bruker E580 pulse console. The other problem is that usually a high-power TWT amplifier with a limited duty cycle is used. Mainly for samples with short relaxation times, this can be a reason for reduced sensitivity with a fixed recording time.

A different approach was chosen by BLOEMBERGEN and DAMON ([1], see also [34, 54]). They used a magnetron to create 50 kW pulses of 1 μ s length with a repetition rate of 500 Hz to investigate ferromagnetic samples. The mw field amplitude was up to 50 G in the cavity.

3.4.2 Resonator and Pick-up Coil

The majority of LOD experiments were performed using a rectangular cavity [6, 11, 54]. In the first EPR experiments with LOD [1, 54] for example, the sample was placed at the wall of a rectangular cavity, separated with a silver foil of a few micron from the detection coil outside the cavity. A pick-up coil can also be placed inside a rectangular cavity. In [55] a saddle-shaped pick-up coil was wound around the tube containing the sample. In the same paper, setups with a helical resonator operating at 0.2 GHz and a 0.7 GHz strip-line resonator, again with a saddle-shaped detection coil inside the resonator, were presented.

In [13] a bridged loop-gap resonator (BLGR) was used, identical to the BLGR for conventional pulse EPR experiments. The detection coil had 600 turns and was placed outside the resonator and the mw shield, which reduces the filling factor of the coil considerably. In a similar setup [45], a two-loop-one-gap resonator and a pick-up coil with 700 turns was used. The coil was placed outside the resonator, but inside the mw shield. This was possible because the coil was made of a wire with a diameter of only 0.05 mm. The drawback of thin wire is its low conductivity and high losses.

For large samples at low excitation frequencies, *e.g.* small animals for EPR imaging, a birdcage resonator can be used [14] where the detection coil can be placed again inside the resonator.

For a conceptual study [56], no resonator was used at all. A single-turn coil

was wound around the sample for excitation, and the saddle-type pick-up coil was pasted on a cylindrical quartz glass tube.

In this thesis, an mw setup with a dielectric ring resonator is presented, and detection is done with a saddle coil with a high filling factor.

3.4.3 Detector

There was a large number of different instrumental approaches for LOD. The one thing common in all LOD work is the use of a pick-up coil to detect the signal. This coil can be integrated into a resonant circuit [2, 13], or broadband detection can be performed [54]. Unfortunately, many of the authors do not describe the details of this part of their setup, although it is of major significance for the sensitivity and the behaviour of the detector.

The signal can be recorded in two different ways. Both of them have been described in the original papers [34, 54]. In the first variant, which is only sensible with pulse excitation, the transient signal is recorded with an oscilloscope or a transient recorder, triggered by the same source as was used for the experiment. The full response of the detector to an excitation is recorded, and the maximum available information is obtained. In the second variant, one spectral component, often equal to the repetition rate of the experiment or the frequency of the amplitude modulation, is selectively read out with a lock-in amplifier.

3.5 Applications of LOD

3.5.1 Relaxation Time Measurements

The major number of applications with LOD focuses on the measurement of spin-lattice relaxation times, which is more straightforward than with conventional detection techniques because of the sensitivity of the detector to spin polarization changing in time. The different methods presented up to now are briefly summarized in this section.

DAMON [54] and BLOEMBERGEN, WANG [34] presented two saturation methods where first a very strong mw pulse of 1 μ s duration was applied. In the conceptually simpler one of the two methods, the recovery of M_z after the pulse was

observed transiently with an oscilloscope. This requires T_1 to be longer than the fall time of the pulse. An equivalent method was used in [57] at high mw frequencies. In the second method, the signal was processed with a lock-in amplifier at the frequency of the pulse repetition rate. It is proportional to the difference between the steady-state magnetization during mw irradiation and the magnetization at Boltzmann equilibrium. This signal was recorded as a function of the mw field amplitude B_1 , and from this curve T_1 could be determined.

SCHWEIGER and ERNST [13] applied two consecutive π pulses, separated by time τ . The first pulse inverts the spin magnetization, and the second pulse samples the residual magnetization by bringing it back along z . τ is incremented, and the signal is detected with a lock-in amplifier at the repetition rate of the experiment. The signal induced in the coil by the first pulse is identical in each experiment and can be subtracted, and the signal induced by the second pulse gives directly the relaxation curve.

COLLIGIANI *et al.* [58] made an experiment where a low-power pulse of $1 \mu\text{s}$ length was applied, and the signal was recorded as a function of the pulse repetition frequency.

LEVANON, KWAN, and WEISSMAN [9] excited organic compounds with a laser flash into a triplet state and observed the signal, which is proportional to $dM_z(t)/dt$, as a function of time after the excitation. In this experiment, phosphorescence processes are superimposed to the spin relaxation, making the interpretation of the data non-trivial.

Besides these pulse methods, different experiments to measure T_1 with continuous mw irradiation and modulation of the mw amplitude have been developed. One approach was to record the signal as a function of the amplitude modulation frequency Ω_m [6]. Eq. (3.34) can be used to derive a theoretical formula for the curve, and fitting this analytical expression to the experimental data yields T_1 . Very short values of T_1 down to 10^{-10} s [59] can be measured this way. Unfortunately, this method is not free of drawbacks. On the one hand, the output of the detector may depend on Ω_m that is swept over a wide frequency range. This effect must be corrected with a setup-dependent calibration function. If detection is done with a resonant circuit tuned to Ω_m , the resonance frequency has to be swept

synchronously with the amplitude modulation frequency. On the other hand, the relaxation pattern is not obtained directly, but a formula based on the Bloch equations must be fitted to the data. The quality of the result strongly depends on the correctness of this formula for a specific sample. To get a comprehensible formula which can be handled easily, different assumptions concerning the homogeneity of the EPR lines, the ratio T_1/T_2 , $\Omega_m T_1$, $\Omega_m T_2$, and the saturation have to be made. The same idea of varying Ω_m was used in [60]. In this case, a more sophisticated theoretical background was used, considering also nuclei coupled to the unpaired electron [61]. For the experimental implementation, the sample was irradiated with two weak mw fields differing in their frequency by Ω_m . It was pointed out that with high mw power as used in [6], where a transition is saturated, this method gives an effective longitudinal relaxation time $T_1^{(\text{eff})}$, arising from the sum of all relaxation paths including nuclear and cross relaxation between observed levels. $T_1^{(\text{eff})}$ usually differs from T_1 except for two-level systems. On the other hand, the sensitivity of this method is very poor when weak mw fields are used.

In a similar approach [62], the phase of the signal detected with a lock-in amplifier was recorded as a function of Ω_m . Ω_m was increased stepwise and could have one of twelve values between 70 kHz and 1 MHz. For each of them, a calibration value was determined to correct for the quality factor of the detection circuit. The phase was calibrated previous to an experiment with a DPPH sample. This calibration procedure is crucial for the success of the method. The relaxation times of the test sample must be known very accurately, and in the optimum case a test sample with similar relaxation properties as the sample under investigation should be used. This method was used in an oximetry experiment where T_1 was recorded for different oxygen concentrations.

In a different experiment [63, 64], the ratio of the LOD signal intensity to the transverse EPR signal at a fixed Ω_m was used to determine very short T_1 values of rare earth complexes down to 10^{-10} s.

One of the main features of LOD EPR is its different dependence of the signal on relaxation times compared with transversely detected EPR [65]. This can easily be seen for low mw power from Eq. (3.23). The on-resonant signal in LOD EPR is proportional to the saturation factor a , which is proportional to $T_1 T_2$, while

with transverse detection the signal under non-saturating conditions is proportional to T_2 , which is derived in detail in several textbooks, *e.g.* [16]. In [11], T_1 is estimated by comparing the signal of an LOD EPR experiment using double mw irradiation with a cw EPR signal obtained under the same conditions. The method can be extended to inhomogeneously broadened lines, provided that all the spectral components have the same T_1 .

In [62], another way to determine T_1 is presented. The area A under the LOD EPR spectrum is calculated for homogeneous and inhomogeneous lines as

$$A = C \frac{T_1}{\sqrt{1 + \Omega_m^2 T_1^2}}, \quad (3.47)$$

where C is a constant and contains the inhomogeneous linewidth, the Larmor frequency, and scaling factors. With this formula, it is possible to determine T_1 by measuring the whole LOD EPR spectrum with different values of Ω_m and then calculating the area under this spectrum. But maybe even more useful, especially in oximetry where one has to deal with oxygen concentrations changing in time, is the use of this method to monitor the change of T_1 relative to a starting value.

3.5.2 EPR Measurements

A common application of LOD is the measurement of EPR spectra. The general outline of such experiments has been given in the theoretical section of this chapter – excitation is done usually either by irradiating the spin system with two different mw frequencies, or by amplitude modulating the mw field. Although LOD EPR is especially for narrow EPR lines less sensitive than standard cw EPR, it is sometimes useful to perform such an experiment because of its supplemental properties compared with transversely detected EPR. In analogy to a pulse EPR experiment, the absorption spectrum rather than its first derivative is obtained. This is mainly an advantage for spectra with very broad lines, where the usual field modulation can be problematic because of its limited modulation amplitude and stability of the baseline in the integrated spectrum, or if broad and narrow lines appear in the same spectrum. LOD EPR does not require the existence of an echo and is free of instrumental deadtime.

While the first experiments with LOD focused on the determination of T_1 relaxation times, the first field-swept EPR experiments, using two different mw fields, were reported two decades later [44], although WHITFIELD and REDFIELD [2] already showed their feasibility. The reason could be the low sensitivity of the setups or the high mw power needed to obtain acceptable signals in the first experiments, which would lead to considerable power broadening for most samples. The setup of MARTINELLI *et al.* was the first one where only low mw power – on the same order as in conventional cw EPR – was applied. Later, the possibility of detecting the signal at higher harmonics of the difference frequency between the two fields was considered, and the effect on the intensity and the linewidth was calculated [11, 50, 66].

SCHWEIGER and ERNST [13] presented another possibility to measure EPR spectra with LOD. They used high-power mw pulses to invert the magnetization. This inversion and the following recovery caused by spin-lattice relaxation induced a signal in the detection coil that was read out with the repetition frequency of the experiment, using a narrow-band detector. The width of the resonance line is determined by the excitation bandwidth of the pulses, analogous to electron spin echo detected EPR. A variation of this method [58, 67] uses low-power pulses, which in turn are prolonged compared with the high-power pulses. On the other hand, no high-power mw amplifier with a limited duty cycle has to be used, allowing for a higher pulse repetition rate. This way, the pulses can be enlarged up to the limit of a cw LOD EPR experiment with square-wave modulation, where the length of the pulses and the time without mw irradiation are equal.

In favourable cases the different relaxation time dependence of the signal in LOD EPR and conventional cw EPR can be used to disentangle spectra of samples with more than one component just by comparing the measurements with the two detection techniques. In [68], an $\text{MnO}:\text{MnCl}_2$ system was analyzed in this way. A similar approach was used in [8, 69] to study the antiferromagnetic material $\text{N}(\text{CH}_3)_4\text{MnCl}_3$, where additionally to the comparison between the spectra obtained with the two detection techniques, LOD EPR spectra were recorded with different modulation frequencies.

As a further application, LOD was used to measure conducting electron spin

resonance of metal samples [70]. With reflection spectrometry, the phase shift and amplitude variation of the mw field inside the skin depth, combined with the magnetization diffusion via the conducting electrons, results in a distortion of the EPR line, which becomes asymmetric and is no longer proportional to the imaginary component χ'' of the magnetic susceptibility. Theoretical correction diagrams are needed to extract g and T_2 from the experimental line shape. An amplitude modulated mw field with LOD makes it easier to determine these parameters. In most cases it provides a signal proportional to χ'' .

3.5.3 LOD ESEEM

SCHWEIGER and ERNST [13] performed a standard two-pulse ESEEM experiment free of instrumental deadtime. As the detector sequence, a $\pi/2$ pulse was applied at the position of the echo, transferring the magnetization to the $-z$ direction. The induced signal is proportional to the echo intensity. The detection circuit is tuned to the repetition rate of the experiment, and the signal is read out with a lock-in amplifier.

3.5.4 Conceptual Studies

LOD is the method of choice to verify the validity of formulae which describe the behaviour of spin polarization in magnetic resonance experiments because its direct sensitivity to the time derivative of this property. One study of this kind was made by WHITFIELD and REDFIELD [2] to test the predictions of the modified Bloch equations for large rf fields. They found a good coincidence between theory and experiment.

Another conceptual study was done by SATO *et al.* [56] who built a setup where the signal could be measured in a wide frequency range. They have shown that the relationship of the signal intensity as a function of the resonant frequency is linear as predicted by theory if instrumental influences are avoided or corrected. However, instrumental factors are of major importance for the dependence of the signal intensity vs. the detection frequency. This has been analyzed by POOLE [16] for cw EPR experiments, and in a recent publication by RINARD *et al.* [71] for

setups usually used for pulse EPR experiments.

3.5.5 EPR Imaging with LOD

In [14] and other studies since then [72–74], it has been shown that some of the most striking problems in *in vivo* EPR imaging can be circumvented by using an amplitude modulated rf field and LOD. The advantages compared to conventional detection are that with biological samples the filling factor of the LOD coil can be much larger than it is possible for EPR resonators operating in the region of 300 MHz. Furthermore, loading the resonator with an animal at such frequencies can reduce its loaded quality factor Q_l by an order of magnitude, while Q_{Ξ} , with $\omega_{\Xi}/2\pi$ of a few hundred kHz, is not significantly degraded. Additionally, Q_{Ξ} is not strongly reduced by conducting samples. However, higher rf power is still required to obtain a certain field strength. A further advantage of LOD is the lower sensitivity to motions of living animals due to respiration, heartbeat, and blood flow, which affects the resonant properties of the EPR cavity. Another consideration is that LOD does not suffer from power limitations [75], and larger irradiation power levels can therefore be used. The spectrometer design is simple, and the only high-frequency components required are the signal generator and the rf amplifier needed to excite the EPR resonance.

Chapter 4

Instrumentation

Other than with conventional detection methods, with LOD the excitation and the detection channel are completely separated from each other as long as the detection frequency is far from the mw frequency used for excitation. There is no deadtime, and it is not even necessary to protect the detector against high mw power. The excitation and the detection channel can be optimized separately. Additionally, a detection setup at low temperatures would benefit fully from the increased noise figure because no mw device at room temperature is coupled to it. The drawbacks are mainly in connection with sensitivity. The detection frequency is three orders of magnitude lower, and it is impossible to design a detection circuit with a loaded quality factor Q_{Ξ} as high as the Q_I of an mw resonator in cw EPR.

In previous work with LOD, dedicated spectrometers with probeheads designed especially for this purpose have been used, which needed a lot of experience to be built. One of the intentions of this work was to use a commercially available spectrometer and probehead, adding only a minimum of additional devices. With the setup presented in this chapter, LOD becomes available for the first time to a large number of researchers without the need of additional investments.

It is known that an inhomogeneous B_1 field has a major impact on the result of nutation experiments [25]. Because one of the experiments presented later uses nutation pulses to induce a signal, the distribution of B_1 in our dielectric ring resonator is investigated in some detail. Finally, the detector is characterized by calculating the theoretical sensitivity that can be obtained with this setup.

4.1 Spectrometer

Our setup is based on a Bruker X-band pulse EPR spectrometer. Experiments have been performed using an ESP-380-1010 mw bridge with eight pulse channels and an ElexSys E-580 console with 2 ns time resolution, which is suited for cw LOD as well as pulse LOD EPR. A schematic drawing of the full setup is shown in Fig. 4.1.

4.1.1 Pulse Excitation

For pulse LOD experiments, a modification of the excitation channel is not required. The mw pulses are formed in the mw bridge of the E-580 spectrometer and amplified up to 1 kW with a traveling-wave tube (TWT) amplifier (Applied System Engineering Inc. 117X) with a duty cycle of 1 %, analogous to transversely detected pulse EPR experiments.

4.1.2 Continuous Wave Excitation

To perform cw LOD experiments, the spectrometer has to be supplemented by additional devices. The cw mw power is taken from the *AUX* output of the mw bridge. Its amplitude is modulated either with an mw switch (M/A-Com 2662-0106) for square-wave modulation, or with a double balanced mixer (Miteq MO 812) for arbitrary modulations. The driving signal for the mw modulators is delivered by an AFG (LeCroy LW 420). The modulated signal is then amplified with a 15 W solid state cw mw amplifier (CTT ASN 096-4242). The power level at the output of the mw amplifier is adjusted by a rotary vane attenuator (Sivers Lab PM 7101X). The isolators are used to generate an mw amplitude modulation free of reflections (Ryt 200102) and to absorb reflections caused by the overcoupling of the probehead (Narda 60583).

4.2 Probehead and Resonator

In the LOD setup, the probehead connects the excitation with the detection path of the spectrometer. With mw detection, this task is normally displaced from the

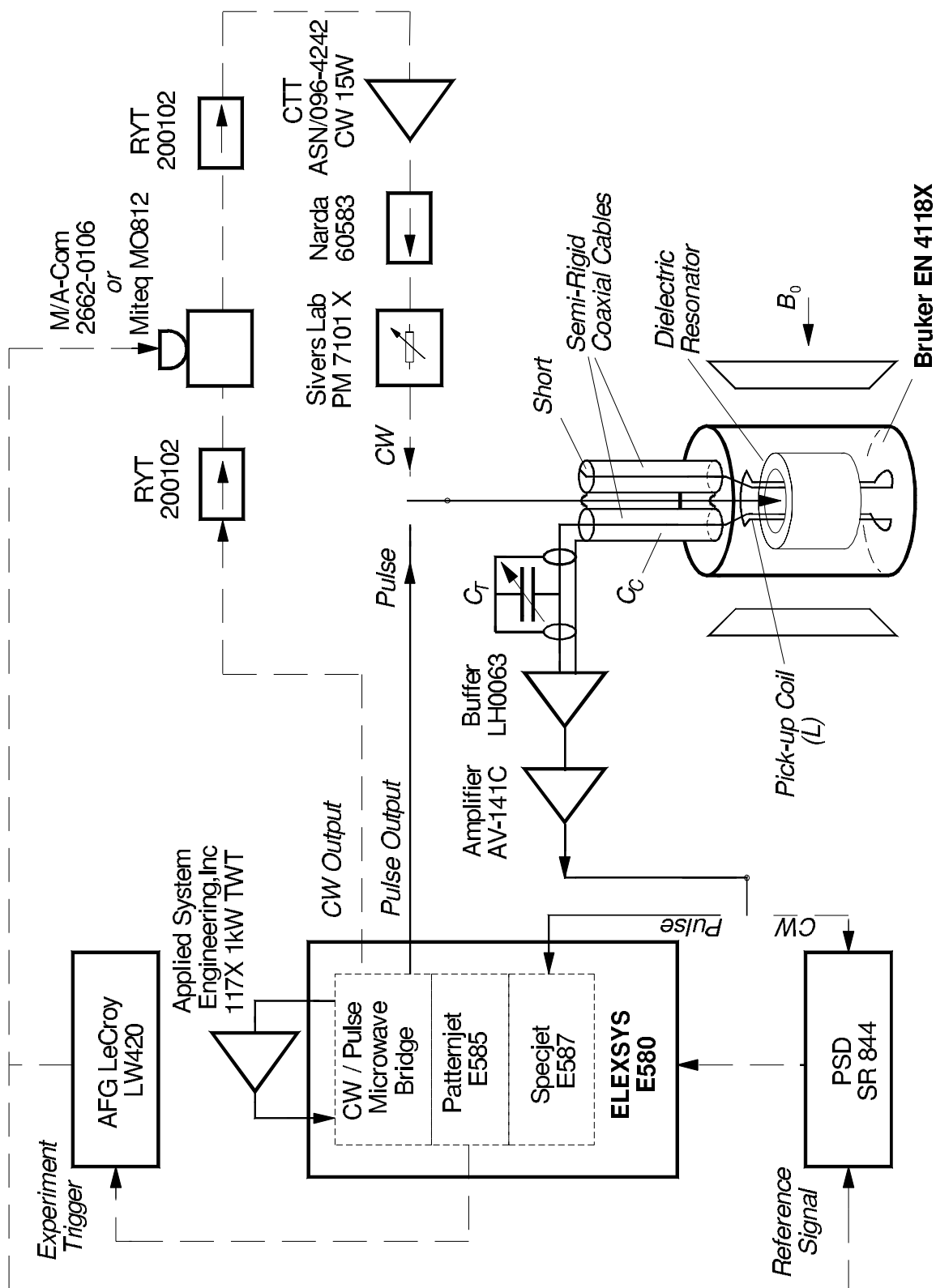


Figure 4.1: Experimental setup used for LOD EPR experiments based on a Bruker ELEXSYS E-580 pulse EPR spectrometer with a pulse ENDOR probehead rotated by 90° about the sample axis. The parts connected by dashed lines are used for cw LOD EPR only.

probehead by using a circulator. In our LOD setup, excitation is done at X-band in the region of 10 GHz, while detection is done at radio frequencies in the region of 10 MHz. This requires the combination of two resonance structures separated in their operating frequency by three orders of magnitude, coupled only by the magnetization of the sample. As LOD experiments usually suffer from sensitivity, the design of the rf detection coil has to be optimized carefully. According to Eq. (3.1), the coil should have a maximum number N of turns and should be as close to the sample as possible for optimum sensitivity. On the other hand, the coil is integrated into a resonant circuit. Therefore N is limited by the maximum inductance L of the coil for a given resonance frequency ω_{Ξ} of the detection circuit and the available space, and the wires have to be arranged such that they are oriented perpendicular to the electric field component of the mw field.

Dielectric resonators are well suited for both pulse and cw EPR experiments. Their Q_l values can be adjusted between 80 (maximally overcoupled with power reflection of approximately 99 %) and 5000 (critical coupling). Furthermore, a coil positioned inside the dielectric ring close to the sample has only a small influence on the mw properties of this type of resonator. With LOD, there are no instrumental limitations such as the deadtime that impose restrictions on the choice of Q_l of the mw resonator. Therefore it can be optimized just by considering spectroscopic and sensitivity criteria. For pulse LOD experiments, the resonator was strongly overcoupled to obtain well-defined pulse shapes. For cw LOD experiments the quality factor Q_l has to be chosen such that the bandwidth of the resonator ω_{mw}/Q_l is larger than the frequency difference between the mw sidebands caused by the amplitude modulation. Otherwise the signal intensity is remarkably reduced. In addition, the two sidebands may have different intensities if ω_{mw} is not equal to the center of the resonator mode.

Several of the requirements listed above also hold for electron nuclear double resonance (ENDOR) experiment. But there, the rf coils are stressed with high rf voltages, while in LOD only small voltages of a few μV have to be detected. However, because in pulse ENDOR the average rf power is much lower than the peak power during the pulses, it is possible to use small coils made of thin wire, which has been implemented in the Bruker X-band pulse ENDOR probehead (EN

4118X). The wire of the rf coil is guided inside the dielectric ring in four grooves parallel to the sample axis and returns outside the dielectric body. The coil is thus very close to the sample tube with a 3.8 mm outer diameter, resulting in a much higher filling factor than in all coil arrangements previously used for LOD experiments. We performed our LOD experiments with such a commercial probehead, rotated around the sample axis by 90° , and used the rf coil, which is then oriented parallel to \mathbf{B}_0 , as a pick-up coil.

4.3 Detection Setup

4.3.1 Resonant Circuit

To get a reasonable sensitivity, the rf coil used to detect the signal has to be integrated into a resonant circuit. To leave the probehead unchanged, additional devices have to be added on the outside by using the rf connectors. The simplest resonant circuit would be a serial LCR circuit, its implementation requires a minimum of additional devices. The rf coil of the ENDOR probehead with an inductance $L \approx 2.6 \mu\text{H}$ is used for signal detection. One of the two semi-rigid 50Ω coaxial cables, which connect the coil with the rf connectors at the outside of the probehead, is shorted. This adds an inductive part with $L_C \approx 0.15 \mu\text{H}$, which is not considered in the following. The second semi-rigid coaxial cable has a high impedance termination and acts as a capacitor with $C_C \approx 50 \text{ pF}$ between coil and ground. These components of the probehead already form a serial LCR resonant circuit with a resonance frequency $\omega_{\Xi}/2\pi = 1/(2\pi\sqrt{LC}) \approx 14 \text{ MHz}$ and a quality factor $Q_{\Xi} = R_S^{-1} \sqrt{L/C} \approx 150$ at room temperature. The resistance of the coil represents the main contribution to the serial resistance R_S . In going from room temperature to liquid helium temperature, Q_{Ξ} increases by a factor 2-3. If the first semi-rigid coaxial cable is open ended, ω_{Ξ} increases by about a factor $\sqrt{2}$. To adjust the resonance frequency of the detection circuit, a tuning capacitor with $C_T = 5 - 15 \text{ pF}$ in parallel to C_C is used. The signal is detected as the voltage across capacitance $C = C_C + C_T$. A schematic drawing of the detection circuit is shown in Fig. 4.2. It is obvious that this is not a pure serial LCR circuit anymore, but it deviates only little from this simple scheme if the capacitors have low losses,

i.e. a high internal resistance R_C , which is fulfilled with the components used for this setup.

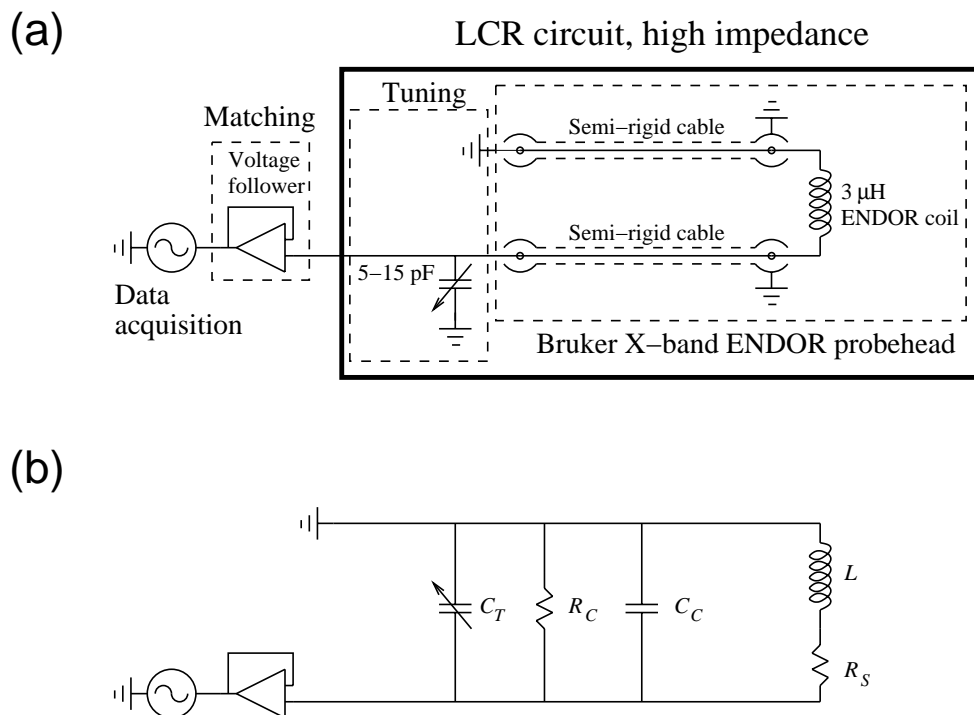


Figure 4.2: (a) Scheme of the resonant circuit for longitudinal detection. It consists of three parts: the X-band ENDOR probehead EN 4118X from Bruker, a tunable air capacitor to adjust the resonance frequency ω_{Ξ} , and a voltage follower to actively match the impedance of the circuit to the 50Ω input of a video amplifier. (b) Equivalent network to simplify the description and simulations of the resonant circuit.

4.3.2 Impedance Matching

Because there is no high power on the detection circuit at any time during the experiment, the impedance matching between the resonant circuit and the 50Ω input of an rf preamplifier can be done actively with a buffer amplifier (National LH 0063), used as a voltage follower. The advantage compared to a passive matching is that Q_{Ξ} is not reduced by the transformed input impedance of the rf amplifier. Since the utilized buffer amplifier is a broadband device, it is easy to handle because no adjustment to the exact ω_{Ξ} is necessary, and it is also very flexible because it can be used for experiments where signals at other frequencies than ω_{Ξ} are of

interest. The drawback is, as usual when using broadband devices, the increased noise figure.

4.3.3 Rf Preamplifier

When a resonant circuit with a high Q_{Ξ} is used, detection has to be done at ω_{Ξ} to get optimum sensitivity. The setup described above with the Bruker ENDOR probehead is well suited for the range of ω_{Ξ} between 5 and 25 MHz. This imposes no special demands on the specifications of the rf preamplifier following the detection circuit, also because there is no high input power at any time during the experiment. In principle, a commercially available device with a very low noise figure and an input and output impedance of 50Ω could be used. However, to get a setup as flexible as possible, a broadband preamplifier (Avtec AV-141C, 20 dB gain) has been chosen with a bandwidth from direct current (DC) to 600 MHz. The reason for this choice becomes evident in the chapter about relaxation time measurements, where an experiment is presented that depends on a broadband amplification of the signal. The drawback in this case is not only the increased noise figure, but also that the output impedance of the device is 3Ω rather than 50Ω , which is the default input impedance of most of the subsequent recording devices like lock-in amplifiers or transient recorders. Fortunately, the AV-141C is capable to drive a device with an input impedance of 50Ω without distortions in the frequency range up to 100 MHz that is of interest in our experiments.

4.3.4 Recording Device

The choice of the recording device depends on the type of experiment. For pulse experiments, the full time trace of the signal during and after the excitation can be recorded with a resolution of 4 ns using the SpecJet transient recorder and signal averager built into the Bruker E580 spectrometer console. With this recorder, a large amount of data accumulates that has to be reduced later. With spectrometers without a transient recorder, it is also possible to use an external one, for example a digital oscilloscope like the LeCroy 7200 that has a time resolution up to 1 ns, but the maximum repetition rate is only about 100 Hz, and data transfer to the console

is much slower. Another possibility for certain experiments is to integrate with a boxcar averager over that part of the signal that contains the information. This is the standard way of data collection in transversely detected pulse EPR experiments, and phase or B_1 cycles can be applied directly, which is not possible with external transient recorders where every phase step must be recorded separately and processed afterwards.

For cw LOD EPR experiments, the signal from the preamplifier is demodulated with a phase sensitive detector (PSD; Stanford Research Systems SR 844). The reference frequency is from the AFG that generates the amplitude modulation. The output of the PSD is recorded with the boxcar averager of the spectrometer.

4.4 Quantization of the B_1 Inhomogeneity

4.4.1 Distribution of B_1 Over the Sample Volume

If the distribution of B_1 in a resonator is considered in a simulation, usually a Gaussian distribution is assumed, neglecting the dependence on the type of resonator that is used [26, 76]. A general procedure to determine this distribution, which is equivalent for all resonators, is presented in the following. In a first step, B_1 in the resonator must be measured as a function of the sample position, and a mathematical function must be selected to model this distribution. Afterwards this function must be expressed as a probability distribution $p(B_1)$, because one is interested in the fraction of sample at each value of B_1 rather than in $B_1(h)$ at a certain position h within the resonator. In a numerical simulation, only a discrete number of Hamiltonians $\mathcal{H}(B_{1,j})$ at different values of B_1 can be evaluated. For each of them we need a weight function $w(B_{1,j})$ that is defined as the integral of $p(B_1)$ between two anchor points $B_{1,i}$ and $B_{1,i+1}$. The minimum value of $B_{1,i}$ is denoted as $B_{1,\min}$ and the maximum value as $B_{1,\max}$. $B_{1,\min}$ is determined by the sample height and the distribution of $B_1(h)$, and it is proportional to $B_{1,\max}$, therefore the ratio

$$d = \frac{B_{1,\max}}{B_{1,\min}} \quad (4.1)$$

is constant for a given sample and resonator. $B_{1,j}$ is chosen at a point in between $B_{1,i}$ and $B_{1,i+1}$. This is often, but not necessarily, at $B_{1,j} = (B_{1,i} + B_{1,i+1})/2$. This

sketch to determine $w(B_1)$ is concretized in some detail for a dielectric ring resonator in Appendix B, because all the experimental results presented here were measured with such a resonator. When a Gaussian distribution of $B_1(h)$ is assumed, the B_1 dependent weight function has the form

$$w(B_{1,j}) = \int_{B_{1,i}}^{B_{1,i+1}} p(B_1) dB_1 = \frac{\sqrt{\ln\left(\frac{B_{1,\max}}{B_{1,i}}\right)} - \sqrt{\ln\left(\frac{B_{1,\max}}{B_{1,i+1}}\right)}}{\sqrt{\ln(d)}}. \quad (4.2)$$

This result is in contradiction to the popular assumption of a Lorentzian or a Gaussian weight function. To visualize the importance of considering the correct B_1 distribution in a simulation, $M_z(t)$ for an isotropic $S = 1/2$ spin system that is irradiated on-resonant is calculated numerically first with $w(B_{1,j})$ according to Eq. (4.2) with $\omega_{1,\min}/2\pi = 7.5$ MHz and $\omega_{1,\max}/2\pi = 15$ MHz (Fig. 4.3a), and then compared to an analogous simulation with the Lorentzian weight function

$$w_l(B_{1,j}) = \frac{1}{1 + \left(\frac{B_{1,j} - B_{1,\max}}{\Delta B_l}\right)^2}, \quad (4.3)$$

where ΔB_l is the half width at half height (hwhh) of this distribution (Fig. 4.3b). A value of $\Delta\omega_l/2\pi = g\beta_e\Delta B_l/h = 1.2$ MHz is used. B_1 is substituted in Fig. 4.3 by the corresponding ω_1 value, which is more common as a measure in numerical simulations. This is possible easily because only dimensionless relative values of B_1 appear in all the relevant formulae. A more detailed explanation is given in Appendix B. Since relaxation is neglected, the full dephasing of magnetization can be traced back to the B_1 distribution. With a sharp value of B_1 , the result would be an undamped cosine function.

It can be concluded that if the distribution of B_1 is considered in a simulation, it is important to use the weight function that corresponds to a certain type of resonator. By using a standard distribution, large errors compared to the experiment may occur.

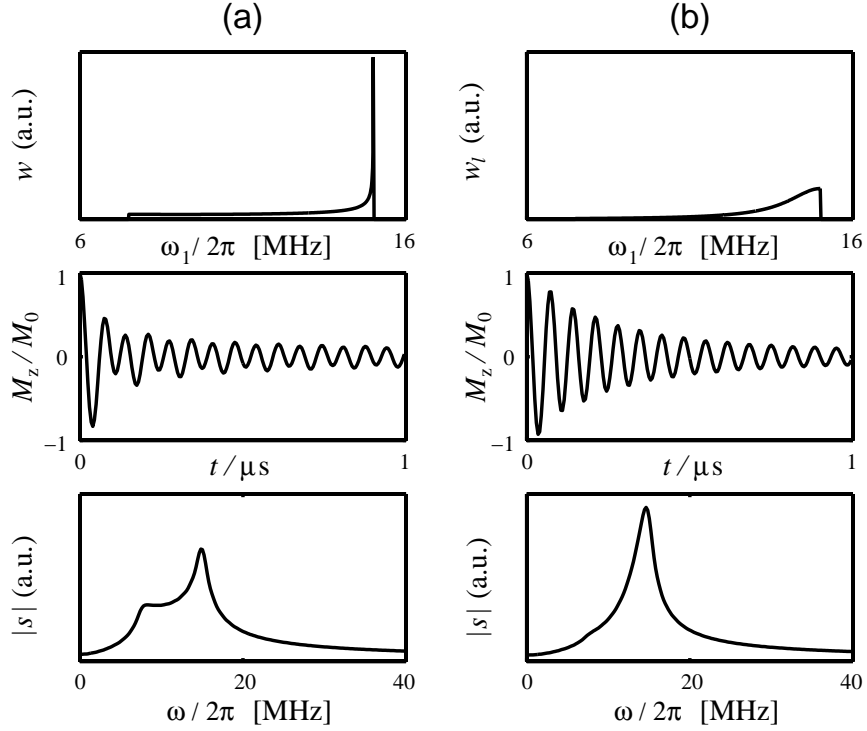


Figure 4.3: Influence of the mw field distribution in a simulation of an isotropic $S = 1/2$ spin system that is irradiated on-resonant. Relaxation is neglected. (a) Simulation with different $\mathcal{H}(B_{1,j})$ weighted with Eq. (4.2) corresponding to the measured B_1 distribution. (b) Simulation with a Lorentzian shaped weight function, given by Eq. (4.3). (top) Normalized weight function. (middle) Transient of $M_z(t)$ with $M_z(0) = M_0$. (bottom) Absolute value spectrum of the above transients. Both time traces were zero-filled to a length of $5 \mu\text{s}$ and apodized with an exponential decay.

4.4.2 Deriving an Analytical Expression for the Spin Nutation

If the simplest possible case is assumed with an $S = 1/2$ spin system that is irradiated on-resonant and relaxation is neglected, the longitudinal magnetization is modulated sinusoidally with the nutation frequency ω_1 , *i.e.* $M_z(t) = M_0 \cos(\omega_1 t)$. For this simple system, an analytic expression for $M_z(t)$ can be obtained also in the case of an inhomogeneous B_1 field if a parabolic instead of a Gaussian distribution of $B_1(h)$ is considered, namely

$$B_1(h) = B_{1,\text{max}} \left(1 - \frac{h^2}{k_p^2} \right). \quad (4.4)$$

k_p is a constant for a particular resonator. For our dielectric ring resonator, we obtain $k_p = 8$ mm. With this distribution, at least the values of B_1 inside the resonator can be fitted quite well.

The unnormalized probability $\tilde{p}_p(B_1)$ is

$$\tilde{p}_p(B_1) = -\frac{k}{2\sqrt{B_{1,\max}}(B_{1,\max} - B_1)}. \quad (4.5)$$

Normalization yields

$$p_p(B_1) = \frac{1}{2\sqrt{1-d^{-1}}\sqrt{B_{1,\max}}(B_{1,\max} - B_1)}. \quad (4.6)$$

In the simple system considered here, B_1 can be replaced by ω_1 in Eq. (4.6), because $\omega_{\text{eff}} = \omega_1 = g\beta_e B_1/\hbar$, and the constant correction factor between the two unit systems is incorporated into the integration limits. The transient of the longitudinal spin magnetization during on-resonant mw irradiation with field B_1 is now calculated as

$$\begin{aligned} \frac{M_z(t)}{M_0} &= \int_{\omega_{1,\max}/d}^{\omega_{1,\max}} p_p(\omega_1) \cos(\omega_1 t) d\omega_1 = \\ &= \sqrt{\frac{\pi}{2t\omega_{1,\max}}} \left[\cos(\omega_{1,\max} t) \text{C} \left(\sqrt{\frac{2\omega_{1,\max} t(1-d^{-1})}{\pi}} \right) \right. \\ &\quad \left. + \sin(\omega_{1,\max} t) \text{S} \left(\sqrt{\frac{2\omega_{1,\max} t(1-d^{-1})}{\pi}} \right) \right], \end{aligned} \quad (4.7)$$

with the Fresnel integrals [77]

$$\text{C}(x) = \text{FresnelC}(x) = \int_0^x \cos\left(\frac{\pi t^2}{2}\right) dt \quad (4.8)$$

$$\text{S}(x) = \text{FresnelS}(x) = \int_0^x \sin\left(\frac{\pi t^2}{2}\right) dt. \quad (4.9)$$

4.5 Sensitivity

4.5.1 Signal-to-Noise Ratio

The sensitivity of detection systems used in magnetic resonance has been discussed in detail by different authors. One of the most cited monographs about this topic is from POOLE [16], a more general one with its focus on the sensitivity of liquid state pulse NMR experiments is from ABRAGAM [20], which has been reexamined by HOULT and RICHARDS [78]. The approach by ABRAGAM is closer to the case of LOD because, at least with our setup, detection is done in the rf range at approximately 10 MHz, and a saddle coil similar to the one used in NMR experiments is used. The main difference is that we are not detecting a magnetization vector precessing in the xy plane with the Larmor frequency, but M_z changing in time. Nonetheless we will follow this approach to determine the signal-to-noise ratio ψ of our detector. The full calculation of ψ_{cw} assuming a continuous on-resonant excitation with a modulated amplitude, described by $\tilde{B}_1(t) = 0.5(1 + \cos(\omega_{\Xi}t))B_1$, is done in Appendix C. The result obtained for $T_1 < \omega_{\Xi}^{-1}$ and B_1 far below saturation is

$$\begin{aligned}\psi_{cw} &= \sqrt{\frac{\mu_0 V_C Q_{\Xi} \omega_{\Xi}}{64kT \Delta\nu F}} \eta_C a_0 M_0 \\ &= \frac{\sqrt{\mu_0} \beta_e \hbar}{24k^{3/2}} \frac{Ng \omega_{mw} a_0 S(S+1)}{T_S} \sqrt{\frac{Q_{\Xi} \omega_{\Xi}}{T \Delta\nu V_C F}},\end{aligned}\quad (4.10)$$

where a_0 is the saturation factor at the maximum mw field B_1 , η_C is the filling factor of the detection coil, V_C is the coil volume, V_S is the sample volume, $\Delta\nu$ is the bandwidth of the detector in Hz, T_S and T are the temperature of the sample and the detector, respectively, and F is the total noise figure of the amplifiers, including the voltage follower for impedance transformation.

Sometimes ψ_{cw} is specified as a function of the mw power absorbed by the spin system, given as [20]

$$P = \frac{\omega_{mw} \tilde{\omega}_1 \tilde{B}_1 T_2 M_0}{\mu_0 (1 + (\Omega_S T_2)^2 + \omega_1^2 T_1 T_2)} = \frac{\tilde{\omega}_1^2 B_0 T_2 M_0}{\mu_0 (1 + (\Omega_S T_2)^2 + \omega_1^2 T_1 T_2)}.\quad (4.11)$$

On-resonant and with the assumption that $a_0 \ll 1$, the power P_0 absorbed at the maximum mw field B_1 can be written as

$$P_0 = \frac{a_0 B_0 M_0}{\mu_0 T_1}. \quad (4.12)$$

Inserted into Eq. (4.10), we obtain

$$\psi_{cw} = \sqrt{\frac{\mu_0^3 V_C Q_\Xi \omega_\Xi}{64 k T \Delta \nu F} \frac{\eta_C T_1 P_0}{B_0}} = \frac{\mu_0^{3/2} \beta_e g \eta_C T_1 P_0}{8 \sqrt{k} \hbar \omega_{mw}} \sqrt{\frac{V_C Q_\Xi \omega_\Xi}{T \Delta \nu F}}. \quad (4.13)$$

In the limit of fast relaxation with continuous excitation, this is the behaviour of a “pseudo” square-law detector [16]. The detector itself is of course linear in the sense that the signal is proportional to the Fourier component of $dM_z(t)/dt$ at ω_Ξ , which itself is linear with respect to a_0 . But because a_0 is proportional to ω_1^2 , the signal is proportional to P_0 of the *exciting* field.

4.5.2 Number of Spins

From Eq. (4.10) it is possible to derivate a general formula for the number of spins in a sample. But because it is rather difficult to determine a_0 , this calculation can mainly be used to estimate the minimum number of detectable spins N_{\min} by setting $\psi = 1$. We then get

$$N_{\min} = \frac{24k^{3/2}}{\sqrt{\mu_0} \beta_e \hbar} \frac{T_S}{g \omega_{mw} a_0 S(S+1)} \sqrt{\frac{T \Delta \nu V_C F}{Q_\Xi \omega_\Xi}}. \quad (4.14)$$

N_{\min} can now be obtained by assuming realistic values for the instrumental parameters. In a room temperature experiment (300 K) at X-band (10 GHz) with an $S = 1/2$ sample with $g = 2$, a detection frequency $\omega_\Xi = 2\pi \cdot 10$ MHz, a quality factor $Q_\Xi = 100$, a coil volume $V_C = 0.5 \text{ cm}^3 = 5 \cdot 10^{-7} \text{ m}^3$, a saturation factor $a_0 = 0.2$, $\Delta \nu = 1 \text{ s}^{-1}$ and assuming $F = 1$, we get $N_{\min} \approx 3 \cdot 10^{12}$ spins. This is on the same order of magnitude of what can be expected from a conventionally detected cw EPR experiment. For example, a typical value at room temperature of $N_{\min} \approx 5 \cdot 10^{12}$ spins is given in [79] with similar instrumental parameters.

4.5.3 Comparison Between Pulse and CW LOD Experiments

While the instrumental part is identical to cw LOD EPR, the main problem to give a general formula for the sensitivity of pulse LOD experiments is the existence of different excitation schemes. Hence only the theoretical optimum is considered here. If we assume a nutation pulse of length t_p that modulates $M_z(t)$ cosinusoidally with ω_{Ξ} , *i.e.* $M_z(t) = M_0 \cos(\omega_{\Xi}t)$, whose realization is discussed in chapter 6, we get during the excitation

$$-\frac{dM_z(t)}{dt} = M_0\omega_{\Xi} \sin(\omega_{\Xi}t) \quad (4.15)$$

if $T_2 \gg t_p$. This is the pulse analogue to Eq. (C.7) for cw LOD EPR. The maximum shot repetition time t_s is given by the duty cycle ρ of the high-power mw amplifier as

$$t_s = \frac{t_p}{\rho}. \quad (4.16)$$

If $T_1 \ll t_s$, the spin magnetization can fully recover between the different pulses. Because at X-band a TWT amplifier has typically $\rho = 0.01$, it is in principle possible to fulfill both requirements, $T_2 \gg t_p$ and $T_1 \ll t_s$. Additionally, a homogeneous B_1 field and an isotropic g are required that Eq. (4.15) is valid.

It is known from signal theory that the S/N is proportional to \sqrt{n} , where n is the number of identical experiments that are accumulated. Thus we obtain

$$\psi_p = \sqrt{\frac{\mu_0 n V_C Q_{\Xi} \omega_{\Xi}}{4kT \Delta\nu_p F}} \eta_C M_0. \quad (4.17)$$

It is important to consider that the minimum bandwidth $\Delta\nu_p$ in the pulse experiment is dependent on the pulse length and Q_{Ξ} . The longer the signal persists, the lower is $\Delta\nu_p$ that can be achieved. For a short pulse, its minimum is given by $\Delta\nu_p = \omega_{\Xi}/2\pi Q_{\Xi}$, and for a long pulse, it approaches [15]

$$\Delta\nu_p = 1/t_p. \quad (4.18)$$

Typically, a TWT amplifier can produce pulses up to 10 μs in length. If we adjust $\Delta\nu$ in a cw LOD experiment to a value that the recording time corresponds to one

shot in the pulse experiment, *i.e.*

$$\Delta\nu = 1/t_s, \quad (4.19)$$

we can compare ψ_{cw} and ψ_p by calculating the ratio

$$\frac{\psi_{cw}}{\psi_p} = \frac{a_0}{4\sqrt{\rho}} \quad (4.20)$$

if we assume Eq. (4.18) to be appropriate. This pretends cw LOD EPR to be less sensitive than pulse LOD EPR. But the quality of the assumptions concerning the determination of $M_z(t)$ in the two cases is completely different. While the sensitivity of the pulse LOD experiment was calculated with strongly idealized specifications, the S/N calculation for the cw LOD experiment was more realistic, provided that the requirements for the relaxation times are fulfilled.

By comparing Eq. (4.10) and Eq. (4.17), it becomes obvious that pulse LOD is favourable for long T_2 not only because of its higher flexibility, but also for sensitivity reasons, while cw LOD is well suited for short relaxation times. As soon as the assumption $T_1 < \omega_{\Xi}^{-1}$ breaks down, ψ_{cw} becomes much worse than in Eq. (4.10). Eq. (4.17) holds relatively well for longer relaxation times, but becomes wrong for short relaxation times.

Chapter 5

Measuring Polarization With Pulse LOD

Longitudinal detection is especially well suited to measure spin polarization because it is sensitive to $dM_z(t)/dt$, and therefore it is not necessary to transfer polarization to coherence to be measured. Different procedures for this task are described in this chapter, taking advantage of the properties and special features of the setup with respect to both sensitivity and flexibility.

5.1 Building Blocks for the Detection of Polarization

A pulse EPR experiment can be subdivided into different building blocks. Usually these are preparation, evolution, mixing, and detection periods [80]. Commonly used detection building blocks, or detectors, create either an FID or an echo. Detector sequences to measure spin polarization are now presented and analyzed for an LOD setup. The signals calculated for the different cases are plotted with the same scaling in all figures to be easily comparable.

5.1.1 Short MW Pulse

The simplest possibility is to apply a short, strong mw pulse of length t_p . This flips the spins with a Larmor frequency within the excitation bandwidth of the pulse by an angle $\beta = \omega_{\text{eff}} t_p$, with ω_{eff} given by Eq. (2.24). This situation is shown in Fig. 5.1. It is evident that with this simple excitation scheme, the dependence of the signal intensity on the relaxation times is small as long as $T_2 > 2\pi/\omega_{\Xi}$.

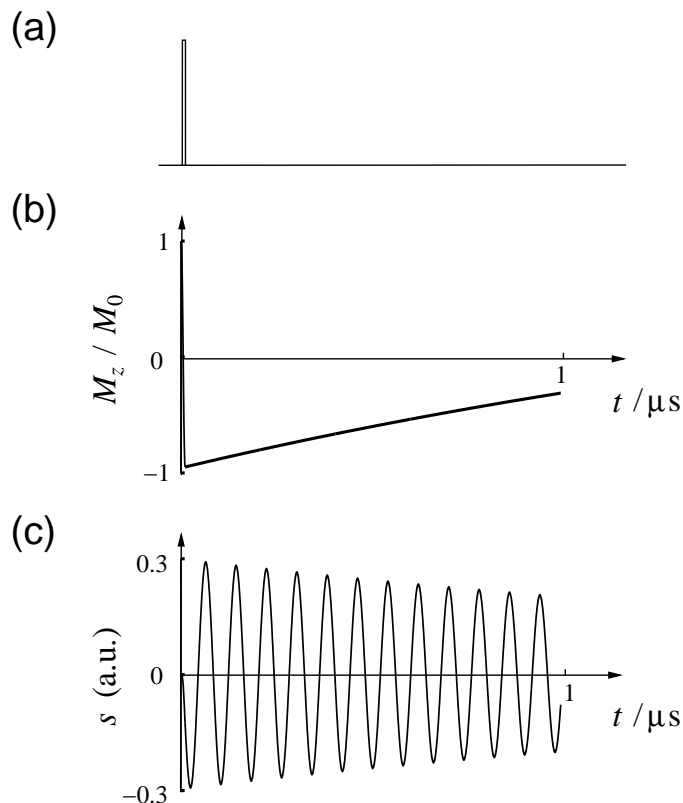


Figure 5.1: Effect of a 10 ns mw pulse (a) with $\omega_1/2\pi = 50$ MHz on the time evolution of M_z of an isotropic $S = 1/2$ spin system that is irradiated on-resonant (b) and the response of the longitudinal detection circuit (c). Relaxation times are $T_1 = 2.5 \mu\text{s}$ and $T_2 = 100$ ns. The resonance frequency of the detection circuit is $\omega_\Xi/2\pi = 12.5$ MHz, and its quality factor is $Q_\Xi = 100$.

In certain cases it is important to consider that the relaxing magnetization induces an additional signal after the mw excitation is switched off. This effect can be neglected for $T_1 \gg 2\pi/\omega_\Xi$, but it becomes more pronounced the shorter T_1 is, and it is especially important if T_1 is on the order of $2\pi/\omega_\Xi$ or shorter. This additional signal component is not dependent on $M_z(0)$, but on $M_z(t_p)$ at the end of the mw pulse. This effect can be avoided if only data points during the pulse are analyzed. Thus the length of the pulse must be large enough that a reasonable signal can be measured, which is usually the case if the pulse length is at least half a modulation period of the detector, *i.e.* $t_p \geq \pi/\omega_\Xi$.

5.1.2 Nutation Pulse

To apply a short mw pulse to measure M_z is most effective for short relaxation times where the experiment can be repeated with a high rate and a large number of summations for each data point is possible without increasing the measuring time too much. For a sample with T_1 on the order of 10^{-3} s or larger, this is not possible anymore, and a detector sequence is needed that induces a larger signal to compensate for the lower repetition rate. Generally speaking, this criterion is met if the spectral component of $dM_z(t)/dt$ at ω_{Ξ} is enlarged. This can be achieved with a long nutation pulse whose amplitude is adjusted such that

$$\omega_{\text{eff}} = \omega_{\Xi}, \quad (5.1)$$

i.e. if the nutation frequency is equal to the resonant frequency of the detection circuit. Alternatively, a setup could be constructed that allows the variation of ω_{Ξ} in a large frequency range, but this is not the scope of this work. The more nutation periods are present to induce the signal, the larger the signal becomes. To discuss the effect of such a high-turning angle (HTA) pulse, two situations depending on T_2 of the sample must be distinguished. They are illustrated in Fig. 5.2.

$T_2\omega_{\text{eff}} > 1/2$: The nutation of magnetization is damped undercritically, and the induced signal is amplified with every additional nutation period (Fig. 5.2a). Setting $\omega_{\text{eff}} = \omega_{\Xi}$ gives the maximum signal, as can be seen in Fig. 5.3a.

$T_2\omega_{\text{eff}} < 1/2$: The nutation of magnetization is overdamped by the fast transverse relaxation, thus no oscillation of $M_z(t)$ is observed, and $dM_z(t)/dt$ has only a weak Fourier component at ω_{Ξ} , leading to a much weaker signal (Fig. 5.2b). The signal intensity increases with higher mw power (Fig. 5.3b). On the other hand, despite the relatively high Q_{Ξ} a broadband signal is induced by $M_z(t)$ that approaches its steady-state value during the pulse, which is clearly visible in Fig. 5.2b (bottom). If T_1 is also short, *i.e.* on the order of $2\pi/\omega_{\Xi}$ or shorter, two additional effects gain considerably in importance. The first one is the broadband signal that is induced by the return of $M_z(t)$ to Boltzmann equilibrium after switching off the mw field. In contrast to the signal induced by the decaying magnetization when the mw field is switched on, this signal only depends on T_1 . An application of this observation is presented in chapter 7. The second effect is the modulation

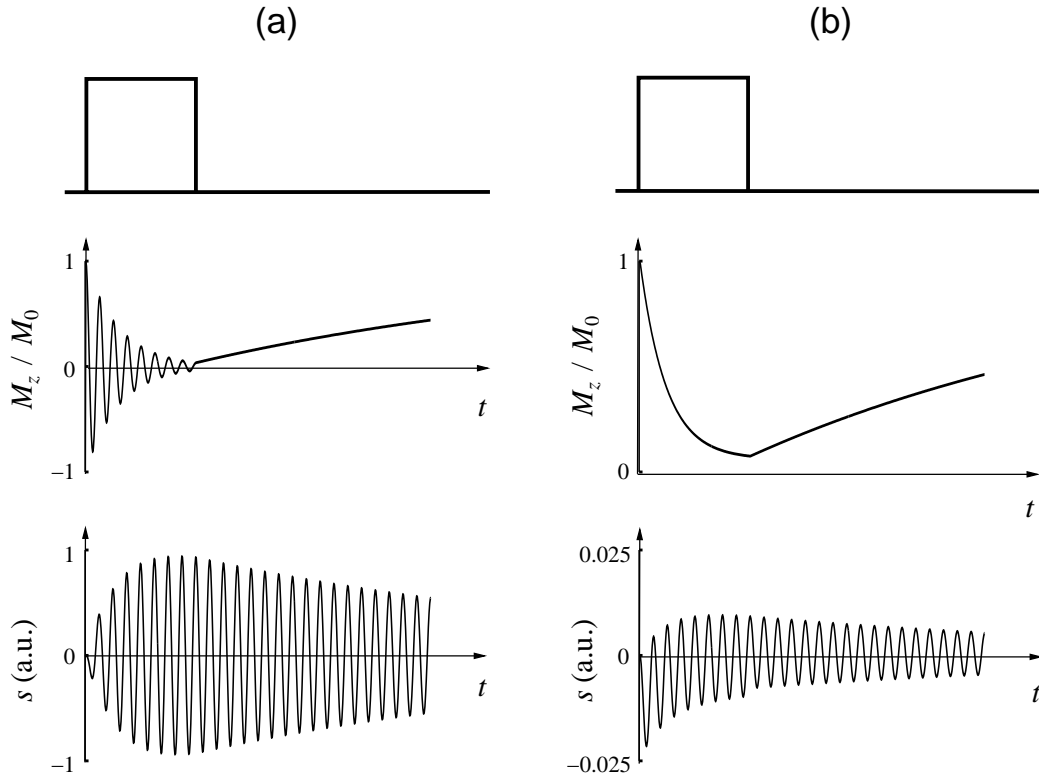


Figure 5.2: Effect of an mw pulse (*top*) with amplitude $\omega_1 = \omega_{\Xi}$ on the time evolution of M_z of a homogeneous $S = 1/2$ spin system that is irradiated on-resonant (*middle*) and the response of the LOD circuit (*bottom*). $T_1 = 30 \times 2\pi/\omega_{\Xi}$ in both cases, and $Q_{\Xi} = 100$. (a) $T_2 = T_1/25 > 2\pi/\omega_{\Xi}$. (b) $T_2 = T_1/2500 \ll 2\pi/\omega_{\Xi}$.

induced by the return of M_z to M_0 , which is determined by the Fourier component of $dM_z(t)/dt$ at ω_{Ξ} . If M_z approaches its respective equilibrium value quickly, we can say roughly that if the duration of the mw pulse is a half-integer multiple of the period of the resonant circuit, the signal induced by switching on the pulse and the one induced by switching the pulse off are added. If the length is an integer multiple, the signals are subtracted. The phase between the two signals depends on T_1 , T_2 and ω_{eff} .

5.1.3 Refocused Nutation Pulse

The decay of the transient nutation caused by B_1 -field inhomogeneities and by an inhomogeneous broadening of the EPR line that is much larger than ω_1 can be refocused to a rotary echo [15,25] by changing the phase of the mw field during the

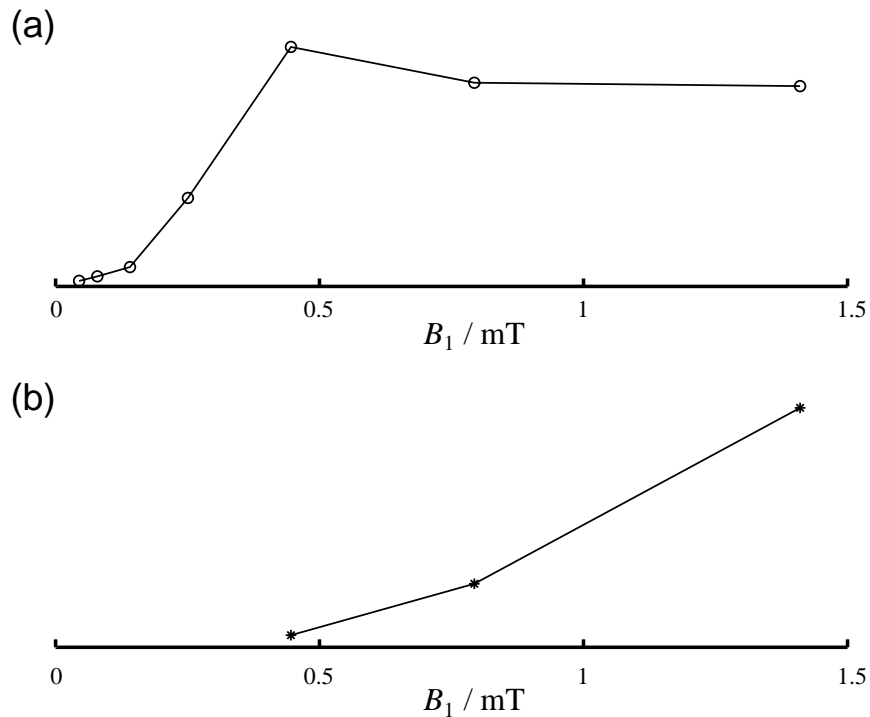


Figure 5.3: Signal intensity of a nutation pulse polarization detector as a function of the mw field amplitude. The length of the nutation pulse is equal to two modulation periods of the detection circuit. The signal transient is recorded during the pulse. The measured points are connected for visibility. (a) Signal of a coal radical with $T_2\omega_{\text{eff}} \gg 1/2$. (b) Signal of an iron complex with $T_2\omega_{\text{eff}} \ll 1/2$.

pulse by 180° . This procedure can be repeated several times, resulting in the pulse sequence shown in Fig. 5.4a, with a first nutation pulse of length t_p , followed by a succession of refocusing pulses with alternating phases and length $2t_p$. Since for detection the phase of the oscillating magnetization must remain the same during the whole pulse sequence, t_p has to be set to

$$t_p = \frac{n 2\pi}{2 \omega_{\Xi}} \quad , \quad n = 1, 2, \dots \quad (5.2)$$

Fig. 5.4bc show the evolution of M_z for the scheme with refocused magnetization if T_1 and T_2 are chosen much larger than ω_{eff}^{-1} . The influence of an inhomogeneous B_1 field and an inhomogeneous EPR line is shown in Fig. 5.4b and 5.4c, respectively. In the case of an inhomogeneous B_1 field, it was necessary to set $\omega_{1,\text{max}} > \omega_{\Xi}$ in order to get a smooth transition of $M_z(t)$ at the time the phase of the pulse is switched. This is because the resulting function in case of an $S = 1/2$

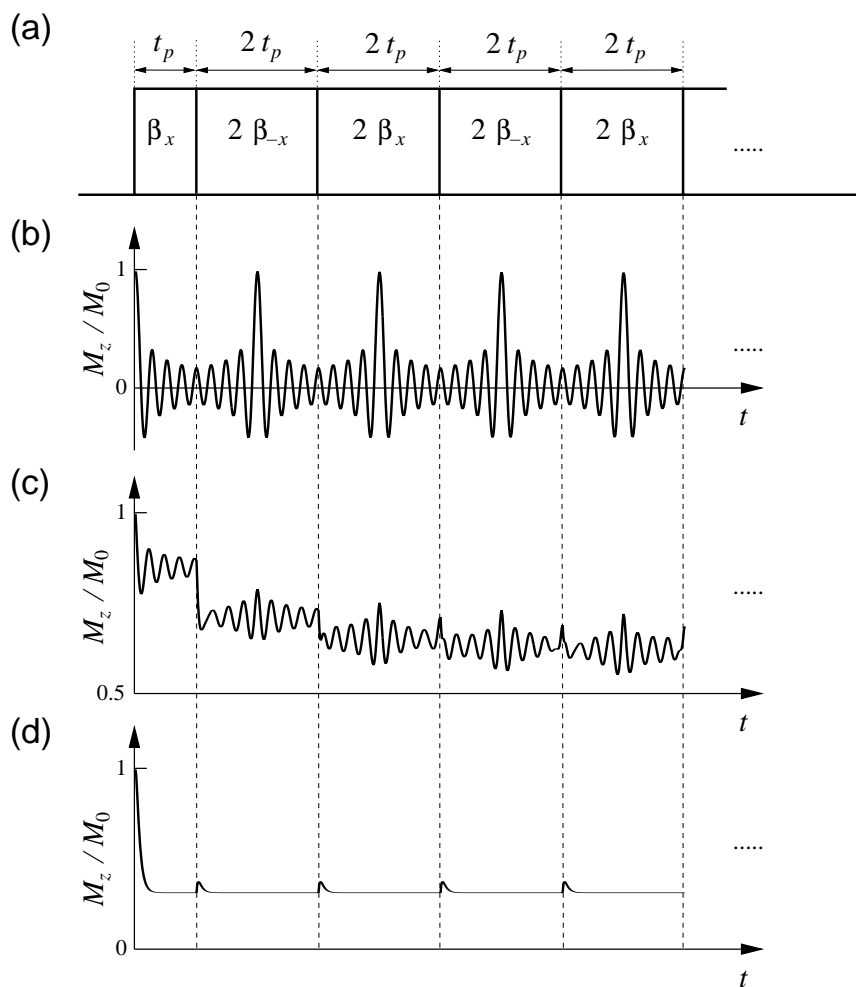


Figure 5.4: (a) Pulse subdivided into segments with alternating phase to generate a train of rotary echoes. (b) Time evolution of M_z for a spin system with a homogeneous EPR line that is irradiated on-resonant with an inhomogeneous B_1 field. (c) Time evolution of M_z for an inhomogeneous EPR line in a homogeneous B_1 field. (d) Time evolution of M_z of a homogeneous EPR line in a homogeneous B_1 field with $T_1 = 2\pi/\omega_1$ and $T_2\omega_1 = 0.4$.

system is not just an exponentially damped oscillation with constant phase, but – as is shown in §4.4.2 – it can be approximated by a superposition of a sinus and a cosinus function weighted with their respective Fresnel integral (Eq. 4.7). This has consequences in practical applications. It is relatively difficult to tune the B_1 field to its optimum value because the B_1 field that gives a maximum signal during the first pulse segment is not equal to B_1 with a smooth transition at the mw phase switch position, which has an overall maximum spectral component at ω_{Ξ} . Because for the experiments the B_1 adjustment was done manually by changing the

attenuation until the signal observed on the oscilloscope was maximum, a change of the shape of the signal could be observed, but it was very difficult to determine the position with maximum signal at ω_{Ξ} without Fourier transforming it. If an experiment without refocusing of magnetization is used to tune B_1 , which provides an unambiguous result, the progression of M_z at the phase switching position is not smooth. The smooth transitions are then obtained at a field position farther off-resonant. A practical example where this problem occurs is shown in chapter 6.

In the case of an inhomogeneous B_1 field, the magnetization can be entirely refocused with this procedure. The same is not possible for an inhomogeneously broadened EPR line. For off-resonant contributions, the angle θ between \mathbf{B}_0 and \mathbf{B}_{eff} changes its sign. For a complete refocusing of magnetization, it would be required that θ is changed by 180° . This is also the reason for the “jumps” of M_z at the position of the phase change of the mw field in Fig. 5.4c.

If $T_2\omega_1 < 1/2$, the spin system behaves completely different to such an excitation. As we have seen in the last section, the nutation is overdamped and M_z approaches a steady-state during the mw pulse. In this case, the magnetization cannot be refocused, and the spin system behaves as in a cw LOD experiment with phase modulation of the mw field, which is shown in Fig. 5.4d. This mechanism might also influence the result if $T_2\omega_1$ is not orders of magnitude larger than 0.5, and $T_1 \approx T_2$. In this case, this second mechanism becomes more important the more refocusing segments a nutation pulse has and the longer the whole pulse is.

5.1.4 B_1 Cycle

In time-domain pulse EPR experiments, magnetization is manipulated with at least one mw pulse previous to detection, which induces a signal in an LOD circuit as well. Depending on the exact state of the circuit at the time the detection pulse is applied, an enlargement or an annihilation of this already present signal is observed, according to the phase difference between the modulation induced by the preparation and the detection sequence. Because this phase difference is generally not constant in a time-domain experiment where pulses are shifted with respect to each other, the final signal is additionally modulated with ω_{Ξ} . Because an LCR

resonant circuit is a linear device, the additional modulation in the signal can be removed easily with a B_1 cycle, *i.e.* by subtracting the signal obtained in an experiment without detection pulse (*blind signal*). The principle is illustrated in Fig. 5.5. To get optimum results, two different mw channels should be used for the

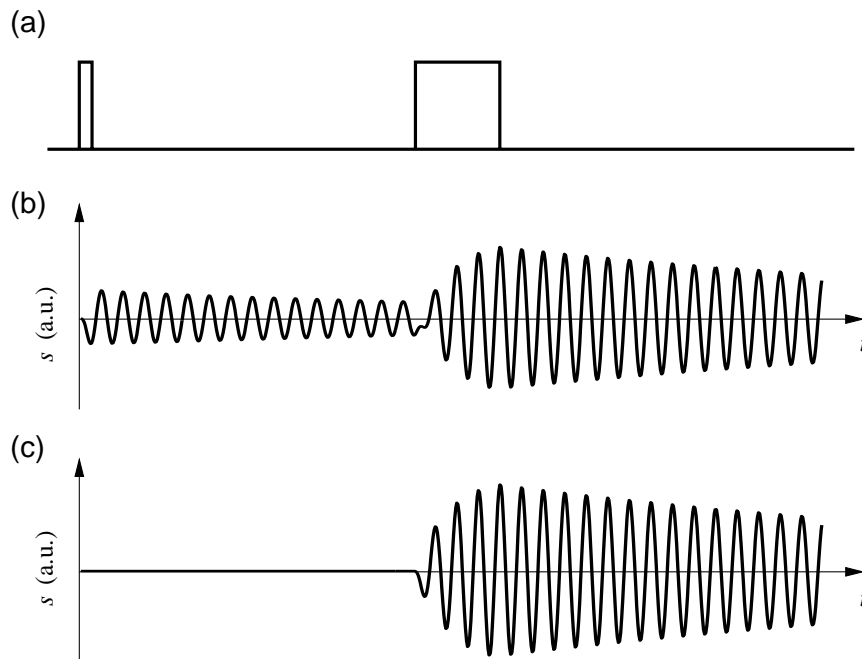


Figure 5.5: Simulation of the effect of a B_1 cycle in an LOD experiment with an LCR circuit with $Q_{\Xi} = 100$. First an inversion pulse is applied, and after an evolution time, M_z is read out with a nutation pulse. (a) Position of the two mw pulses. (b) Signal on the detection circuit if both mw pulses are applied. (c) Resulting signal if a blind signal without detection pulse is subtracted from the transient in (b).

preparation and the detection pulse. The blind signal is obtained with a fully attenuated detection pulse; all other parameters remain the same. With this procedure not only the signal induced by the first pulse is subtracted, but also spikes induced by other mw devices like the switches or the TWT amplifier are eliminated. The success of this method in practical applications is demonstrated in chapter 7 along with other methods specifically designed for relaxation time measurements.

5.2 Signal Recording and Data Processing

Because the highest frequency components of the signal with our LOD setup are about 100 MHz, it is possible to record the signal transiently, without demodulating it first like it is necessary with transverse detection. On the other hand, pulse EPR spectrometers are usually designed to use a boxcar integrator for data acquisition, and the transient data recording is an option that usually lacks some features. It is shown how both methods can be used in LOD, and the respective advantages and drawbacks are listed.

5.2.1 Collecting Data with a Transient Recorder

In an LOD experiment, the frequency of the signal of interest is often on the same order of magnitude as ω_{Ξ} . The most flexible method for data processing is thus to record the full transient signal with a transient recorder and subsequently analyze the data and reduce it to the desired information. Sometimes it is even possible to cross-check the result with a different analysis method. An example for that is presented in chapter 7. Furthermore, systematic errors can often be avoided or at least identified after the measurement.

A drawback of this method is that the data sets are several orders of magnitude larger than when only one point per shot is recorded. To avoid an excessive increase of data, the sampling rate of the transient recorder should not be chosen larger than needed for the frequencies of interest. To avoid backfolding of noise, a lowpass filter can be used before the data is digitized. As an alternative that might be interesting as a further development, especially with respect to the use of LOD in routine applications, one can think of recording the signal transiently, but performing an automatized analysis during the measurement so that only the reduced data accumulates, equivalent to the use of a much simpler recording setup like a boxcar integrator. Another drawback of a transient recorder is that the spectrometer software is not capable to record more than two-dimensional data sets. If the transient dimension is reduced to one point, it is effectively only possible to perform one-dimensional experiments. Furthermore, with some transient recorders no phase or B_1 cycles can be applied directly, so that it becomes necessary to record

the respective traces separately and add them up manually.

5.2.2 Analysis of Transient Data

The obvious method to analyze transient data is to use a Fourier transform and pick out the frequency components of interest. To avoid side effects and to determine the frequencies precisely enough, a zero filling of the measured data might be necessary.

If only the spectral component at ω_{Ξ} of the signal is considered, it is easier to use the same mathematic scheme that is used in a lock-in amplifier, because it is usually simpler to evaluate the DC component of a signal than the value at a certain frequency. In this scheme the signal $V_S \sin(\omega_{\Xi}t + \varphi_S)$ is multiplied with a reference $V_R \sin(\omega_{\Xi}t + \varphi_R)$, and the output

$$\begin{aligned} V_M &= V_S V_R \sin(\omega_{\Xi}t + \varphi_S) \sin(\omega_{\Xi}t + \varphi_R) \\ &= \frac{1}{2} V_S V_R (\cos(\varphi_R - \varphi_S) + \sin(2\omega_{\Xi}t + \varphi_R + \varphi_S)) \end{aligned} \quad (5.3)$$

is obtained. Since the signal of interest and the reference have the same frequency, the first term of the output is at DC. The second term is at frequency $2\omega_{\Xi}$ and can be readily removed after a Fourier transform of V_M . The phase of the signal can be obtained simply by performing the same calculation with the reference phase $\varphi_R - \pi/2$. The bandwidth of the signal depends on the length and the shape of the input transient as is the case with a conventional Fourier transform. Since a DC offset of the input signal leads to an output that is modulated with the reference frequency, it is not necessary to perform a baseline correction with this method.

If the measured transient has a good S/N , it might be convenient to sum up the absolute value of all data points after a baseline correction. This broadband method is not frequency selective like the Fourier methods, but this drawback might be small, especially if Q_{Ξ} is large. This leads directly to the data acquisition method discussed in the next section.

5.2.3 Collecting Data with a Boxcar Integrator

The simplest way to record a signal is to use a boxcar averager, where the signal is integrated during a certain time period. This method lacks the possibility to be frequency selective. If a modulated signal is recorded with such a device over a full period or an integer number of periods, it is cancelled out except for asymmetries. Since the signal across an LOD circuit is such a modulation, a boxcar integrator might not be the device of choice for most experiments. On the other hand, every pulse spectrometer is capable to process data from a boxcar integrator, and phase or B_1 cycles can be performed easily. In addition, it is possible to record truly multi-dimensional spectra because the data does not have to be reduced after recording. This also keeps the data set small.

There are two ways to use a boxcar integrator in an LOD experiment. The first one is to choose the boxcar window such that it spans not more than half a modulation period of the resonant circuit, which is sensible mainly in experiments with short pulses to read out spin polarization. The second approach is to rectify the modulation before it is recorded. In this case, the boxcar window can have an arbitrary length, but care must be taken that the signal has no offset.

5.2.4 Signal Processing with a Lock-In Amplifier

In an experiment with continuous excitation, it is not practicable to record data with a transient recorder. In this case it is much more convenient to perform a phase-sensitive detection with a lock-in amplifier where one spectral component of the signal, usually ω_{Ξ} , is read out selectively. With such a device a time averaging of the signal adjusted to the sweep rate and the line width can be performed, thus obtaining the optimum S/N , without the need to further process the data.

5.3 Time-Resolved Polarization Measurement

To measure the time dependence of the polarization represents the boundary of LOD. This is only a conceptual study with some preliminary results, thus no optimization of the equipment was implemented.

5.3.1 Procedure

Independent of the setup that is used, the properties of the detection circuit must be known accurately. It is not possible to build a detector that is sensitive and at the same time no resonances appear on a broad bandwidth from DC up to several tens of MHz. The differential equation that describes the circuit must be known along with the relevant parameters such as resonance frequency ω_{Ξ} and quality factor Q_{Ξ} . For this conceptual approach, Eq. (3.7) is used, but with a general excitation function $V_{\text{ind}}(t)$, *i.e.* the voltage induced in the coil by M_z changing in time given by Eq. (3.1). Then $V_{\text{ind}}(t)$ is numerically determined from the measured transient signal $V_{\Xi}(t)$ with

$$\frac{1}{\omega_{\Xi}^2} \frac{\Delta^2}{\Delta t^2} V_{\Xi}(t) + \frac{1}{Q_{\Xi} \omega_{\Xi}} \frac{\Delta}{\Delta t} V_{\Xi}(t) + V_{\Xi}(t) = V_{\text{ind}}(t), \quad (5.4)$$

where Δt is the time between the data points that are used to determine the derivatives of the transient $V_{\Xi}(t)$. Note that Δt is not necessarily equal to the time between two adjacent data points. To solve this equation for $V_{\text{ind}}(t)$, the second derivative of the measured signal with respect to t must be calculated from noisy data. This is known to be a problem because noise is amplified with every derivation of discrete data. If the sampling rate is higher than needed, noise is further increased if adjacent points are used to calculate a derivative. It is thus advantageous to either use non-neighbouring data points, or to calculate the slope using a suited interpolation between several data points. In this example, a weighted linear regression is used, where the slope is given as

$$\frac{\Delta V_{\Xi}(t)}{\Delta t} = \frac{\sum_{i=1}^N w_i (t_i - \langle t \rangle) V_{\Xi,i}}{\sum_{i=1}^N w_i (t_i - \langle t \rangle)^2}, \quad (5.5)$$

with the average value $\langle t \rangle$ of the time values and the weight factor

$$w_i = \cos \left(\pi \frac{t_i - t}{t_{\max} - t_{\min}} \right) \quad t_{\min} \leq t \leq t_{\max} \quad (5.6)$$

$$w_i = 0 \quad t < t_{\min}, t > t_{\max}.$$

w_i was chosen to weight data points less the farther away they are from time t at which the slope is to be determined. This “cosine bell” function covers data points that lie between t_{\min} and t_{\max} and are centered around t . These boundary points do not have to coincide with real data points. The second derivative is calculated in the same way from the points that are obtained after the first cycle. To avoid the introduction of artifacts at an early stage of the analysis, $t_{\max} - t_{\min}$ should not be larger than the inverse bandwidth of the voltage follower. Denoising algorithms where resolution is lost can be applied at a later stage, where it is easier to predict their consequences.

The problem of the increased noise caused by the second derivative of the signal is somewhat reduced because $V_{\text{ind}}(t)$ is according to Eq. (3.1) proportional to $dM_z(t)/dt$, thus to obtain $M_z(t)$ we can integrate the resulting transient, regaining some of the lost sensitivity.

Another problem could be that ω_{Ξ} and Q_{Ξ} are experimentally not determined precisely enough to obtain the desired result within the noise limit. This can be circumvented by optimizing these values during the data analysis. We know that after the end of the excitation, the spectral component of $V_{\text{ind}}(t)$ at ω_{Ξ} should not be higher than the surrounding frequencies, at least not for spectroscopic reasons. Thus the ringing of the detector after the excitation must be recorded for some time. This ringing can be analyzed with exactly the procedure described above, varying ω_{Ξ} and Q_{Ξ} . At the correct values, the Fourier transform of $V_{\text{ind}}(t)$ should show no peak at ω_{Ξ} . This refinement works well because the starting value of ω_{Ξ} is already known very accurately. This can be seen in Fig. 5.6, where the signal during the ringing of the detection circuit after an excitation was analyzed. Fig. 5.6a shows the spectral component at ω_{Ξ} of the reconstructed excitation V_{ind} when ω_{Ξ} is varied. It should not have an increased value compared with the frequency components slightly higher and lower than ω_{Ξ} because the only mechanism that contributes to V_{ind} from the spin system is its relaxation, which is not modulated. Fig. 5.6b shows the influence of Q_{Ξ} on the result. One can see that a small variation on ω_{Ξ} has a much larger effect than a small variation of Q_{Ξ} . This is obvious because the squared value of ω_{Ξ} goes into the equation of motion, while the value of Q_{Ξ} appears only linear.

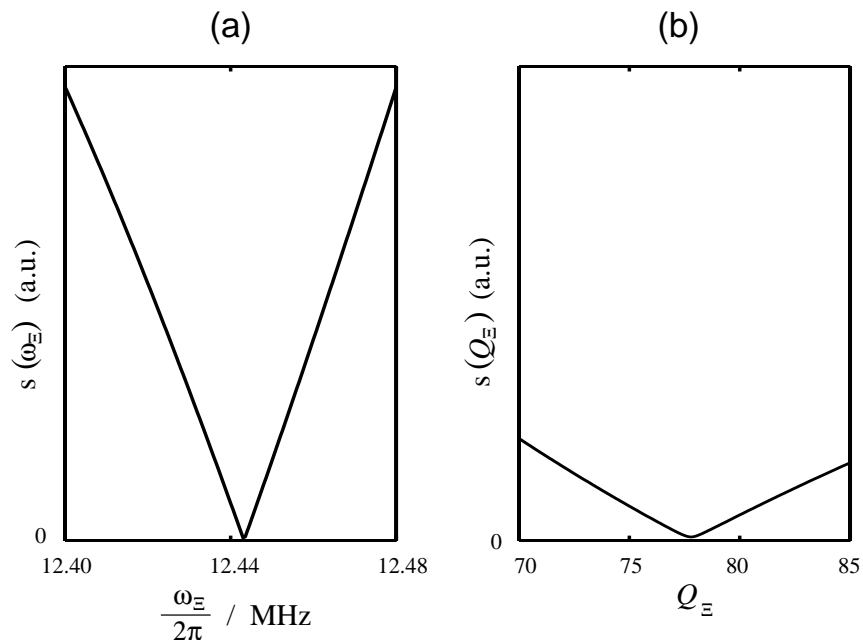


Figure 5.6: Exact numerical determination of ω_{Ξ} and Q_{Ξ} . The excitation V_{ind} is reconstructed from the ringing of the resonator with the equation of motion of the LCR circuit, and the spectral component of V_{ind} at ω_{Ξ} is minimized. (a) Variation of ω_{Ξ} with constant Q_{Ξ} . (b) Variation of Q_{Ξ} with constant ω_{Ξ} . The y axis is identically scaled as in (a).

One of the limiting factors of this method is the validity of Eq. (3.7) for the detection circuit. The use of real electronic components compared to the idealized ones in the theoretical descriptions leads to resonances at higher harmonics of ω_{Ξ} that do not appear in the formulae. These higher harmonics thus cannot be removed by a more precise determination of ω_{Ξ} and Q_{Ξ} .

5.3.2 Experimental Example

To demonstrate the feasibility and the limitations of this approach, a train of 31 high-power mw pulses of 40 ns length and 40 ns interpulse delay was applied to a sample of 1 % bis(picolinato)Cu(II), $\text{Cu}(\text{pic})_2$, diluted into the corresponding Zn complex. B_0 was chosen at the position with maximum signal, and the measurement was done at room temperature. The distance between the sampling points was 1 ns, and w_i was calculated with $t_{\text{max}} - t_{\text{min}} = 10$ ns. The resonant frequency of the detector was set to $\omega_{\Xi}/2\pi = 12.5$ MHz by adjusting the tunable capacitor

C_T such that the signal is maximum. This is possible because the repetition rate of the pulses in the pulse train was 12.5 MHz, thus a dominant spectral component at this frequency was created. The quality factor of the detection circuit was approximately $Q_{\Xi} = 75$, determined before the fine adjustment of C_T . With the refinement procedure described above, the exact values, $\omega_{\Xi}/2\pi = 12.443$ MHz and $Q_{\Xi} = 77.8$, were obtained. The time trace $V_{\Xi}(t)$ of the original signal is shown in Fig. 5.7a together with the reconstructed voltage $V_{\text{ind}}(t)$ in Fig. 5.7b. The corresponding Fourier transforms are displayed in Fig. 5.7d-g. We see that

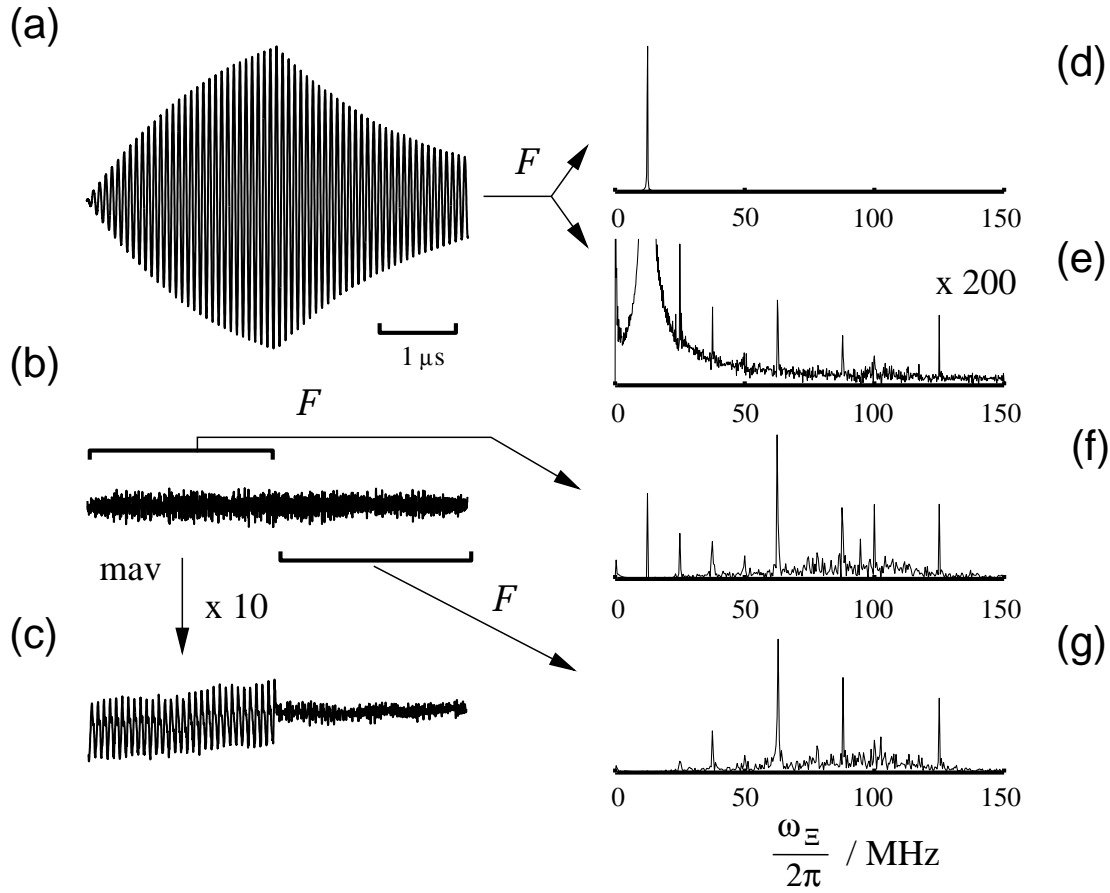


Figure 5.7: Reconstruction of the time trace of $M_z(t)$ during and after a pulse train with 31 pulses from the transient signal measured on the resonant circuit. (a) Original trace of $V_{\Xi}(t)$ as measured with the transient recorder. (b) Time trace of the reconstructed $V_{\text{ind}}(t)$. (c) $V_{\text{ind}}(t)$ after denoising with two consecutive moving averages over 16 ns. (d) Absolute value of the Fourier transform of $V_{\Xi}(t)$. (e) Same as (d), but scaled with a factor 200. (f) Absolute value of the Fourier transform of $V_{\text{ind}}(t)$ during the pulse train. (g) Absolute value of the Fourier transform of $V_{\text{ind}}(t)$ after the pulse train.

the dominant component in the spectrum of $V_{\Xi}(t)$ is at ω_{Ξ} . In the spectrum of $V_{\text{ind}}(t)$, this component is prominent only during the pulse train, while it is not visible anymore afterwards. Above 100 MHz, which is approximately the bandwidth of the voltage follower, the noise in the frequency spectrum decreases to zero.

To observe the impact of the pulses in the time trace of $V_{\text{ind}}(t)$, a strong denoising procedure is necessary. The trace in Fig. 5.7c was obtained with two consecutive moving averages (mav) over 16 ns, thus reducing the bandwidth considerably. This is not necessary to observe the strong component at the repetition frequency of the pulses in the Fourier spectrum of $V_{\text{ind}}(t)$ during the pulse train (Fig. 5.7f). The same component vanishes in Fig. 5.7g, which shows the spectrum of $V_{\text{ind}}(t)$ after the pulse train. This spectrum was used to optimize ω_{Ξ} and Q_{Ξ} .

In the frequency spectra on the right hand side of Fig. 5.7, the limitations of the method become evident in the way that most peaks appear at higher harmonics of ω_{Ξ} . To identify their origin, one needs to distinguish between peaks that are only present during the pulse train and thus really caused by $M_z(t)$, and peaks with instrumental origin that are always present. The instrumentally induced signals can be subdivided into B_1 -field dependent and B_1 -field independent ones. To distinguish between them, two independent measurements with different mw power are needed. The only B_1 -field independent signal in Fig. 5.7fg is the one at 125 MHz, which had the same intensity in all measurements. There is another one at 250 MHz, which is not shown. Such signals, which are often caused by a clock in one of the spectrometer components that is not sufficiently shielded or by a grounding path, are typically very narrow and have a frequency that is characteristic for a clock like 10 MHz or 25 MHz (or an integer multiple of it).

The time trace in Fig. 5.7 can now be integrated to obtain $M_z(t)$. The same problem that is well-known for the integration of broad cw EPR spectra appears, namely that it is almost impossible to retrieve the baseline correctly. Especially broad features might be distorted. Fig. 5.8a shows such an attempt of integrating $V_{\text{ind}}(t)$. The baseline was corrected such that $M_z(t)$, averaged over a pulse cycle, decreases continuously during and increases again after the pulse train, and that $M_z(t)$ does not exceeds its value before the first pulse was applied. However, this procedure is not very robust because it assumes that no other sources,

for example of instrumental origin, contribute to the signal. After the integration, a denoising procedure with two consecutive moving averages over 8 ns was applied. The result is at least during the pulse train as expected in the sense that $M_z(t)$ shows a cyclic behaviour with the frequency of the pulse repetition rate in the short term and decreases exponentially in the long term. This can be explained with the short T_2 value of metal complex samples such as $\text{Cu}(\text{pic})_2$ at room temperature. $T_2\omega_1 < 1/2$ even for the maximum achievable mw field strength, thus magnetization does not nutate during mw irradiation. Between the pulses, $M_z(t)$ relaxes with T_1 towards M_0 . The behaviour of the magnetization transient after the pulse train does not meet the expectations well, because no fast changes of $M_z(t)$ are induced anymore. And the smaller the slope of a function, the more vulnerable is its integrated form to noise of any kind. Another reason could be that as long as the temporal change of M_z is caused by relaxation and not by an mw pulse, no distinction can be made between on-resonant and off-resonant polarization with such a broadband detection scheme. Therefore the observed curve includes also non-equilibrium polarization caused by diffusion processes. If a sample is affected considerably by diffusion, it is not surprising to obtain a non-exponential relaxation curve.

To look at the short term behaviour more closely, a baseline correction with a high-order polynomial was performed on the full data transient. In Fig. 5.8b, the results of this analysis is shown. The upper graph compares the transient that is denoised with two consecutive moving average procedures over 16 ns (*lower trace*) with the original transient obtained after integration (*upper trace*). We can see that besides the long-term relaxation, which is most probably due to diffusion, almost immediately an oscillatory steady-state is reached. Therefore we can try to obtain an improved image of the behaviour of $M_z(t)$ during one pulse cycle by summing up different pieces of the full trace that are shifted by the pulse spacing of 80 ns. However, as we have seen above, the noise has its largest fraction at integer multiples of a resonance period of the detector. Therefore they sum up as well instead of being annihilated. The result of such a procedure, starting after the sixth pulse, is shown in the lower graph of Fig. 5.8b, where a single moving average was performed before summing up the pieces. One can see that the beginning and

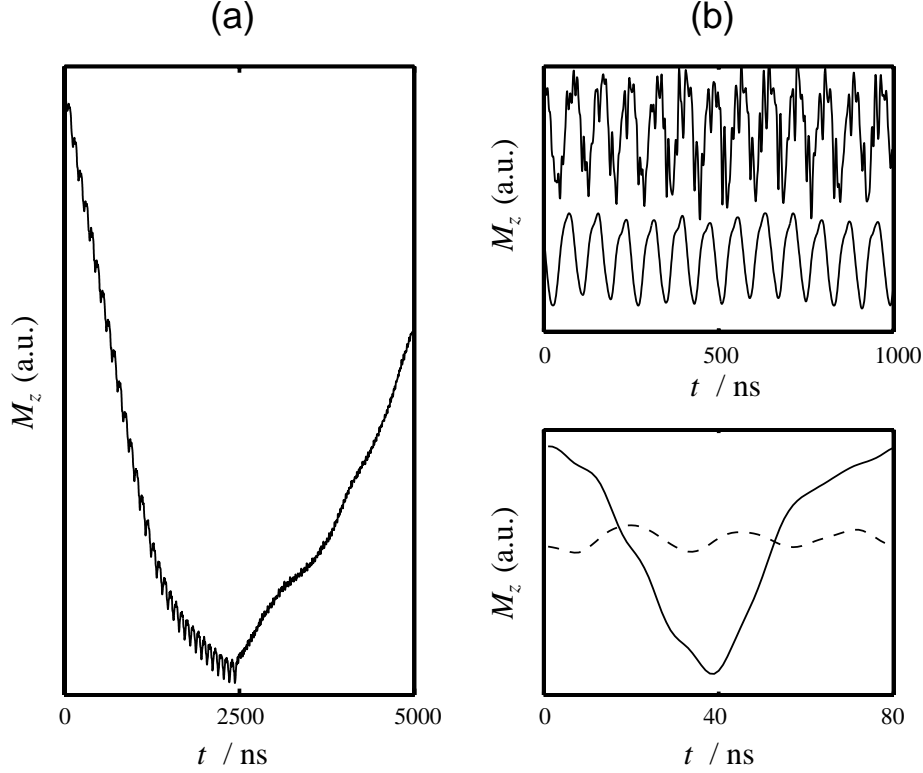


Figure 5.8: $M_z(t)$ of $\text{Cu}(\text{pic})_2$ during and after an mw pulse train. (a) $M_z(t)$ obtained by integrating the reconstructed V_{ind} of an experiment. (b) Clipping of the full trace after a high-order polynomial baseline correction. (upper graph) Comparison between the transient obtained without denoising (top) with a trace that is strongly denoised with two consecutive moving averages over 16 ns each (bottom). (lower graph) Trace between the beginning of two mw pulses. The trace was denoised by summing up $M_z(t)$ during the last 25 of 31 cycles of the pulse train. (full line) Signal during the pulse train, denoised with a single moving average over 16 ns. (dashed line) For comparison, the same procedure was applied to $M_z(t)$ after the end of the pulse train.

the end of the trace are almost at the same height, which confirms our procedure. For comparison, the same procedure was applied to the part of the signal after the pulse train (dashed line).

5.3.3 Discussion of the Results

As a first point, one can say that Eq. (3.7) describes our detection setup very accurately. After the recovery of $V_{\text{ind}}(t)$ with this formula, the enhanced spectral component at ω_{Ξ} vanishes completely after the pulse train, while the periodic trace

of $M_z(t)$ during the pulse train is clearly visible. This equation can also be used to determine ω_{Ξ} and Q_{Ξ} very precisely from a measured transient. If this is to be done, it is inevitable to have a very high sampling rate for the data points of the measured time transient.

Because of its low sensitivity, its high susceptibility to systematic errors and the costly data analysis, the only practical use of this experiment might be in fundamental studies. For example, it could be used to investigate diffusion processes, especially in combination with methods to monitor on-resonant changes of M_z .

This experiment shows the importance of a sensitive detection circuit with a high Q_{Ξ} . It would be very difficult to build a broadband detector that is still sensitive enough for routine measurements. However, in chapter 7, a method is presented where broadband information is obtained with a different approach, which is adapted to a special class of problems.

Chapter 6

Field-Swept EPR Measurements

In this chapter, the feasibility and the properties of field-swept EPR experiments with LOD is discussed. Two new pulse schemes based on the polarization detectors introduced in the last chapter are presented. Finally, the usefulness of the same basic setup for cw LOD experiments with modulation of the mw field amplitude is demonstrated.

6.1 Transient-Nutation LOD EPR

6.1.1 Principle of the Experiment

A simple nutation pulse or a composite nutation pulse with refocusing of magnetization, as discussed in chapter 5, can be used to record a field-swept EPR spectrum. This approach is called *transient-nutation longitudinally detected EPR* (TN-LOD EPR) [81]. In chapter 2 it was shown that the nutation frequency for an $S = 1/2$ spin system with isotropic g value is

$$\omega_{\text{eff}} = \sqrt{\omega_1^2 + \Omega_S^2}. \quad (6.1)$$

Because of the Ω_S dependence of ω_{eff} , the condition for the maximum signal, *i.e.* $\omega_{\text{eff}} = \omega_{\Xi}$, cannot be fulfilled with a constant ω_1 at all field positions of a spectrum. This will be addressed later. The optimum result in terms of a minimum linewidth

and spectral distortions is obtained when

$$\omega_1 = \omega_{\Xi}, \quad (6.2)$$

i.e. when the on-resonant nutation frequency is equal to the detection frequency. In Fig. 6.1, TN-LOD EPR spectra at room temperature of a coal sample with a narrow radical signal and a broad signal from an iron impurity without (Fig. 6.1a) and with (Fig. 6.1b) refocusing of magnetization are compared with the corresponding integrated cw EPR spectrum (Fig. 6.1c). The detection frequency for the TN-LOD spectra was $\omega_{\Xi}/2\pi = 12.5$ MHz. They were recorded in 10 min with a resolution of 601 data points. Three minutes of the recording time were used for data acquisition; the rest was instrumental overhead to transfer the data

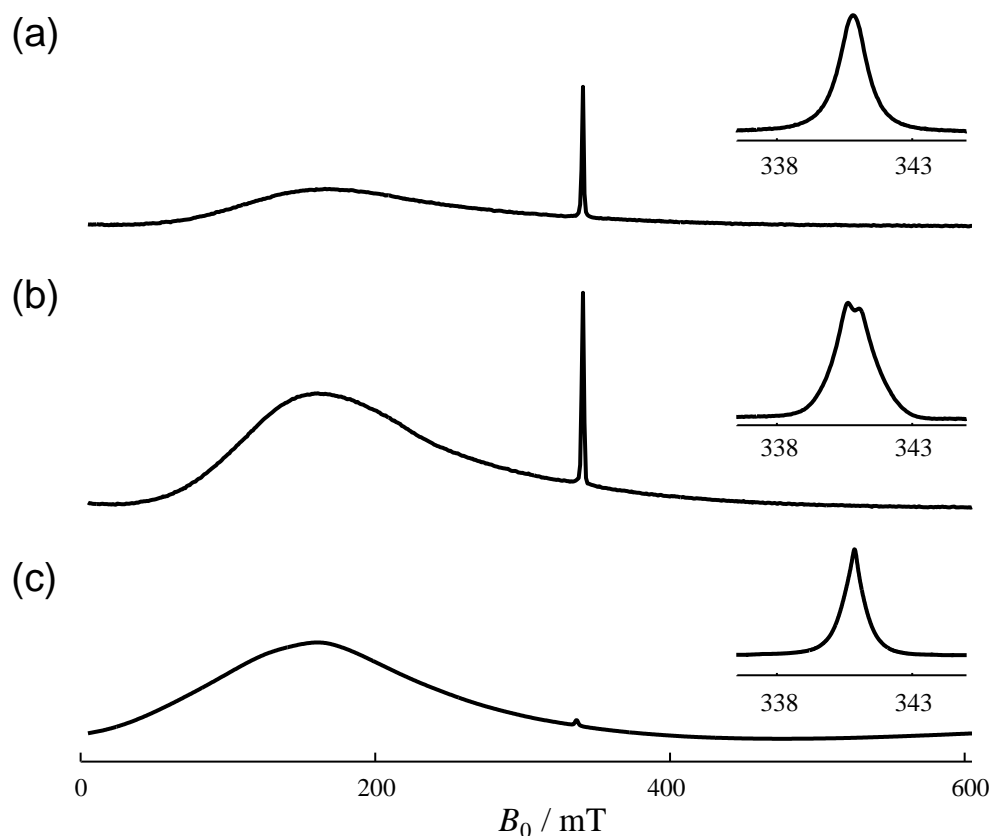


Figure 6.1: EPR experiment of a coal sample. (a) TN-LOD EPR spectrum without refocusing of the magnetization. The length of the mw pulse was $1 \mu\text{s}$. (b) TN-LOD EPR spectrum with refocusing of the magnetization. The pulse consists of one segment of length $t_p = 160$ ns and eight segments of length $2t_p$. (c) Integrated cw EPR spectrum.

to the computer and to reset the pulse programmer. All pulse LOD experiments with transient detection suffered from such an overhead, which was almost zero in the cw LOD experiments that are discussed later. The insets in Fig. 6.1ab were recorded with identical parameters than the full spectra except for a higher resolution with a reduced sweep width. For the cw EPR spectrum shown in 6.1c a modulation amplitude of 2.3 mT (inset: 0.1 mT) and an mw power of 0.2 W (inset: 20 μ W) were used.

The iron spectrum in Fig. 6.1a is three times weaker in intensity than in the corresponding spectrum in Fig. 6.1b. An S/N ratio of 40 is found for the iron spectrum in 6.1a and of 130 in 6.1b. The reason for this is the influence of the relaxation time of the sample on the observed signal when a nutation pulse is used as polarization detector. This topic was addressed in chapter 5. It was shown that two different mechanisms are responsible for a signal, depending on the factor $T_2\omega_1$. In a field-swept EPR experiment, this has different implications. First of all, a signal inducing mechanism exists for all possible values of T_2 . While the approach of M_z towards its steady-state value during a pulse without refocusing and its relaxation towards Boltzmann equilibrium afterwards is the only signal inducing mechanism for a sample with $T_2\omega_1 < 1/2$, the refocusing acts like a phase modulation. The signal is increased with the number of refocusing pulse segments and with a shorter time between the phase switching. Thus the dependence of the signal on the length of the pulse segments is very different for samples with $T_2\omega_1 < 1/2$ and samples with $T_2\omega_1 \gg 1/2$. The situation becomes more complicated with samples where $T_2\omega_1$ is larger than 1/2, but not several orders of magnitude. Especially for short T_1 , *i.e.* if $T_1 \approx T_2$, both mechanisms contribute comparably to the signal.

When the three insets with the radical spectrum in Fig. 6.1a-c are compared, a number of differences can be observed, mainly the unequal line shape of the TN-LOD EPR compared with the integrated cw EPR spectrum. This has different reasons. First of all, the height of the sample was approximately equal to the height of the resonator, thus not all spins experience the same B_1 . Hence the optimum condition given in Eq. 6.2 is not fulfilled for all spin packets at the same mw power, and narrow lines might be broadened. This effect is not very dominant because for an optimum signal, $\omega_{1,\max}$ is only slightly higher than ω_{Ξ} . If Ω_S is

increased, ω_{eff} rises likewise, thus for relatively small Ω_S the point is reached where $\omega_{\text{eff}} > \omega_{\Xi}$. For larger Ω_S the signal intensity decreases quickly. A much more important reason for the varying line shapes is the nature of the coal sample, which consists of several radical components with different linewidths. For one dominant radical component with a small linewidth, one finds $T_1 \approx T_2$, which is a favourable condition for the detection of field-modulated cw EPR spectra, especially with the low mw power used in this measurement. Therefore the relative intensity of this narrow line compared to the broader line of another component with $T_1 \gg T_2$ is larger in the conventional cw EPR spectrum than in the TN-LOD EPR spectrum, where the contribution of the narrower line to the signal is small. This model can be easily verified with a pulse echo-detected EPR experiment, where the same result as with the TN-LOD EPR was obtained, since from the narrow line only an FID but no echo could be observed, while the other dominant component – or components – showed a nice echo at room temperature.

The reason for the splitting of the radical line in the TN-LOD EPR experiment with refocusing of magnetization was already discussed in chapter 5. Because of ambiguities regarding the adjustment of the optimum mw field strength caused by the distribution of B_1 over the sample volume, the same attenuator setting as in the experiment without refocusing was used. But this entails a discontinuity in the time derivative of $M_z(t)$ at the positions of the mw phase switching. The maximum signal is induced at B_0 field positions with smooth progression of $M_z(t)$, which is somewhat off-resonance. Thus the magnitude of the splitting is not determined by a physical property, but by the discrepancy between the actual and the optimum mw field strength. This splitting cannot be removed easily by adjusting one of the parameters in the data analysis. To avoid it, it is inevitable to exactly adjust the B_1 field value, which can be a difficult task, as was described before. It might be even necessary to first perform some adjustment measurements. Another possibility would be to use point-like samples, which is often not possible because of a low signal intensity. Finally it can be even necessary to do the experiment without refocusing of M_z for samples with narrow lines.

To summarize the results, one can say that TN-LOD EPR is especially suited for samples consisting of different species with very different relaxation times, be-

cause a signal inducing mechanism exists for each relaxation time range. Since the absorption spectrum and not its first derivative is measured, the method performs equally well for spectra with very broad lines. Another application can be to disentangle spectra consisting of more than one component by comparing it with a cw EPR spectrum. The two methods have a different signal dependence on the relaxation time. TN-LOD EPR is not restricted to samples in the solid state. It can be used for liquids as well.

6.1.2 Microwave Power Dependence of the Signal

Because ω_{eff} depends on Ω_S , a few additional points must be considered in a field-swept experiment compared to the simple polarization detector discussed in the last chapter. This discussion is illustrated with an experimental example using a sample of γ -irradiated Herasil glass whose EPR spectrum was recorded as a function of the mw field amplitude (Fig. 6.2). The height of the sample was approximately equal to the resonator height, thus it experienced the full B_1 inhomogeneity discussed in §4.4.1. The measurements were made with a TN-LOD EPR scheme with refocusing of magnetization. The nutation pulse was divided into 21 segments of 400 ns length with alternately inverted phase. For the discussion of the B_1 dependence of the signal, the full transient was used for data analysis. The same data can be used later to discuss the data analysis itself. The first question to be analyzed is what happens if the on-resonant nutation frequency is not equal to the detection frequency, *i.e.* if $\omega_1 \neq \omega_{\Xi}$. For $\omega_1 > \omega_{\Xi}$, it is not possible to meet the condition $\omega_{\text{eff}} = \omega_{\Xi}$. Thus the signal intensity is reduced, and depending on the experimental procedure, the lines might be additionally broadened and distorted, especially if $\omega_1 \gg \omega_{\Xi}$. This signal reduction and line distortion can be seen by comparing the middle with the bottom spectrum in Fig. 6.2b. If $\omega_1 < \omega_{\Xi}$, the condition $\omega_{\text{eff}} = \omega_{\Xi}$ is fulfilled at the off-resonant field positions $\Omega_S = \pm \sqrt{\omega_{\Xi}^2 - \omega_1^2}$. Narrow EPR lines with a width of the order of ω_{Ξ} or smaller may be split into two peaks separated by $2\sqrt{\omega_{\Xi}^2 - \omega_1^2}$. If $\omega_1 \ll \omega_{\Xi}$, this condition is met at $\omega_{\text{eff}} \approx \Omega_S$. Of course, in this case the nutation angle θ becomes small, and so does the signal. If the whole spectrum is narrower than $2\omega_{\Xi}$, it is doubled, with the two copies shifted by $\pm\omega_{\Xi}$ from their actual position. Another consequence is that if the B_1

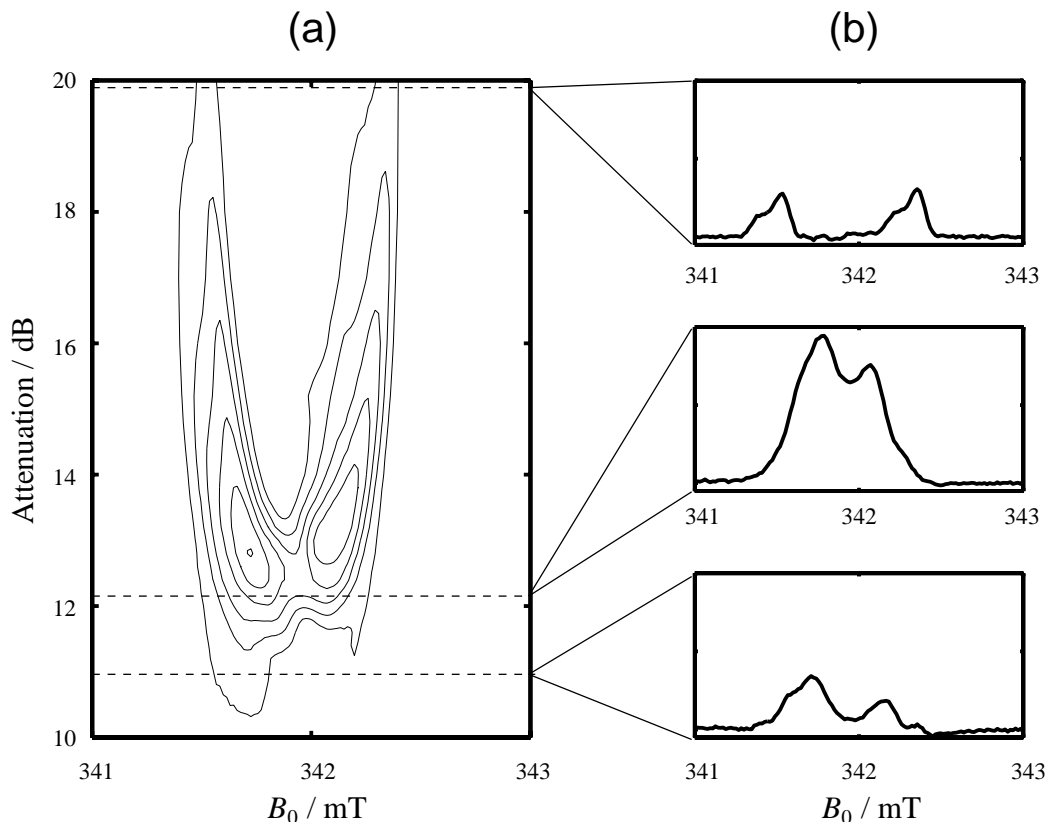


Figure 6.2: TN-LOD EPR spectrum of γ -irradiated Herasil glass as a function of the mw power. The mw pulse is subdivided into 21 segments of 400 ns length with alternating phases to refocus magnetization. $\omega_{\Xi}/2\pi = 12.5$ MHz. (a) Contour plot of the spectrum vs. the attenuation of the mw power. (b) Spectrum at three different power levels. Their intensities are directly comparable. (top) $\omega_1 \ll \omega_{\Xi}$. (middle) $\omega_1 \approx \omega_{\Xi}$, where the maximum signal is obtained. (bottom) $\omega_1 > \omega_{\Xi}$.

distribution is a major source for line broadening, its influence decreases continuously with decreasing mw power, because at the position with maximum signal Ω_S becomes the main contributor to ω_{eff} , and the relative influence of ω_1 becomes very small. Thus line broadening caused by an inhomogeneous B_1 field is reduced, finally ending up with a spectrum with natural line widths. This can be seen on the top slice of Fig. 6.2b, where the well-known Herasil spectrum is visible twice, separated by approximately $2\omega_{\Xi}$. Each copy has the same width and shape as is obtained in a cw EPR spectrum.

6.1.3 Variation of the Detection Frequency

To obtain the EPR spectrum, each transient trace is reduced to one point whose amplitude represents the signal at the respective B_0 field position. This value is usually calculated as the spectral component of the signal at ω_{Ξ} , as was described in chapter 5. But in principle, any frequency ω_d could be chosen, the signal amplitude decreasing with larger $|\omega_d - \omega_{\Xi}|$. The consequence of an arbitrary ω_d can be discussed again with Eq. (6.1) for an $S = 1/2$ spin system. The signal is maximum for a certain detection frequency for those spin packets where $\omega_{\text{eff}} = \omega_d$. Thus we get the maximum signal for a given ω_1 if

$$\Omega_S = \pm \sqrt{\omega_d^2 - \omega_1^2}. \quad (6.3)$$

This equation has only real solutions for $\omega_d \geq \omega_1$. If $\omega_d > \omega_1$, narrow EPR lines with a width on the order of ω_d or smaller may be split into two peaks separated by $2\sqrt{\omega_d^2 - \omega_1^2}$. If $\omega_d \gg \omega_1$, this condition is met at $\Omega_S \approx \pm\omega_d$. This means the splitting becomes larger with increasing ω_d , approaching an asymptotic line. For $\omega_d < \omega_1$, the signal gets weak and very noisy. In Fig. 6.3 the TN-LOD EPR spectrum without refocusing of a small sample of lithium phthalocyanine is shown as a function of ω_d . Because the signal for all ω_d outside the bandwidth of the detection circuit is much lower than at ω_{Ξ} , each trace in the ω_d dimension is scaled to the same maximum value. The trace at 20 MHz is extremely noisy because of a very strong signal with instrumental origin at that frequency. Modulations above 20 MHz were actively suppressed by the use of a low pass filter, thus the noticeably increased noise level. This analysis can only be performed if B_1 is within a very small range for all spin packets such that no other effects like those discussed in §6.1.2 are superimposed. For a sample in an inhomogeneous B_1 field, the noise becomes large if ω_d is not within the bandwidth of the detection circuit. For example, the γ -irradiated Herasil glass that was used in the last section could not be used for this analysis.

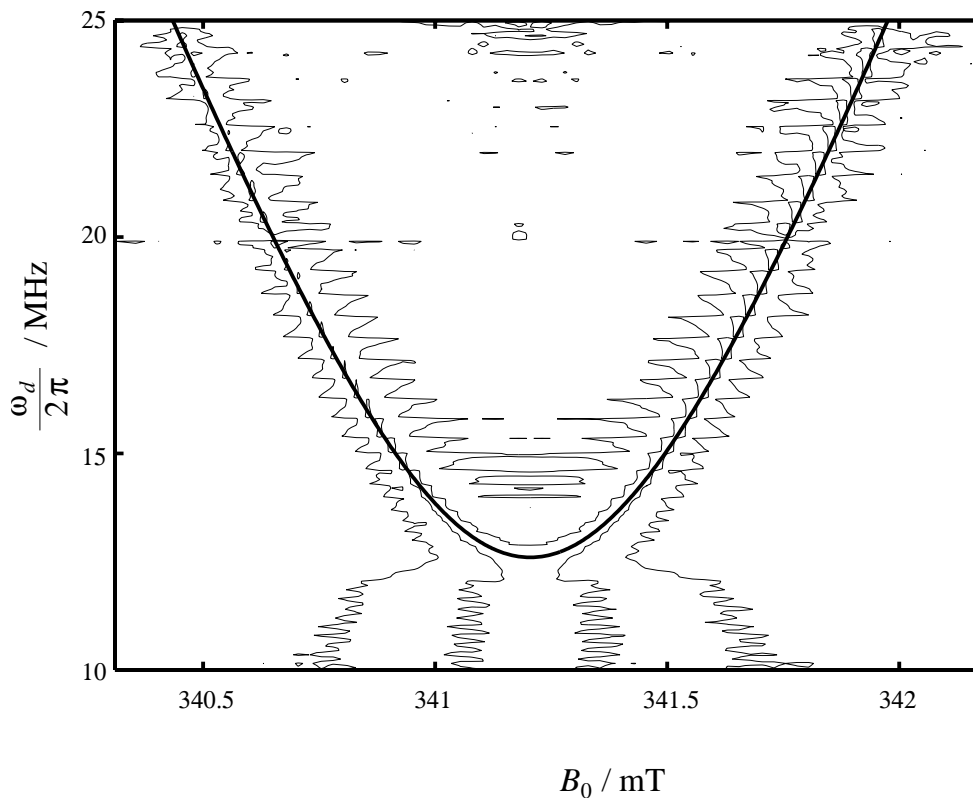


Figure 6.3: TN-LOD EPR spectrum without refocusing of magnetization of lithium phthalocyanine as a function of ω_d . The mw pulse had a length of $1.5 \mu\text{s}$. $\omega_{\Xi} = 12.6 \text{ MHz}$. The signal at each trace in the ω_d dimension is scaled to the same maximum value. The solid line represents the expected position of the line according to Eq. (6.3).

6.2 Pulse-Train LOD EPR

Another excitation scheme to measure EPR spectra with LOD uses a train of mw pulses of length t_p , separated by the pulse repetition time t_{rep} (Fig. 6.4a). It is called *pulse-train excited longitudinally detected EPR* (PT-LOD EPR). Such an excitation scheme has already been used for LOD experiments with shot repetition frequencies $1/t_s$ between 1 and 10 kHz and $t_s \gg t_p$ [13]. In this earlier approach the sequence consisted of a large number of π pulses. Between the pulses, the spin magnetization relaxed towards its Boltzmann equilibrium. The resonant circuit with frequency $\omega_{\Xi} = 2\pi/t_s$ filtered the first Fourier component of the periodically changing z magnetization. The sinusoidal signal was recorded with a phase-sensitive detector (PSD). In the approach proposed here, a pulse repetition

frequency $1/t_{\text{rep}} = \omega_{\Xi}/2\pi$ of about 10 MHz is used, and t_{rep} and t_p are of the same order of magnitude. This corresponds to an increase of the detection frequency by three to four orders of magnitude compared to the former scheme, and the signal intensity is concentrated on the fundamental frequency and a few higher harmonics. In contrast to the low-frequency approach, detection is done with a transient recorder, since the length of the pulse train is limited by the duty cycle of the TWT amplifier.

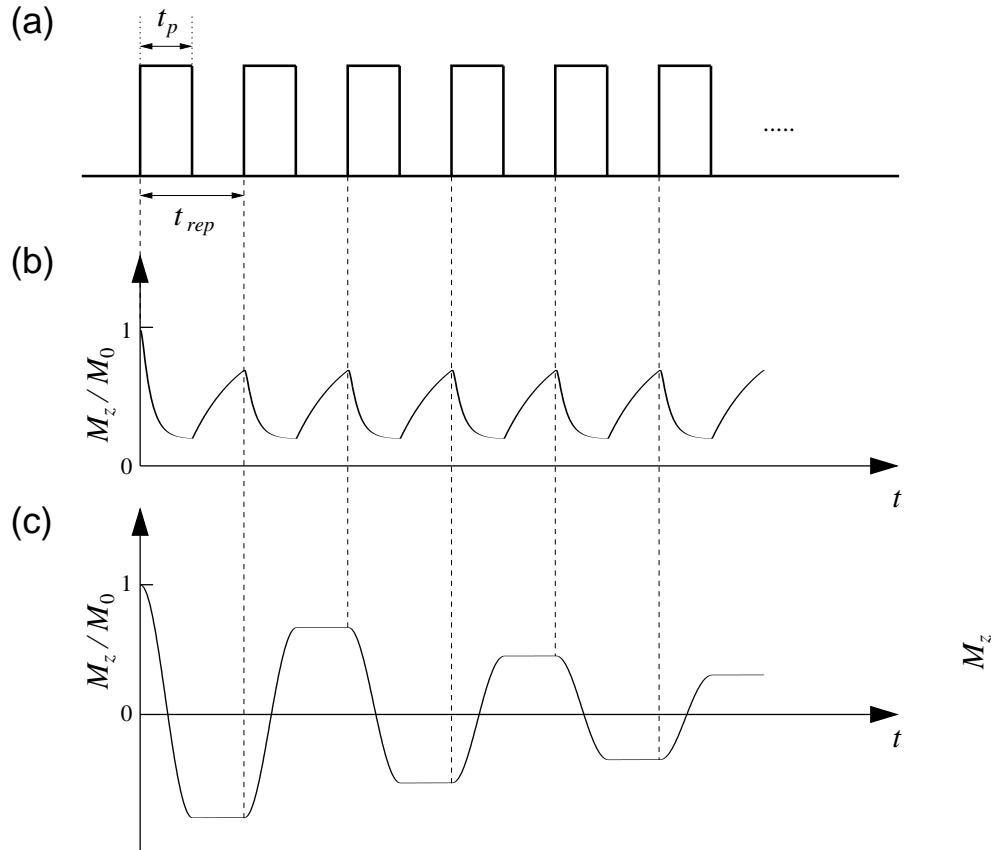


Figure 6.4: Schematic of the PT-LOD EPR experiment. (a) Pulse sequence consisting of a train of π pulses of length t_p and a pulse repetition time $t_{\text{rep}} = 2t_p$. (b) Behavior of the M_z magnetization for the case $T_2 \ll 2\pi/\omega_{\Xi}$. Parameters used for the simulation were $t_{\text{rep}} = 80$ ns, $T_1 = 40$ ns, $T_2 = 1$ ns. (c) Behavior of the M_z magnetization for the case $T_1 \gg 2\pi/\omega_{\Xi}$ and T_2 on the order of $2\pi/\omega_{\Xi}$. The pulse sequence inverts the magnetization periodically (parameters: $T_1 = 40$ μ s, $T_2 = 100$ ns).

As in the TN-LOD EPR experiment, the signal observed in the PT-LOD experiment strongly depends on the effect of the mw pulses on the spin system, *i.e.*,

whether the magnetization can be inverted several times with strong mw pulses. Two cases will be discussed separately.

No inversion of the magnetization possible ($T_2 \ll 2\pi/\omega_{\Xi}$): In this case the magnetization approaches its steady-state value during each pulse and partially recovers between the pulses. This is shown in Fig. 6.4b for $t_{\text{rep}} = 2t_p$. t_{rep} must be set to

$$t_{\text{rep}} = 2\pi n/\omega_{\Xi}, \quad (6.4)$$

where n is a positive integer; otherwise the signals induced by the different pulses do not have the same phase, which reduces the detected signal. After a few cycles, the magnetization reaches an oscillatory steady state. In the limit of a pulse train with an infinite number of pulses and for $t_{\text{rep}} = 2t_p$, the only difference between this method and the cw LOD experiment with a square-wave modulation of the mw field amplitude is to use a transient recorder instead of a PSD for detection.

At least partial inversion of magnetization possible, and $T_1 \gg t_{\text{rep}}$: In this case $M_z(t)$ remains virtually unchanged between two consecutive pulses, so that the maximum signal is obtained with flip angles of 180° (Fig. 6.4c). The decay of the magnetization caused by the inhomogeneous B_1 field and inhomogeneous EPR lines can partially be refocused by alternately inverting the phase of the pulses. The change in M_z is thus periodic with $2t_{\text{rep}}$, and a repetition time $t_{\text{rep}} = \pi/\omega_{\Xi}$ must be used for maximum signal intensity. The measured signal will first increase and then slowly decrease to a low steady-state value. Lines with a width smaller than the excitation bandwidth of the pulses will be broadened and distorted. For optimum sensitivity, the same rules apply for the choice of the repetition time between two pulse trains as in pulse echo experiments [22].

Figure 6.5 shows the PT-LOD EPR spectrum of 1 % bis(picolinato)Cu(II) diluted into a powder of the corresponding zinc complex. The spectrum was recorded at room temperature with a resonant frequency $\omega_{\Xi}/2\pi = 12.5$ MHz. It was measured with 500 data points in 8 min and was obtained with a train of 31 mw pulses of length 40 ns. An mw power of 150 W and a pulse repetition time $t_{\text{rep}} = 80$ ns were used. An S/N ratio of 350 was achieved.

PT-LOD EPR is easier to implement than TN-LOD EPR because the adjustment of the mw power is less critical. The approach is most sensitive for para-

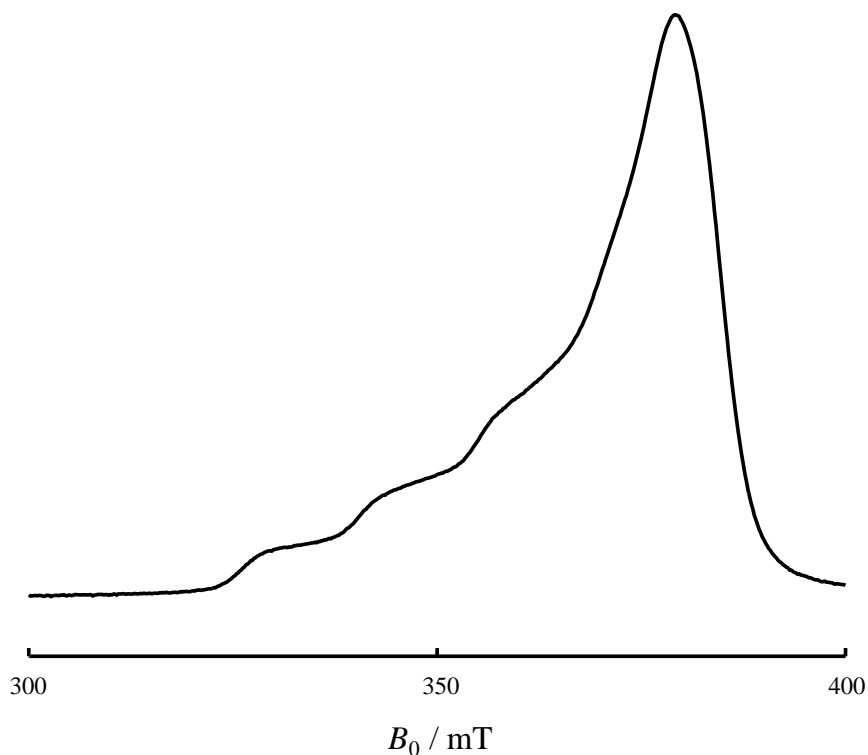


Figure 6.5: PT-LOD powder EPR spectrum of 1 % bis(picolinato)Cu(II) diluted into the corresponding zinc complex (mw frequency 9.6355 GHz).

magnetic species with T_1 on the order of or shorter than an oscillation period of the detection circuit. The PT-LOD experiment can be considered as a high-power variation with a limited duty cycle of the cw LOD EPR experiment with amplitude modulation, which is discussed next.

6.3 CW LOD EPR Methods

This class of experiments where the signal is induced by an amplitude modulated continuous mw field was discussed in some details in previous chapters, and it is only necessary to demonstrate the performance of the setup for this kind of experiments with some examples.

The cw LOD powder EPR spectrum of Mn(II)-doped NH_4Cl (0.08 %) [82] recorded with a square-wave modulated mw field is shown in Fig. 6.6a. The quality factor of the mw resonator was $Q_L = 700$ and the mw power was 5 W. The

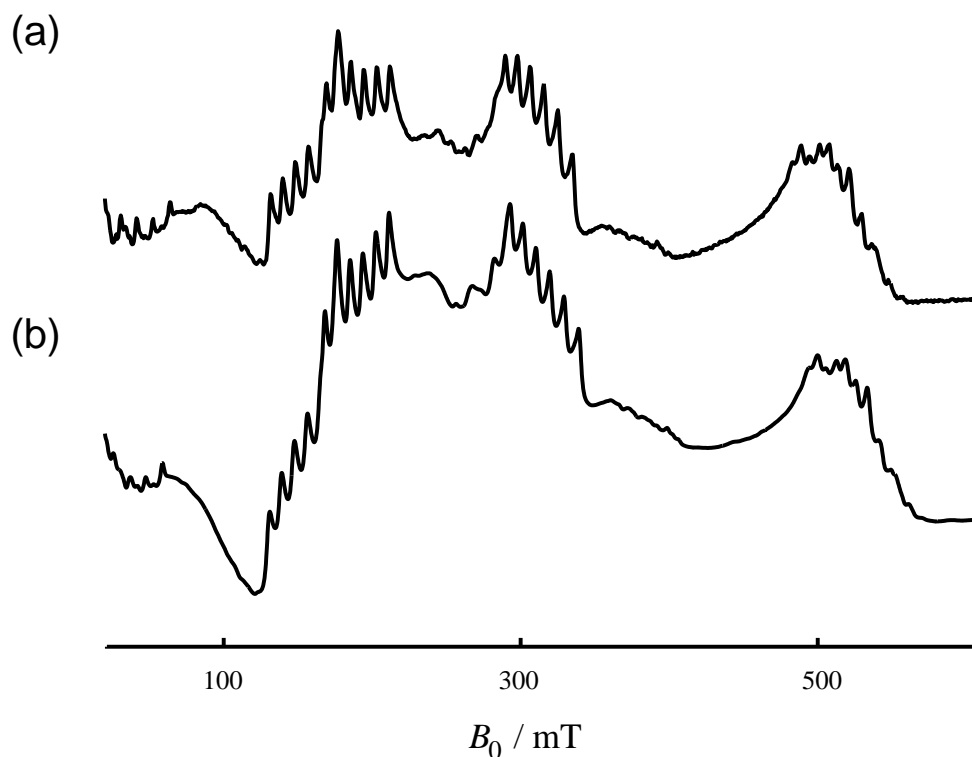


Figure 6.6: Continuous wave LOD EPR experiment. (a) LOD EPR spectrum of a powder of Mn-doped NH_4Cl recorded at room temperature with a square-wave modulated mw field (mw frequency 9.6303 GHz). (b) Corresponding integrated cw EPR spectrum (mw frequency 9.7686 GHz).

spectrum with an S/N ratio of about 120 was measured in 2 min with a resolution of 1024 data points. For comparison, the integrated cw EPR spectrum is shown in Fig. 6.6b. It is difficult to get the correct baseline for a cw EPR spectrum that covers such a wide field range. For cw LOD EPR the linewidth and the width of the spectrum represent no limitations since the absorption spectrum instead of its first derivative is detected. The small shift in the field axis of the two spectra is caused by the use of two slightly different mw frequencies.

Since in this setup the pick-up coil is placed inside the resonator, spurious lines from paramagnetic impurities in the dielectric ring do not disturb the spectrum. This is often a problem in cw EPR experiments using this resonator type.

A single crystal of VO^{2+} in $\text{Mg}(\text{NH}_4)_2(\text{SO}_4) \cdot 6 \text{H}_2\text{O}$, which was considerably smaller than the Mn(II)-doped NH_4Cl sample, was measured in another experi-

ment (Fig. 6.7). To avoid line broadening the mw power was limited to 0.5 W, and

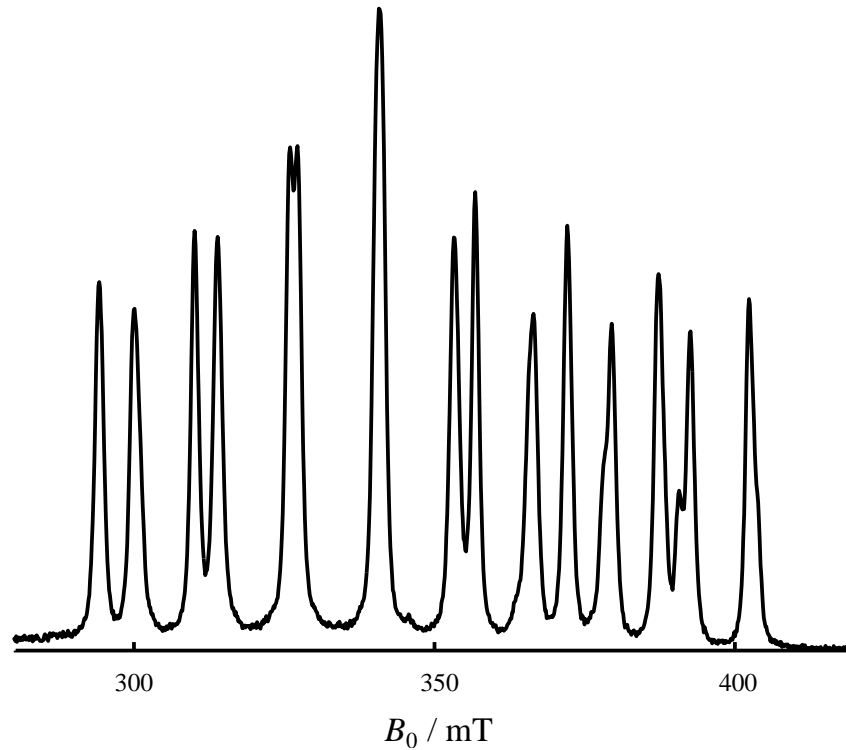


Figure 6.7: CW LOD EPR spectrum with square modulation of B_1 of a single crystal of VO^{2+} in $\text{Mg}(\text{NH}_4)_2(\text{SO}_4) \cdot 6 \text{H}_2\text{O}$.

the resonator was overcoupled to $Q_l \approx 1000$. A recording time of 2 h was required to get a S/N ratio of ≈ 100 with 1024 field values.

Chapter 7

Spin-Lattice Relaxation Time Measurement

In this chapter, different concepts to measure longitudinal relaxation times with LOD are discussed. None of them is based on new models, but they are advancements of well known techniques. Additionally, a summary of the techniques for data analysis is given.

7.1 Data Processing

For indirect methods to measure relaxation times, data analysis is usually very simple, because a measured parameter is directly connected to the relaxation time. The problem there is that the model used to derive the method might be appropriate only for a limited number of samples, or that it requires magnetization to relax mono-exponentially with a sharp value of the relaxation time. Systems consisting of more than one component or with a continuous distribution of relaxation times may lead to ambiguous or even wrong results. Much more flexible are methods that directly provide the full relaxation pattern. In principle, arbitrary relaxation mechanisms can be disentangled in this way. On the other hand, data analysis becomes much more complex, especially if complicated functions must be used to describe the relaxation trace and if the experimental data is noisy. To perform such an analysis, two different strategies have been used in the past. One is to fit the parameters of a predefined function to the measured data with a minimization algorithm, and the other is to calculate a quasi-continuous distribution of relaxation

times from a relaxation curve. Both of them are discussed briefly.

An important aspect to improve the result of a relaxation time measurement without enlarging the measuring time is to exponentially space the data points. In this way, the region with a high rate of change of $M_z(t)$ is sampled more accurately, allowing a more reliable fit of the data, while it is still possible to record the whole relaxation pattern until the equilibrium value M_0 is reached. Both procedures for data analysis presented here can easily handle arbitrarily spaced data points.

7.1.1 Determination of Relaxation Times by Curve Fitting

Relaxation transients can be fitted with a least-square minimization algorithm. Arbitrary functions can be fitted with this procedure, but the functions must be known in advance. In magnetic resonance, longitudinal relaxation can often be described with the function

$$S(t) = \sum_{i=1}^n A_i \left[1 - k_i \exp \left(- \left(\frac{t}{T_{1,i}} \right)^{\alpha_i} \right) \right], \quad (7.1)$$

where A_i is the amplitude of component i , k_i represents the efficiency of the inversion or the saturation process with an optimum of $k_i = 2$ for IR and $k_i = 1$ for SR experiments, $T_{1,i}$ is the relaxation time, and α_i is a parameter accounting for a distribution of $T_{1,i}$ that leads to a stretched exponential. We get $\alpha_i = 1$ if $T_{1,i}$ has a sharp value, and $\alpha_i < 1$ in case of a distribution of $T_{1,i}$. In the latter case the analysis depends on the shape and the width of the $T_{1,i}$ distribution and is usually not trivial. This parameter has been used mainly to analyze the pore size of porous rocks and the size of biological cells [83]. The number n of components to be fitted has to be preset. If it is not exactly known in advance, it can be estimated by iteratively increasing n and manually analyze the residuals between experiment and fit.

To allow for a stable fit the number of parameters to be fitted should be kept as small as possible. In Eq. (7.1), this number can be reduced by subtracting the signal amplitude $S_0 = \sum_i A_i$, corresponding to an infinite evolution time between

preparation and detection. We get the simplified formula

$$S(t) - S_0 = - \sum_{i=1}^n b_i \exp \left(- \left(\frac{t}{T_{1,i}} \right)^{\alpha_i} \right) \quad (7.2)$$

with $b_i = A_i k_i$. In general, we can state that the larger n , the more difficult it becomes to get a reproducible fit that does not strongly depend on the initial values for the minimization, because especially with noisy data it is often possible to fit the same multi-exponential decay with strongly differing relaxation times and still get an almost equivalent result. This problem becomes more pronounced if different components have similar $T_{1,i}$ values. With the MARQUARDT-NEWTON-GAUSS minimization algorithm [84] used for this work, it was very difficult to fit data with $n > 3$ if only one independent set of data was available. The situation is much better when $T_{1,i}$ can be fitted to a set of independent measurements where the only property that changes between the traces is A_i . This can be a two-dimensional experiment with the relaxation transient in one and a second property like the B_0 field in the other dimension if $T_{1,i}$ are field independent. In this case it is possible to separate a spectrum that contains different components with respect to B_0 by fitting one set of k_i and $T_{1,i}$, and calculating $A_i(B_0)$ for each field position. Note that it is very important to know the correct baseline in such an experiment to get a sensible result.

7.1.2 Inversion of Multi-Exponential Decay Data

A different approach is to calculate a quasi-continuous relaxation time distribution. This problem can be formulated as a Fredholm equation of the first kind with the general form [84]

$$s(t) = \int_{T_{\min}}^{T_{\max}} K(t, T) f(T) dT, \quad (7.3)$$

where T_{\min} and T_{\max} mark the limits of the distribution to be calculated, $s(t)$ are the experimental data, and $f(T)$ is the unknown function to be solved for. $K(t, T)$ is called the *kernel*. For an IR experiment with complete inversion of M_z , this would be

$$K(t, T) = 1 - 2e^{-t/T}. \quad (7.4)$$

Eq. (7.3) is analogous to the matrix equation

$$\mathbf{K} \cdot \mathbf{f} = \mathbf{g} \quad (7.5)$$

whose solution is $\mathbf{f} = \mathbf{K}^{-1} \cdot \mathbf{g}$ with the inverse matrix \mathbf{K}^{-1} . Like Eq. (7.3), Eq. (7.5) has a unique solution whenever \mathbf{g} is non-zero and \mathbf{K} can be inverted. However, Fredholm equations of the first kind are often extremely ill-conditioned. Applying the kernel to a function is generally a smoothing operation, so the solution, which requires an inversion of the operator, will be extremely sensitive to small changes or errors in the input data. Smoothing actually often loses information, and there is no way to get it back in an inverse operation. Specialized methods have been developed for such equations, which are often called inverse problems. In general, a method must augment the information given with some prior knowledge of the nature of the solution [83,85], which is then used, in one way or another, to restore lost information.

7.1.3 Selection of Analysis Method

As a first step to choose the best method for data analysis, it should be summarized what is already known about the system and what is expected. Important facts are previous knowledge about the shape of the relaxation pattern, possible relaxation pathways, the number of different spin components in the sample, and of course the kind of information of interest.

Mono-Exponential Relaxation Pattern: This is the most convenient case to analyze. The curve-fitting routines are stable, and even noisy data can be analyzed reliably. There is no need to use an inversion algorithm.

Multi-Exponential Relaxation Pattern: If the number of components of the relaxation pattern is known and small, *i.e.* $n \leq 3$, and if these are well separated, a curve fitting algorithm might be preferred because of its simplicity. However, it is sometimes possible to fit the same experimental data either with one exponential and $\alpha < 1$, or with two exponentials and $\alpha_i = 1$. In any case, if a curve fitting is used, the model that is finally chosen should be physically reasonable. If at least one component of the relaxation curve has to be described with a distribution and its interpretation based on α_2 is not well-known, or if the number of different relax-

ation components is not known in advance and not easily obtained with iterative trial-and-error, an inversion algorithm is preferable.

Arbitrary Shape of the Relaxation Curve: In this case it is important if the mathematical form of this shape is known or not. If it is known, an inversion algorithm might be difficult to apply, while curve fitting to any algebraic function is feasible with standard methods. Thus this second method might be preferable. If the function is not known, one can use an inversion algorithm with a standard kernel and try to estimate the function from the shape of the obtained relaxation time distribution.

Correlation of Two Different Relaxation Times: This is, especially in NMR, a classical problem that corresponds to solving Fredholm integrals of the first kind in 2 and 2.5 dimensions. A computationally feasible method that can be performed on generally available computer hardware has been developed recently [86].

In the case of a fitting algorithm, it is necessary to have an initial guess for the relaxation time. The better this guess, the faster the fitting, and the risk of finding a local minimum instead of the global one can be minimized. The larger the number of different parameters to be fitted, the more important it becomes to have reasonable initial values. Otherwise the fitting procedure might end up in a result that physically does not make sense. Another problem might arise if two relaxation times are nearly equal. Depending on the noise level of the experimental data, a separation might be impossible.

7.1.4 Data Refinement

In relaxation time measurements the obtained data is sometimes rather noisy. Depending on the type of relaxation curve, the routine to fit the data may become unstable or not give any useful output at all. In some of the LOD methods presented later to determine longitudinal relaxation times, the problem is even more pronounced because an exponentially damped modulation with time constant τ ,

$$s_m(t) = a_m \exp\left(-\frac{t}{\tau}\right) \cos(\omega t), \quad (7.6)$$

whose amplitude a_m can be an order of magnitude larger than the signal induced by the difference between the initial and the equilibrium magnetization, is super-

imposed on the relaxation curve. If relaxation after an excitation can be described with an exponential according to Eq. (2.32) or a sum of exponentials, this knowledge can be used to mathematically denoise the data prior to the determination of the relaxation time by calculating the moving average over a period $T_p = 2\pi/\omega$ of the modulation, *i.e.* by calculating

$$\bar{s}(t) = \frac{1}{T_p} \int_{t-T_p/2}^{t+T_p/2} s(t') dt', \quad (7.7)$$

where the measured signal $s(t)$ is assumed to be a continuous stream of data. $s(t)$ can be divided into three parts, namely the signal $s_r(t)$ that gets its time dependence from the relaxation of $M_z(t)$, the detector ringing $s_m(t)$ and the random noise $s_w(t)$. The signal $s_r(t)$ can be divided further according to Eq. 2.32 into

$$s_r(t) = s_0 + (s_r(0) - s_0) e^{-t/T_1}, \quad (7.8)$$

with the signal s_0 from the spin system at Boltzmann equilibrium and the signal $s_r(0)$ at the beginning of the relaxation process.

If a moving average over T_p is applied to an undamped modulation with frequency ω , the modulation can be removed completely. To show the efficiency of this approach, we discuss how the moving average influences the relaxation time T_1 , what the residual is when the modulation is exponentially damped, and what the consequences are when T_p is not exactly a multiple of the difference between two adjacent data points.

The consequence of a moving average to the signal induced by the relaxing $M_z(t)$ can be calculated by integrating $s_r(t)$ over T_p . T_1 and T_p are not correlated, therefore the result is applicable to an arbitrary moving average over an exponential. We get

$$\begin{aligned} \bar{s}_r(t) &= \frac{1}{T_p} \int_{t-T_p/2}^{t+T_p/2} s_0 + (s_r(0) - s_0) e^{-t'/T_1} dt' \\ &= s_0 + \frac{T_1}{T_p/2} \sinh\left(\frac{T_p/2}{T_1}\right) (s_r(0) - s_0) e^{-t/T_1}. \end{aligned} \quad (7.9)$$

This result shows that for $T_p \ll T_1$ we get $\overline{s_r}(t) \approx s_r(t)$. If T_p is on the order of T_1 , $\overline{s_r}(t)$ has still the same shape as $s_r(t)$ with the same relaxation time T_1 , but with amplitude $\frac{T_1}{T_p/2} \sinh\left(\frac{T_p/2}{T_1}\right) > 1$. This has consequences if the decay is multi-exponential. After the moving average the relaxation curves with shorter T_1 values will become more intense relative to those with longer T_1 values.

For an exponentially damped cosine, integration over a modulation period T_p yields

$$\begin{aligned} \overline{s_m}(t) &= \frac{\omega}{2\pi} \int_{t-\frac{\pi}{\omega}}^{t+\frac{\pi}{\omega}} e^{-t'/\tau} \cos(\omega t') dt' \\ &= \frac{\omega\tau e^{-t/\tau}}{\pi(1+\omega^2\tau^2)} (\omega\tau \sin(\omega t) - \cos(\omega t)) \sinh\left(\frac{\pi}{\omega\tau}\right). \end{aligned} \quad (7.10)$$

Since a_m would only introduce a constant factor, it is omitted in Eq. (7.10) for simplicity. By substituting $Q_{\Xi} = \omega\tau/2$, where Q_{Ξ} is the quality factor of the detector, and assuming that $Q_{\Xi} \gg 1$, the effect of the moving average can be approximated by

$$\overline{s_m}(t) \approx \frac{e^{-t/\tau} \sin(\omega t)}{2Q_{\Xi}}. \quad (7.11)$$

This result shows that calculating a moving average over T_p reduces the modulation by a factor $2Q_{\Xi}$.

For an integration interval that deviates by $2\Delta/\omega$ from T_p , we find

$$\begin{aligned} \overline{s_m}(t) &= \frac{\omega}{2(\pi + \Delta)} \int_{t-\frac{\pi+\Delta}{\omega}}^{t+\frac{\pi+\Delta}{\omega}} e^{-t'/\tau} \cos(\omega t') dt' \\ &= \frac{\omega\tau e^{-t/\tau}}{2(\pi + \Delta)(1 + \omega^2\tau^2)} \\ &\quad \times \left[e^{(\pi+\Delta)/\omega\tau} (\omega\tau \sin(\omega t - \Delta) - \cos(\omega t - \Delta)) \right. \\ &\quad \left. - e^{-(\pi+\Delta)/\omega\tau} (\omega\tau \sin(\omega t + \Delta) - \cos(\omega t + \Delta)) \right]. \end{aligned} \quad (7.12)$$

With the assumptions $\Delta \ll \pi$ and $Q \gg 1$, we get

$$\overline{s_m}(t) \approx e^{-t/\tau} \left(\frac{1}{2Q} \cos \Delta \sin(\omega t) - \frac{1}{\pi + \Delta} \sin \Delta \cos(\omega t) \right). \quad (7.13)$$

There are two oscillatory terms in Eq. (7.13) which differ in phase by 90° . The sine function dominates if

$$\frac{\Delta}{\pi} < \frac{1}{2Q}. \quad (7.14)$$

In this case, we find the same result as in Eq. (7.11), weighted by $\cos \Delta$. If the other term dominates, the amplitude of the unwanted modulation is

$$\overline{s_m}(t) \approx -\frac{e^{-t/\tau} \cos(\omega t)}{1 + \pi/\Delta}, \quad (7.15)$$

therefore the original modulation is reduced by a factor $(1 + \pi/\Delta)$. For example, for a moving average over 11 data points separated by 8 ns and an oscillation period of 84 ns, the error is 4 ns, corresponding to $\pi/\Delta = 21$. The modulation amplitude is reduced to about 4.5 % of the initial value. If the remaining modulation is still too strong, the procedure can be repeated a second time with the already refined data.

In all the calculations shown above, we assumed that the relaxation of M_z is exponential. Otherwise the recovery curve would be distorted because only exponential functions are not affected in their character by a moving average.

7.2 Inversion and Saturation Recovery

7.2.1 Principle and Realization

The principle of these experiments is to invert spin magnetization or saturate a transition and read out $M_z(T)$ as a function of time T after the inversion or saturation pulse (§2.5.7). The problem of the transverse polarization detectors is that T_2 must be at least on the order of the instrumental deadtime t_d caused by the ringing of the resonator after a high-power mw pulse. This is usually the case for transition metal compounds at cryogenic temperatures and for radicals at ambient temperatures. At room temperature transition metal complexes have very short

T_2 values, which makes it difficult or even impossible to measure T_1 with these standard detection techniques. A different approach to measure $M_z(T)$ is to apply one of the polarization detectors with LOD described in chapter 5. The relaxation curve is measured in an analogous way as in an IR or SR experiment with echo detection by increasing time T between the preparation sequence and the detector step by step. The pulse scheme for the *inversion-recovery longitudinally detected T_1 experiment* (IR-LOD T_1), the progression of M_z , and the response of the detection circuit are shown in Fig. 7.1. The *saturation-recovery longitudinally detected T_1 experiment* (SR-LOD T_1) is analogous, with the inversion pulse replaced by a saturation pulse.

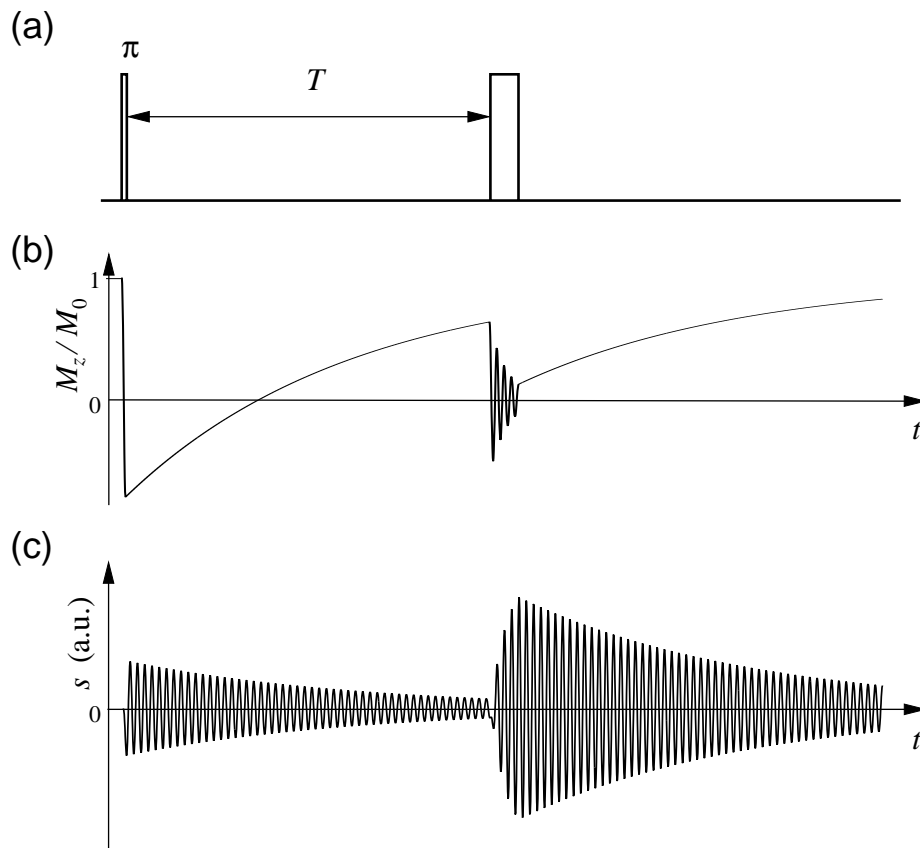


Figure 7.1: The IR-LOD T_1 experiment. (a) Pulse sequence consisting of an inverting π pulse followed by a free evolution period. At time T a nutation pulse is applied to read out $M_z(T)$. (b) Progression of M_z as a function of time t . In this simulation a ratio between the longitudinal and the transverse relaxation time of $T_1/T_2 = 25$ is used. (c) Simulated response of a serial LCR detection circuit with a quality factor $Q_{\Xi} = 100$ and $\tau_{\Xi} = T_1$.

For the two methods IR-LOD T_1 and SR-LOD T_1 , there exists a lower, but not an upper limit for T_1 . This is caused by different reasons. First, the resolution of the pulse programmer is limited. For a reasonable fit of the relaxation curve, a few data points should be collected until M_0 is reached. Second, because of the finite rise and fall time of the mw switches and the finite bandwidth $\Delta\omega$ of the mw resonator, the edges of the pulses can no longer be considered as infinitely short, whenever the switching times or $2\pi/\Delta\omega$ are not significantly shorter than T_1 . In this case the decay of the observed signal is determined by both the relaxation time T_1 and the time constant of the fall time of the preparation pulse. This effect can be reduced by using faster mw switches and by lowering the quality factor of the resonator. With our setup, T_1 values down to about 20 ns can be measured.

A signal is not only induced in the coil by the change of M_z during the detection pulse, but also during the inversion or saturation pulse (Fig. 7.1c). Since in most experiments the detection pulse is applied before the signal induced by the preparation pulse has fully decayed, the observed time trace during and after the detection pulse is a superposition of both signals. Consequently, when time T is incremented in an IR-LOD T_1 or SR-LOD T_1 experiment, the relaxation curve is modulated with ω_{Ξ} . Only in the case of $T_1 \gg \tau_{\Xi}$, no additional steps to reduce this unwanted modulation are required, because the shortest value of T can be chosen large enough so that the signal induced in the LCR circuit by the preparation pulse has decayed at the time the detection pulse is applied. The modulations can be reduced with a power cycle (§5.1.4), by calculating the moving average over a modulation period $T_{\Xi} = 2\pi/\omega_{\Xi}$ of the resonant circuit (§7.1.4), or by using an inversion sequence that consists of two pulses with the second pulse annihilating the signal induced by the first pulse. It is also possible to reduce Q_{Ξ} to get a shorter τ_{Ξ} , but this in turn reduces the sensitivity and is not a valuable alternative for short T_1 values.

The performance of these methods in an experiment is shown in Fig. 7.2 and 7.3. The effect of subtracting the blind signal is demonstrated with an SR-LOD experiment of a sample of natural dolomite where the time trace for every value of T was recorded with a transient recorder and then reduced to one point in the relaxation curve by selectively reading out the spectral component at ω_{Ξ} . Fig.

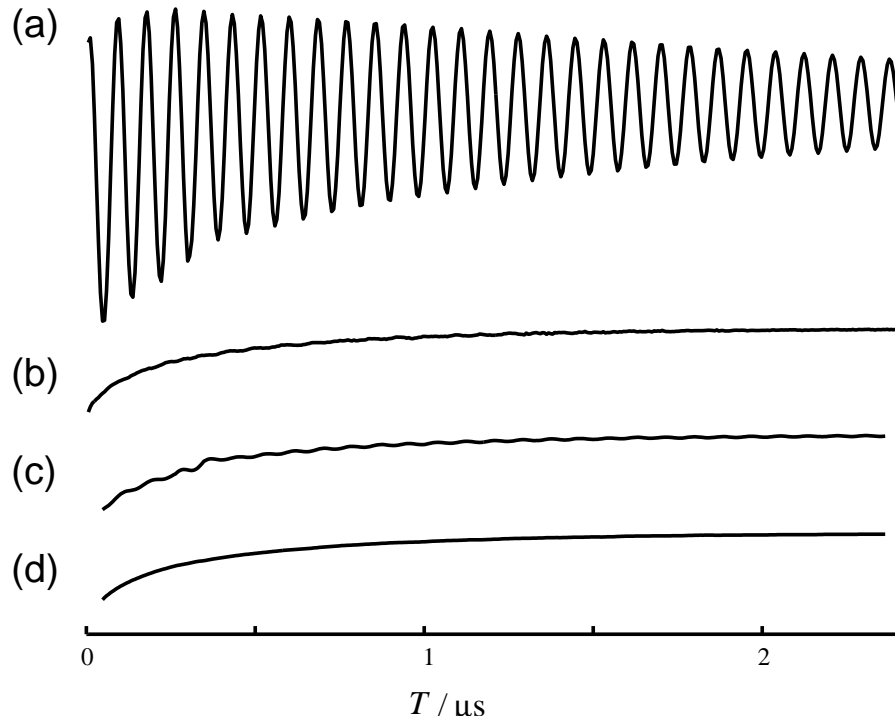


Figure 7.2: SR-LOD T_1 experiment on Mn(II) centers in natural dolomite at room temperature. (a) Initial relaxation curve after reduction of each time trace observed at a fixed T value to a single point. (b) With subtraction of blind signals. (c) With a moving average over one modulation period of the detection circuit. (d) With subtraction of the blind signals and moving average over one modulation period.

7.2a shows the original relaxation curve without any optimizations, while in Fig. 7.2b the blind signals are subtracted separately for each transient trace before they were reduced. The corrected relaxation curve is still slightly modulated. The effect of calculating a moving average over T_{Ξ} is shown in Fig. 7.2c. For short T values, instrumental artifacts are visible. Therefore even when calculating a moving average over a modulation period, a blind signal should be subtracted. The result obtained after subtraction of the blind signal and a moving average is shown in Fig. 7.2d.

The ringing of the detection circuit induced by the preparation sequence can also be minimized by inverting M_z with two mw pulses (Fig. 7.3a), where the second pulse annihilates the signal induced by the first pulse. A rule of thumb for the optimum choice of length, intensity and interpulse delay of the two pulses can-

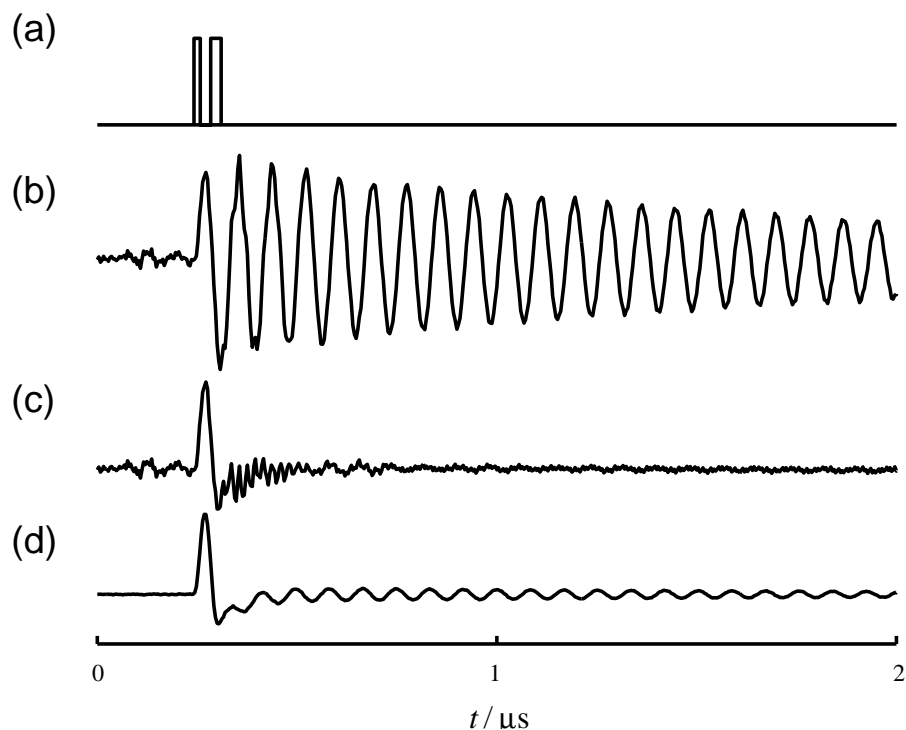


Figure 7.3: Transient signal of DPPH observed during and after the two-pulse inversion sequence. (a) Position and length of the pulses. (b) Only the first pulse was applied. (c) The second pulse is used to compensate the signal induced by the first pulse. (d) Inversion sequence with subtraction of the blind signal with fully damped mw power.

not be given, because this strongly depends on the relaxation times of the sample. The easiest way to adjust these parameters is to observe the transient signal on the oscilloscope and to optimize the different parameters iteratively. The performance of this method is shown on a sample of α,α -diphenyl- β -picrylhydrazyl (DPPH). In Fig. 7.3b, only the first pulse is applied, resulting in a modulation with a large amplitude. When the second pulse is optimized for minimum modulation at the end of the preparation sequence, the signal shown in Fig. 7.3c is obtained. The modulation of the signal after subtraction of the blind signal is stronger than the signal without this correction (Fig. 7.3d). This is because some of the artifacts, which were also reduced by the second pulse are added again by subtracting the blind signal. However, the high-frequency artifacts are strongly reduced, and the instrumental artifacts, which are clearly visible before the first pulse is applied, are completely removed.

7.2.2 Experimental Examples

A sample of γ -irradiated Herasil glass (100 kGy) was measured with the IR-LOD T_1 pulse sequence at 298 K. The length of the inverting pulse was $t_\pi = 22$ ns. To enhance the signal intensity, the magnetization was two times refocused during the detection pulse of length $2.1 \mu\text{s}$ by switching the mw phase by 180° after 420 ns and 1260 ns. The nutation frequency was adjusted to ω_Ξ . The result is shown in Fig. 7.4 together with the residues between the observed and the fitted signal. A

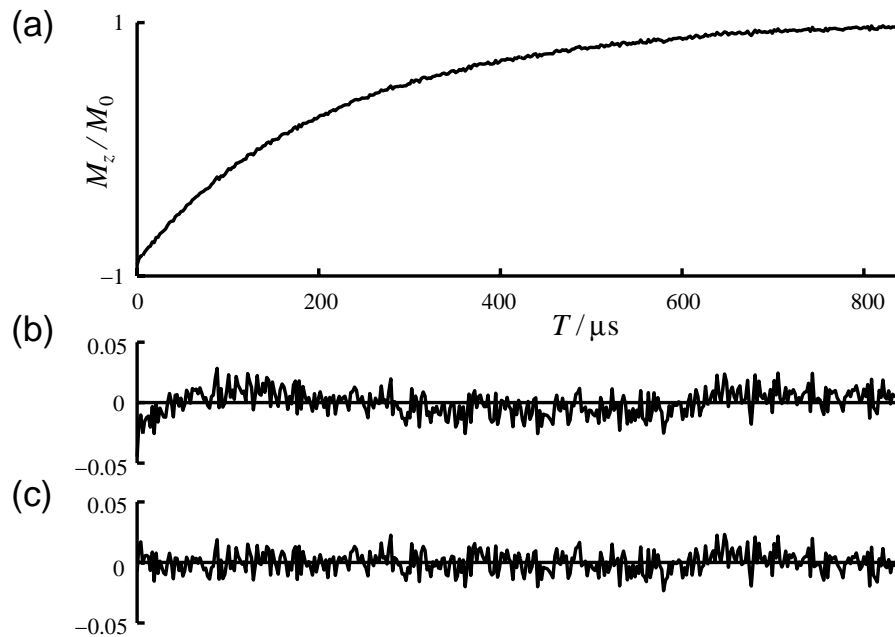


Figure 7.4: IR-LOD T_1 measurement of γ -irradiated Herasil glass at 298 K, $B_0 = 343.2$ mT and $\omega_{\text{mw}}/2\pi = 9.614$ GHz. The acquisition time was 15 min, including the measurement of the blind signal. (a) Experimental relaxation curve. (b) Residuals between the experimental relaxation curve and the fitted curve assuming an exponential recovery of M_z . (c) Residuals between the experimental relaxation curve and the fitted curve, assuming a distribution of T_1 values.

spin-lattice relaxation time of $T_1 = 219 \mu\text{s}$ was found. The same relaxation time was obtained with a standard IR experiment and two-pulse echo detection. The fit is slightly better by assuming a distribution of T_1 values (Fig. 7.4c) instead of a mono-exponential decay (Fig. 7.4b). This is reasonable because the strong γ irradiation leads to a high concentration of defect centers. Since this method is not very specific, fluctuations of local defect concentrations may occur. In addition, in

a glass the environment of the centers is not very well defined.

As a second example, the SR-LOD T_1 method was used to study a powder of natural dolomite at 250 K. In such a sample, the Ca(II) and the Mg(II) sites can be substituted by Mn(II). The length of the saturation pulse was 420 ns, the length of the detection pulse was 44 ns. The mw power was 500 W for the saturation pulse and 150 W for the detection pulse. The relaxation curve shown in Fig. 7.5 was obtained by calculating the moving average over T_{Ξ} . It can be fitted well by assuming a multi-exponential decay with two components. The longitudinal relaxation times are found to be $T_1(1) = 110$ ns and $T_1(2) = 568$ ns.

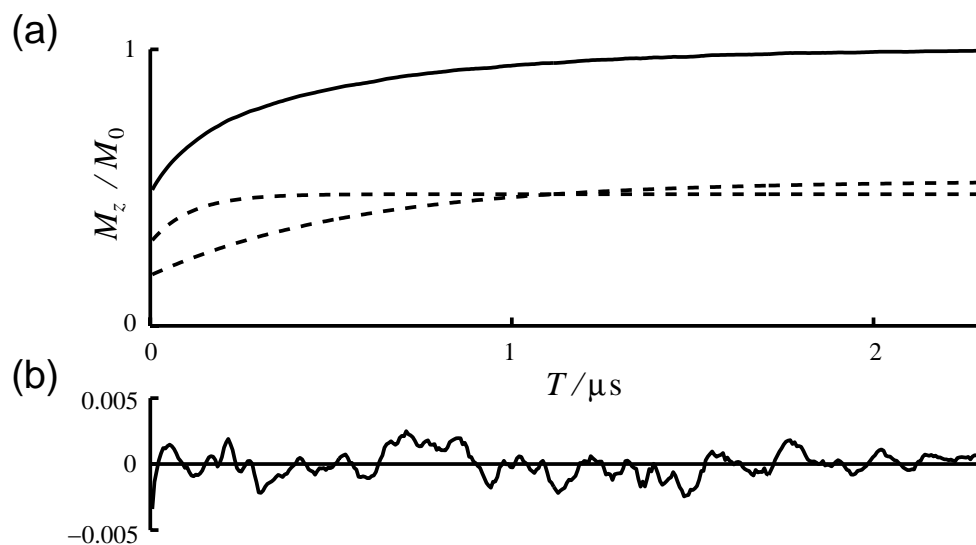


Figure 7.5: SR-LOD T_1 measurement on Mn(II) centers in natural dolomite at 250 K, $B_0 = 352.2$ mT and $\omega_{mw}/2\pi = 9.622$ GHz. 400 data points were collected. The acquisition time was 15 min, including the measurement of the blind signal. (a) *Solid line*: Experimental relaxation curve, smoothed with a moving average. *Dashed lines*: Components of the relaxation curve obtained by the fitting of the experimental data. (b) Residuals between the experimental curve and the sum of the fitted curves.

As a last example, the relaxation time T_1 of a powder of DPPH is determined with the SR-LOD T_1 method. The length of the saturation pulse was 420 ns, the length of the detection pulse was 84 ns. The mw power was 500 W for both pulses. The SR-LOD T_1 data, consisting of 100 data points separated by 10 ns in the T dimension, were acquired with a transient recorder and then processed in different ways. In Fig. 7.6a, the amplitude of the spectral component at frequency ω_{Ξ} of

the signal for each T value after the detection pulse was determined, as in the previous examples. A second approach for data analysis, shown in Fig. 7.6b, uses

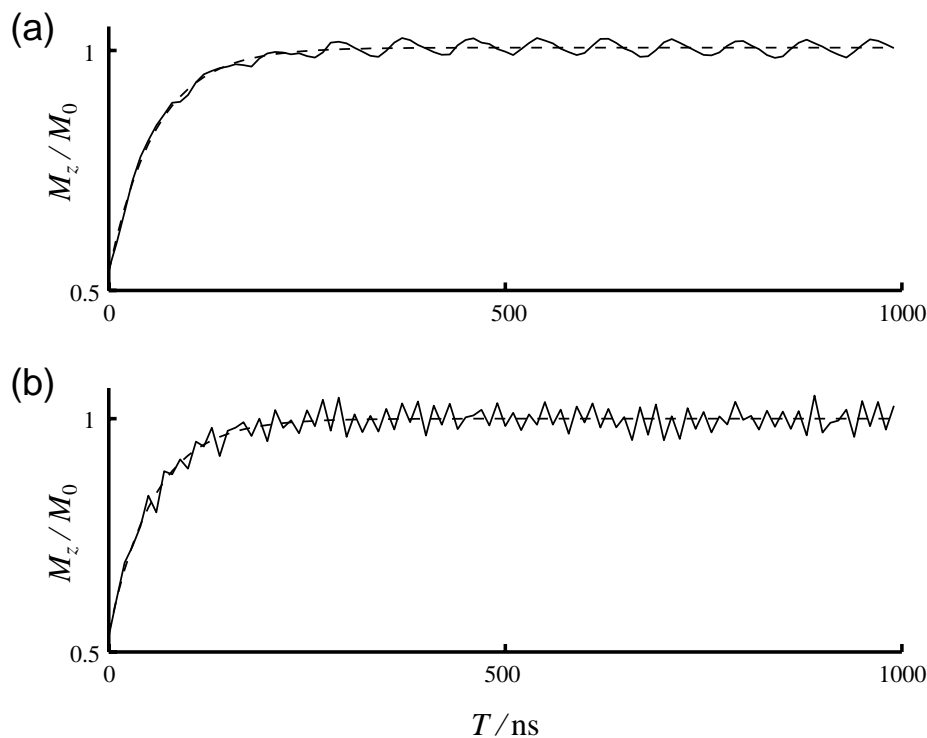


Figure 7.6: SR-LOD T_1 measurement of a powder of DPPH at 298 K, $B_0 = 343.3$ mT and $\omega_{mw}/2\pi = 9.630$ GHz. The acquisition time was 4 min, including the measurement of the blind signal. The solid lines represent the experimental relaxation curves that have not been smoothed with a moving average, the dashed lines are the corresponding fits. (a) From each trace in the t dimension the spectral component at ω_{Ξ} was calculated. (b) Only the two data points with maximum signal during the detection pulse were used.

the sum of the two data points with maximum signal during the detection pulse. A relaxation time of $T_1 = 59.2$ ns was found with the first and $T_1 = 56.7$ ns with the second analysis method.

The relaxation times of DPPH have extensively been investigated in the literature. Since T_2 is between 10^{-8} s and 10^{-7} s and very close to the T_1 value, other recording techniques perform equally well. For example, a value of $T_1 = 56$ ns was reported in [87].

7.3 Direct Measurement of T_1

An alternative way of measuring T_1 is to analyze the broadband signal that is induced after the preparation sequence by the temporal derivative of the relaxing M_z magnetization. In analogy to the IR-LOD T_1 and SR-LOD T_1 experiments, an exponentially damped modulation with frequency ω_{Ξ} and time constant τ_{Ξ} originating from the ringing of the detection circuit is superimposed on the relaxation curve. This time, only the instrumental artifacts can be removed by subtracting the blind signal which can be recorded either with a B_0 field far off-resonance or by reducing the mw power. To reduce the oscillations superimposed on the relaxation curve, we have to calculate the moving average over T_{Ξ} as explained in the previous section. As a consequence, this method is only feasible for an exponentially relaxing magnetization. An alternative to the calculation of the moving average is to perform the experiment with a resonant circuit with a very low Q_{Ξ} value so that after excitation the ringing of the detection circuit decays rapidly ([34] and P. Höfer, pers. commun.).

With this direct method, T_1 can be determined in a single experiment so that the recording time is strongly reduced compared to an IR-LOD T_1 or SR-LOD T_1 experiment. Furthermore, it is possible to carry out a 2D field-swept EPR experiment with T_1 as a second dimension. The lower limit for T_1 is about 20 ns for the same reasons as discussed above for the IR-LOD T_1 and SR-LOD T_1 experiments. Another reason is the bandwidth limitation of the voltage follower, which is approximately 100 MHz. Since for this experiment the induced voltage is proportional to $dM_z(t)/dt$, the signal intensity scales with $1/T_1$, which becomes evident by calculating the first derivative of Eq. (2.32). Therefore this method is mainly suited for short T_1 values. If the baseline is corrected accurately, the signal can be integrated to obtain $M_z(t)$, but the risk to introduce systematic errors is relatively high. With samples that are affected by any kind of diffusion, an analysis of this kind leads to different results than a method where only the on-resonant M_z magnetization is read out with a detection pulse.

As an example for this method, the same data of DPPH than in the last section was interpreted and analyzed differently. The mechanism described here induces

a signal in the transient trace of an SR-LOD T_1 as well, but in that experiment it is neglected and the information gets lost during the data analysis. As can be seen in Fig. 7.6, M_z has fully relaxed for $T > 400$ ns. the signal induced by the detection pulse does not depend on the preparation pulse anymore. Therefore for any of these traces the same result is expected in a direct measurement of T_1 when only the signal after the detection pulse is considered. To increase the signal-to-noise ratio, the 50 traces with $T > 500$ ns were added (Fig. 7.7a). To get

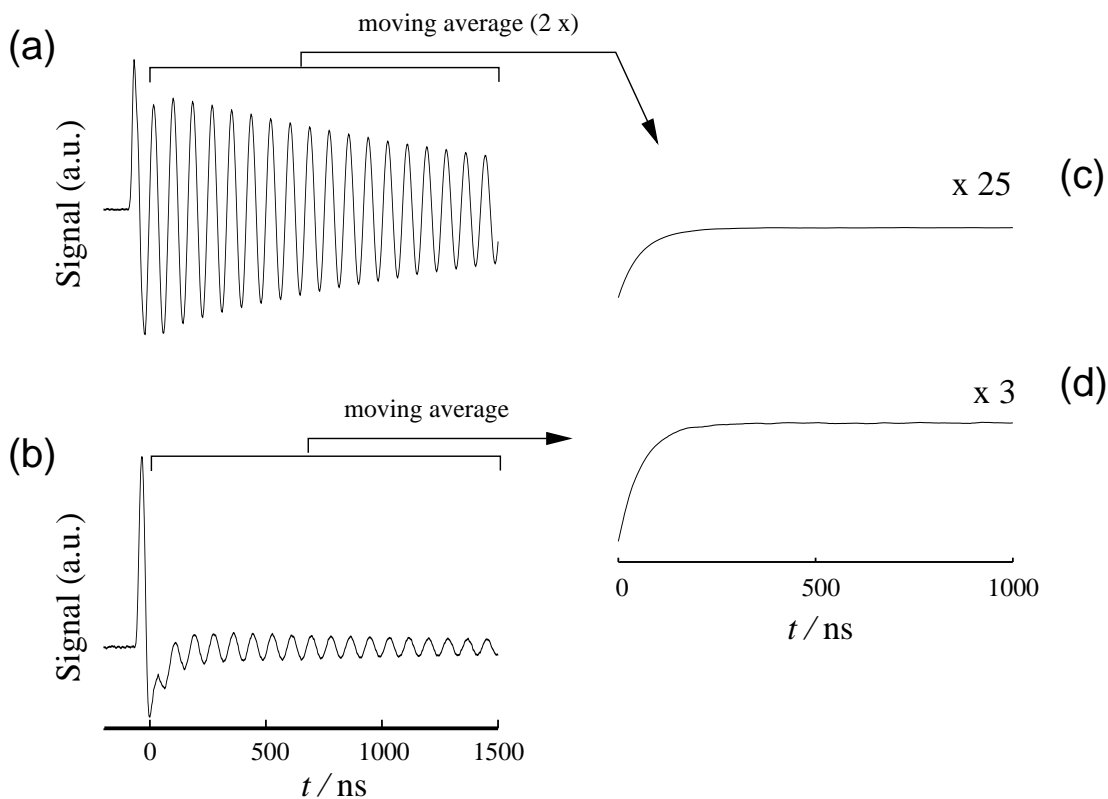


Figure 7.7: Measurement of T_1 using the signal that is directly induced by the relaxing M_z magnetization after an excitation. (a) The same data set as in Fig. 7.6 was used to determine the induced signal. (b) Signal induced by a two-pulse inversion sequence. (c) Signal of (a) after smoothing with two consecutive moving averages over T_E . (d) Signal of (b) smoothed with one moving average over T_E .

rid of the modulations, two consecutive moving averages over T_E were calculated before T_1 was determined. The result is shown in Fig. 7.7c. The relaxation time found with this method was $T_1 = 57.9$ ns. The same analysis was done with the time trace obtained after an inversion pulse sequence consisting of two pulses

to minimize the resonator ringing (Fig. 7.3 and 7.7c), where it was sufficient to eliminate the modulations with a single moving average over T_{Ξ} , shown in Fig. 7.7d. $T_1 = 57.2$ ns was obtained in this case.

It should be noted that although the same data set was used for the analysis in Fig. 7.6 and Fig. 7.7a, the mechanisms that induce the signal were different. Additionally, Fig. 7.6 is an SR experiment, while Fig. 7.7 shows IR experiments with two different data sets. Therefore these second results can be used to verify the results obtained with the first scheme.

Chapter 8

Outlook

8.1 Instrumentation

Since this work is based on a new instrumental approach and not on an optimization of a previous setup, there are several possibilities for future developments. As was shown in this study for the X-band, the requirements for a pulse ENDOR and a pulse LOD probehead are similar. Maybe this can be used to build probeheads suited for both tasks also at other frequency bands.

In LOD experiments, the excitation frequency is usually at least three orders of magnitude higher than the detection frequency. Therefore the excitation and the detection channels are only coupled with each other through the spin system. For low temperature measurements, a setup where the whole detection circuit, the impedance matching device and the preamplifier are at low temperature would fully benefit from the improved noise figure of the corresponding devices. However, this would require a completely new probehead, which would not be suited for pulse ENDOR experiments anymore. At least, pulse and cw EPR experiments with only mw excitation and transverse detection should still be possible, so that the same sample could be investigated with LOD as well as with transverse detection without changing the setup.

As was mentioned in the instrumental chapter, one of the main factors influencing the sensitivity of the setup is the design of the detection circuit. To predict the success of the different optimization parameters, we can start from the formula

of the signal-to-noise ratio in a cw LOD EPR experiment and summarize only the detector dependent part ψ_{Ξ} of Eq. (4.10). By neglecting constant factors, we get

$$\psi_{\Xi} \propto \sqrt{\frac{V_C Q_{\Xi} \omega_{\Xi}}{T \Delta \nu F}} \eta_C. \quad (8.1)$$

The coil volume V_C and its filling factor η_C are already well optimized in the current setup. Possible improvements include changing the number of turns of the detection coil or the capacitance C of the detection circuit. To estimate the influence of such changes, we can assume that η_C , V_C , T , $\Delta \nu$ and F are constant, and we get the simplified equation

$$\psi_{\Xi} \propto \sqrt{Q_{\Xi} \omega_{\Xi}} = \frac{1}{\sqrt{R_S C}}. \quad (8.2)$$

Now two different cases can be distinguished. One is to keep ω_{Ξ} constant, the other one is to improve ψ_{Ξ} irrespective of the change of ω_{Ξ} . The important formulae for this discussion are given in Appendix C. The inductance of the coil is given as

$$L = \frac{\mu_0 n^2 A^2}{V_C}, \quad (8.3)$$

where the cross-section A shall be constant. The main contribution to the serial resistance R_S of the detection circuit comes from the coil and is given as

$$R_S = \rho \frac{l}{A_w}, \quad (8.4)$$

where l is the length of the wire used for the coil, A_w is its cross-sectional area, and ρ is its specific resistance. Since l is approximately proportional to n , we can say that

$$R_S \propto \frac{n}{A_w}. \quad (8.5)$$

Assuming ω_{Ξ} to be constant is equivalent to

$$LC = \text{const.}, \quad (8.6)$$

since $\omega_{\Xi} = (LC)^{-1/2}$ in a serial LCR circuit. Increasing n by a factor f also increases R_S by the same factor, and we have to decrease C by a factor f^2 . We get

for the signal-to-noise ratio

$$\psi_{\Xi}(1) \propto \frac{1}{\sqrt{R_S(1)C(1)}} = \sqrt{\frac{f}{R_S(0)C(0)}}. \quad (8.7)$$

To double ψ_{Ξ} we have to increase n by a factor 4. However, increasing n is usually possible only within certain limits without decreasing A_w , which leads to an increased R_S . If we assume that the wire is chosen such that it fills the available space completely, we have to reduce A_w approximately by a factor f to increase n by a factor f . This increases the resistance of the wire by a factor f , and we do not get a benefit for ψ_{Ξ} at all. An alternative to circumvent the problems associated with the serial resistance of the wire for the detection coil is to use a superconductive coil. In this case, ψ_{Ξ} increases, but the setup complicates considerably and loses some of its versatility.

Another possibility to optimize ψ_{Ξ} in Eq. (8.2) is to decrease C by a factor f without changing the coil. This leads to an increase of ψ_{Ξ} by a factor \sqrt{f} , and it also increases ω_{Ξ} by the same factor. In the setup used in this work, reducing C is possible if one can modify the probehead, since the main contribution to C originates from the semi-rigid cable between the coil and the rf connectors.

A problem with the present setup was noise of instrumental origin. To a certain extent, it can be removed by subtracting a blind signal. But it prevented to fully benefit from the increased Q_{Ξ} caused by the reduced R_S at very low temperatures, because it was necessary to introduce a resistance at temperatures below 100 K to avoid that Q_{Ξ} gets larger than about 150. At higher Q_{Ξ} , the voltage follower was overloaded by the signal that the detection circuit picked up from the console and the mw bridge. Therefore, an improved setup should have a better rf shielding.

Another future development could be to simplify the access to LOD methods and equipment for other researchers. This could include a ready-to-use device with all the electronic parts, which are necessary in addition to the ones available in a standard spectrometer, or predefined pulse programs and data analysis tools that can be used without an extensive study of the topic.

Since the properties of EPR methods with LOD are strongly dependent on the relaxation times of a sample, an important step towards a more general usability

of LOD would be to construct a setup with an easily changeable detection frequency, for example by including a device to switch between different C , possibly combined with a tunable capacitor to enable a continuous variation of ω_{Ξ} .

And finally, setups might be designed that do not use coils for detection, but more sensitive sensors like optical devices or spin systems that can be read out very sensitively.

8.2 CW LOD EPR

Based on the theoretical approach presented in chapter 3, it should be possible to do relaxation time studies by analyzing the phase of the signal. Similar approaches have been made by other groups and were described in the same chapter. However, all of them are based either on the variation of an additional parameter like the modulation frequency, or the recording of the longitudinal and the transverse component of the signal separately. A new approach could be to use the difference of the signal phase between on- and off-resonant mw irradiation. But even in this case, a careful calibration of the phase of the signal, possibly with a well-known reference, is necessary. First experiments were made with the Mn(II)-doped NH_4Cl sample presented in chapter 6. A clear projection of the EPR spectrum was visible also in the phase spectrum. But since this sample has $S = 5/2$ and a large zero-field splitting, Eq. (3.46) might be inadequate for a detailed analysis.

In almost all theoretical approaches to describe LOD experiments with continuous amplitude modulated mw irradiation, an $S = 1/2$ spin system and the validity of the Bloch equation was assumed. This is a good starting point to get an understanding of the method, but it is an oversimplification for most samples that are investigated with EPR. It neglects, for example, cross relaxation, the influence of diffusion processes, the anisotropy or transition dependence of relaxation times, or the different behaviour upon mw irradiation of central and non-central transitions in a spin system with $S > 1/2$. Future developments in cw LOD EPR should extend the theoretical background to include at least some of the effects listed above. Possible applications from such an extended treatment could include

new methods for sensitivity enhancement, for example by measuring the signal in a second dimension as a function of the mw power, or by detecting at different harmonics of the amplitude modulation frequency and compare the obtained spectra. An enhanced sensitivity might also be obtained by a variation of the shape of the amplitude modulation, which is possible with the setup presented in chapter 4.

8.3 Pulse LOD EPR

Pulse LOD has a large potential for future improvements. First of all, because LOD is sensitive directly to the change of longitudinal magnetization, it is superior to transverse techniques to study longitudinal relaxation phenomena as soon as a sensitive setup is available. In this thesis only some very basic methods have been presented to investigate relaxation phenomena, and the possibility to study diffusion phenomena was only sketched. A next step could be for example to perform ELDOR type experiments with LOD. Another possibility would be to perform 2D field-swept EPR experiments with T_1 as a second dimension. This kind of experiment fully benefits from the properties of pulse LOD, which allows to resolve T_1 down to 10^{-8} s, and for the first time it becomes possible to do such experiments with liquid samples.

Many of the conventional pulse EPR schemes can be used with LOD without substantial changes except for the detection sequence. Experiments where $M_z(t)$ is the property of interest are simplified with LOD, since no coherence must be created to obtain a signal. But experiments where an echo modulation is investigated have to be supplemented by an additional detection pulse at the position of the echo that induces a changing M_z magnetization proportional to the echo intensity. A very challenging task, theoretically and especially instrumentally, would be to invent pulse experiments where the desired information, for example of an ESEEM experiment, is directly encoded in a modulation of M_z and broadband detected.

In chapter 6 it is shown how a nutation pulse can be used to induce a signal in a pick-up coil parallel to \mathbf{B}_0 . However, the attempt was not made to separate a spectrum with respect to its nutation frequency. A possible experiment would be

a 2D transient nutation experiment with B_0 changed in the first and B_1 changed in the second dimension. If the condition $\omega_{\text{eff}} = \omega_{\Xi}$ is fulfilled for a certain transition, the spectrum would show a maximum signal, and a PEANUT-type result would be obtained.

Significant improvements should also be possible with an optimization of the data analysis. One possibility is to simulate the full time trace of an observed signal, including the properties of the detection circuit. Especially for samples with T_1 on the order of $1/\omega_{\Xi}$ or shorter, this could improve the quality of the obtained results considerably. But such simulations are rather complicated, and a large number of parameters must be taken into account. Another extension of existing analysis schemes would be to consider the exponentially damped modulation, which is still present after a B_1 cycle, in the data analysis instead of ignoring it or trying to remove it.

Appendix A

Forced Harmonic Oscillation of a Serial LCR Circuit

The equation of motion of a forced harmonic oscillation is given by

$$\frac{1}{\omega_{\Xi}^2} \frac{d^2}{dt^2} V_{\Xi}(t) + \frac{1}{Q_{\Xi} \omega_{\Xi}} \frac{d}{dt} V_{\Xi}(t) + V_{\Xi}(t) = V_0 \cos(\omega t), \quad (\text{A.1})$$

with the quality factor Q_{Ξ} , the excitation $V(t) = V_0 \cos(\omega t)$ of the forced oscillation, and the voltage $V_{\Xi}(t)$ on the capacitor. The detection circuit is undercritically damped, *i.e.* $2Q_{\Xi} = \omega_{\Xi} \tau_{\Xi} > 1$. The forced oscillation, which is switched on at $t = 0$, consists of two components, the rise oscillation $V_{\Xi,r}(t)$ and the stationary oscillation $V_{\Xi,s}(t)$ with

$$V_{\Xi}(t) = V_{\Xi,r}(t) + V_{\Xi,s}(t). \quad (\text{A.2})$$

$V_{\Xi,r}(t)$ is the general solution of the homogeneous equation of motion, $V_0 = 0$, that depends on the initial conditions and is decreasing with time. $V_{\Xi,s}(t)$ is the periodic solution of the inhomogeneous equation of motion, $V_0 \neq 0$, and is independent of the initial conditions. The rise of an undercritically damped resonant circuit corresponds to a damped oscillation,

$$V_{\Xi,r}(t) = V_{\Xi,0} \exp\left(-\frac{t}{\tau_{\Xi}}\right) \cos(\omega_D t - \alpha_0), \quad (\text{A.3})$$

with $\omega_D = \omega_{\Xi} \sqrt{1 - (2Q_{\Xi})^{-2}}$. The amplitude $V_{\Xi,0}$ and the phase α_0 depend on the initial conditions of the forced oscillation, *e.g.* $V_{\Xi}(0)$ and $\dot{V}_{\Xi}(0)$. The stationary oscillation $V_{\Xi,s}(t)$ is a harmonic oscillation

$$V_{\Xi,s}(t) = V_{\Xi,s}(\omega) \cos(\omega t - \alpha(\omega)) \quad (\text{A.4})$$

with the angular frequency ω of the excitation. Amplitude $V_{\Xi,s}(\omega)$ and phase $\alpha(\omega)$ depend on ω and V_0 , but not on the initial conditions of the resonant circuit. We obtain

$$V_{\Xi,s}(\omega) = V_0 \frac{1}{\sqrt{\left[1 - \left(\frac{\omega}{\omega_{\Xi}}\right)^2\right]^2 + \left[\frac{\omega}{Q_{\Xi}\omega_{\Xi}}\right]^2}} \quad (\text{A.5})$$

for the amplitude and

$$\tan(\alpha(\omega)) = \frac{1}{Q_{\Xi}} \frac{\omega \omega_{\Xi}}{\omega_{\Xi}^2 - \omega^2} \quad (\text{A.6})$$

for the phase of the signal. In complex notation, the amplitude of the stationary oscillation is

$$V_{\Xi,s}(\omega) = V_0 \frac{1}{1 - \left(\frac{\omega}{\omega_{\Xi}}\right)^2 + i \frac{\omega}{Q_{\Xi}\omega_{\Xi}}} . \quad (\text{A.7})$$

A maximum amplitude $V_{\Xi,s}(\omega_{\text{res}}) = V_{\Xi,\text{max}}$ of the stationary forced oscillation is obtained at angular frequency $\omega = \omega_{\text{res}}$ of the excitation. We get

$$\omega_{\text{res}} = \omega_{\Xi} \sqrt{1 - \frac{1}{2Q_{\Xi}^2}} , \quad (\text{A.8})$$

$$V_{\Xi,\text{max}} = V_0 Q_{\Xi} \sqrt{1 - \frac{1}{4Q_{\Xi}^2}} , \quad (\text{A.9})$$

$$\tan(\alpha_{\text{res}}) = 2Q_{\Xi} \sqrt{1 - \frac{1}{2Q_{\Xi}^2}} . \quad (\text{A.10})$$

With our setup, the important case is $Q_{\Xi} \gg 1$, and we get

$$\omega_{\text{res}} \approx \omega_{\Xi}, \quad (\text{A.11})$$

$$V_{\Xi, \text{max}} \approx V_0 Q_{\Xi}, \quad (\text{A.12})$$

$$\tan(\alpha_{\text{res}}) \approx 2Q_{\Xi}. \quad (\text{A.13})$$

Therefore the distinction between ω_{res} and ω_{Ξ} will not be made in the instrumental and the experimental chapters.

The half width of a resonance is the interval $\Delta\omega$ between the two exciting angular frequencies for which the energy of the forced harmonic oscillation is half of the resonance energy at ω_{res} . For $Q \gg 1$, we get

$$\frac{\Delta\omega}{\omega_{\Xi}} = \frac{1}{Q_{\Xi}}. \quad (\text{A.14})$$

Appendix B

B_1 Field Distribution in a Dielectric Ring Resonator

If a quantity x in a Hamiltonian has not an exact value for all spin packets, but is described with a distribution, it is in most cases necessary to evaluate the Hamiltonian for different values of x and perform a weighted summation. The weight function $w(x)$ can be defined infinitesimally as

$$dw(x) = p(x) dx, \quad (\text{B.1})$$

with the probability distribution $p(x)$ of this particular state, which is proportional to the number of spin packets with the corresponding Hamiltonian. In a simulation, only a discrete number of calculations with different x values can be evaluated. Thus, the x axis has to be split into different segments, subdivided by a number of anchor points x_i . For each of these segments, the Hamiltonian is evaluated once at a value x_j between x_i and x_{i+1} and weighted with

$$w(x_j) = \int_{x_i}^{x_{i+1}} p(x) dx. \quad (\text{B.2})$$

Rules how the values x_i and x_j should be chosen to get an optimum compromise between performance and accuracy can be found in textbooks on numerical analysis, *e.g.* [84].

Very important for EPR experiments is the distribution of B_1 over the sample volume. For a dielectric ring resonator it has been determined both numerically (J. Forrer, private communication) and experimentally [76], and this discussion is based on data available from these sources¹. The lateral B_1 value, *i.e.* perpendicular to the resonator axis, falls off by less than 5 % to the edge of the sample and has to be considered only with disk shaped samples. In this discussion, it is neglected, because the axial distribution is much broader. Parallel to the resonator axis, B_1 has a -5 % homogeneity region that covers approximately 25 % of the resonator height, rapidly falling off to about 50 % of the maximum value at the edges of the resonator. These values can be fitted nicely with a Gaussian function

$$B_1(h') = B_{1,\max} \exp\left(-\frac{1}{2} \left(\frac{h' - h_0}{k}\right)^2\right), \quad (\text{B.3})$$

where h' is the position of a particular sample fraction along the resonator axis. h_0 corresponds to the position with maximum B_1 field, and k is a parameter characterizing the width of the B_1 distribution² and is a constant for a certain resonator. To keep the formulae simple, we will substitute $h = h' - h_0$. Note that the use of a Gaussian function for the B_1 field distribution is an *ad hoc* assumption. The values of B_1 within the resonator can be reproduced nicely, and also the behaviour on its outside is consistent with numerical simulations. However, the measured values inside the resonator can be modeled with a hyperbolic function equally well within the error limits of the measurements, and also a parabolic function would be suited. This last possibility is used in §4.4.2 to derive an analytic expression for the nutation of an $S = 1/2$ spin system with on-resonant mw irradiation and a distribution of B_1 . In Fig. B.1, numerical values are shown for the Bruker X-band pulse and cw EPR probehead ER-4118, where the nutation frequency $\nu_{\text{TN}} = \omega_{\text{eff}}/2\pi$ was determined with a phase-inverted echo-amplitude detected nutation (PEANUT)

¹The same numerical [88, 89] and experimental [76] data is available for the bridged loop-gap resonator, where the B_1 field drops off fast at the upper and lower edge of the resonator. The -5 % homogeneity region covers 50 % of the resonator length, but the length of the resonator is only about 8 mm compared to 13 mm of a dielectric ring resonator for X-band frequencies.

²To be precise, $2k$ is the width between the two points with maximum slope of the Gaussian function.

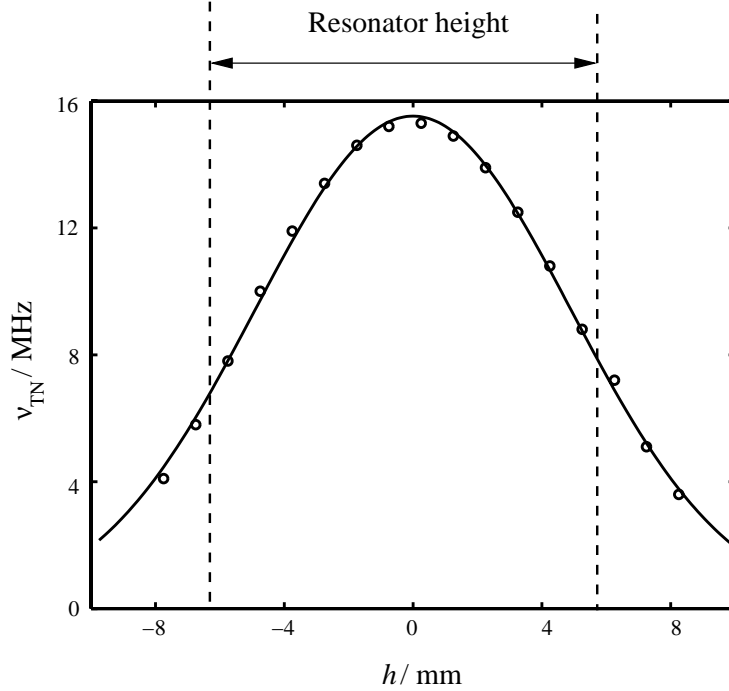


Figure B.1: Distribution of ν_{TN} in the Bruker X-band probehead ER-4118 with a dielectric resonator. (circles) Experimental values as published in [25], which have been determined with a PEANUT experiment using a small sample of lithium phtalocyanine. (solid line) Fit of a Gaussian function to the experimental data using a least-square algorithm. A value of $k = 4.9$ mm according to the definition in Eq. (B.3) was obtained.

experiment [25, 76] using a small sample of Lithium Phtalocyanine that has been measured at different heights. For such a simple $S = 1/2$ system³, B_1 is proportional to ν_{TN} . While B_1 is more convenient as a measure for a weight function because its amplitude mainly depends on instrumental factors and does not depend on sample properties, ν_{TN} is easier to measure with high precision. Fortunately, as we will see later, B_1 appears in the formula for the weight function only relative to its maximum value $B_{1,\text{max}}$, thus the same distribution is obtained with B_1 and ν_{TN} . The next step is to calculate $p(B_1)$, *i.e.* the fraction of sample as a function of B_1 . First, Eq. (B.3) can be transformed to

$$h(B_1) = k \sqrt{2 \ln(B_{1,\text{max}}/B_1)}. \quad (\text{B.4})$$

³This is strictly valid only for an isotropic $S = 1/2$ system. For systems with $S > 1/2$ or anisotropic g values, the situation is more complicated [24, 25].

We assume that in the sample holder every slice with the infinitesimal height dh contains the same amount of sample, which is true, for example, for a cylindrical sample as is used in most measurements of diluted powders or frozen solutions. Now we can say that the larger the volume element with a certain B_1 value, the larger is the derivative $dh(B_1)/dB_1$. Thus the – not normalized – probability to find a spin packet at a certain value of B_1 is given by

$$\tilde{p}(B_1) = \frac{dh(B_1)}{dB_1} = -\frac{k}{B_1 \sqrt{2 \ln(B_{1,\max}/B_1)}}. \quad (\text{B.5})$$

If we additionally assume that the sample is loaded symmetrical⁴ with respect to h_0 , a normalized probability distribution $p(B_1)$, where $\int p(B_1)dB_1 = 1$, can be obtained through dividing $\tilde{p}(B_1)$ by its integral from $B_{1,\min}$ to $B_{1,\max}$. A simple term is obtained if $B_{1,\min}$ is expressed as a fraction of $B_{1,\max}$, namely $B_{1,\min} = B_{1,\max}/d$. Integration yields

$$P = \int_{B_{1,\max}/d}^{B_{1,\max}} \tilde{p}(B_1) dB_1 = -k \sqrt{2 \ln(d)}. \quad (\text{B.6})$$

This result shows that assuming a Gaussian distribution of B_1 is not sensible anymore for a very long sample with $B_{1,\min} = 0$, because then P goes to infinity. But such a long sample physically does not make sense either. For the normalized probability distribution we get

$$p(B_1) = \frac{\tilde{p}(B_1)}{P} = \frac{1}{2 \sqrt{\ln(d)} B_1 \sqrt{\ln(B_{1,\max}/B_1)}}. \quad (\text{B.7})$$

Eq. (B.7) goes to infinity at $B_1 = B_{1,\max}$. But in a numerical simulation with a discrete number of Hamiltonians at different values of B_1 we need the weight function $w(B_1)$ rather than $p(B_1)$, which is now

$$w(B_{1,j}) = \int_{B_{1,i}}^{B_{1,i+1}} p(B_1) dB_1 = \frac{\sqrt{\ln\left(\frac{B_{1,\max}}{B_{1,i}}\right)} - \sqrt{\ln\left(\frac{B_{1,\max}}{B_{1,i+1}}\right)}}{\sqrt{\ln(d)}}, \quad (\text{B.8})$$

⁴This assumption simplifies normalization of $\tilde{p}(B_1)$ somewhat, but is not a necessary requirement.

where i and j have the same meaning as in the general considerations above. To get the correct sign, one must keep in mind that we derived these equations by integrating from $h = 0$. Therefore $B_{1,i} > B_{1,i+1}$. Eq. (B.7) does not depend explicitly on k . The only parameter that one needs to know in a simulation of a B_1 distribution is the upper and the lower bound of B_1 . k is implicitly enclosed in $B_{1,\min}$. This can be used, on the other hand, to determine $B_{1,\min}$ if the sample size and $B_{1,\max}$ is known.

Appendix C

Signal-to-Noise Ratio of CW LOD EPR

The discussion is divided into three parts. Because the coupling between the excitation and the detection circuit is only done by the spin system, we can completely separate the time evolution of M_z , which is induced by irradiating the spin system with an mw field, and the signal induced in the detection circuit by $M_z(t)$. As a measure for the sensitivity, we use the S/N ratio of our setup and the corresponding minimum detectable number of spins. Therefore we will treat the noise on the detector as third part. It would be possible as well to consider only the induced signal, but this treatment might be misleading by giving an ambiguous weighting of certain parameters which are relevant for the noise as well.

C.1 Time Evolution of M_z

As is shown in §C.2, the induced signal is proportional to $-dM_z/dt$. This means that an mw irradiation scheme has to be chosen to optimize this signal. For this discussion, a continuous mw field \tilde{B}_1 linearly polarized along the x axis of the laboratory frame whose amplitude is modulated with the resonant frequency ω_{Ξ} of the detection circuit is assumed. It has the form

$$\tilde{B}_1(t) = 0.5 (1 + \cos(\omega_{\Xi}t)) B_1 . \quad (\text{C.1})$$

$M_z(t)$ can be calculated using the Bloch equations (2.33). It is a simple task for constant mw irradiation to calculate a steady-state solution (Eq. 2.38), but with

amplitude modulation, it can be very difficult or even impossible to find analytical solutions, depending on $B_1(t)$. For a straightforward discussion, we assume a homogeneous EPR line and $\Omega_S = 0$. Because we are interested in the S/N ratio, this is justified because we get the maximum signal at this position. To simplify the discussion further, let us assume that

$$T_1 < \omega_{\Xi}^{-1}. \quad (\text{C.2})$$

In this way we can approximate $M_z(t)$ by its respective steady-state solution during the experiment, phase-shifted by a certain angle φ . At this point we are not interested in this phase and neglect it. By inserting $\tilde{B}_1(t)$ into Eq. (2.38), we get

$$\begin{aligned} M_z(t) &\approx \frac{M_0}{1 + \left(\frac{g\beta_e}{2\hbar} (1 + \cos(\omega_{\Xi}t)) B_1 \right)^2 T_1 T_2} \\ &= \frac{M_0}{1 + 0.25 (1 + \cos(\omega_{\Xi}t))^2 \omega_1^2 T_1 T_2} \end{aligned} \quad (\text{C.3})$$

with the amplitude of the spin magnetization M_0 at Boltzmann equilibrium. The time derivative of $-M_z(t)$ can be calculated as

$$\begin{aligned} -\frac{dM_z(t)}{dt} &= \frac{0.25(\omega_1)_0^2 T_1 T_2 (1 + \cos(\omega_{\Xi}t)) \sin(\omega_{\Xi}t) \omega_{\Xi}}{(1 + 0.25 (1 + \cos(\omega_{\Xi}t))^2 (\omega_1)_0^2 T_1 T_2)^2} M_0 \\ &= 0.25 \omega_{\Xi} a_0 M_0 \frac{\sin(\omega_{\Xi}t) + 0.5 \sin(2\omega_{\Xi}t)}{(1 + 0.25 a_0 (1 + \cos(\omega_{\Xi}t))^2)^2}, \end{aligned} \quad (\text{C.4})$$

where $a_0 = \omega_1^2 T_1 T_2$ is the saturation factor at maximum mw power. If we do not saturate the EPR transition, *i.e.* $a_0 \ll 1$, we can set

$$(1 + 0.25 a_0 (1 + \cos(\omega_{\Xi}t))^2)^2 \approx 1, \quad (\text{C.5})$$

and we get

$$-\frac{dM_z(t)}{dt} \approx 0.25 \omega_{\Xi} a_0 M_0 (\sin(\omega_{\Xi}t) + 0.5 \sin(2\omega_{\Xi}t)). \quad (\text{C.6})$$

This shows that we observe a signal not only at the modulation frequency ω_{Ξ} , but also an appreciable signal amplitude at its first harmonic, and we could use this frequency for detection as well. But here we use ω_{Ξ} as the reference for the PSD, and therefore the relevant signal component is

$$-\frac{dM_z(t)}{dt} = 0.25 \omega_{\Xi} a_0 M_0 \sin(\omega_{\Xi} t). \quad (\text{C.7})$$

C.2 Signal Induced by a Magnetization Changing in Time

The magnetic field of a magnetic dipole with the moment $\boldsymbol{\mu}$, described by its magnetic induction \mathbf{B} , is given in vacuum by

$$\mathbf{B}(\mathbf{r}) = \frac{\mu_0}{4\pi} \frac{3(\boldsymbol{\mu} \cdot \mathbf{r})\mathbf{r} - (\mathbf{r} \cdot \mathbf{r})\boldsymbol{\mu}}{r^5}, \quad (\text{C.8})$$

where the vector \mathbf{r} has its origin at the magnetic dipole. If \mathbf{B} flows through a closed loop s , the magnetic flux Φ is defined as

$$\Phi = \int_A \mathbf{B} \cdot \mathbf{n} da \quad (\text{C.9})$$

where A is the area delimited by s and \mathbf{n} is a normalized vector orthogonal to the infinitesimal area element da . Φ is independent of the choice of A . Φ changing in time induces between the two ends of a wire loop an electric voltage

$$V_{\text{ind}} = -\frac{d\Phi(t)}{dt}. \quad (\text{C.10})$$

In an LOD setup, the detection device is an rf coil integrated into a serial LCR resonant circuit with the self-inductance L of the coil, the capacitance C of a condenser, and the resistance R_S of the coil as the main contribution to the total serial resistance. The resonance condition of such an LCR circuit with resonant frequency ω_{Ξ} is given by

$$\omega_{\Xi}^2 LC = 1, \quad (\text{C.11})$$

and its quality factor is

$$Q_{\Xi} = L \omega_{\Xi} / R_S. \quad (\text{C.12})$$

To calculate the induced signal, some idealized assumptions are made, identical to the ones made by ABRAGAM [20] in his discussion of the sensitivity of an NMR setup. The self-induction of the detection coil shall be given by the formula

$$L = \frac{\mu_0 n^2 A^2}{V_C}, \quad (\text{C.13})$$

which is correct for a long solenoid. n is the number of turns of the coil, A is the coil area, and V_C is the coil volume. We assume for simplicity that a magnetic induction \mathbf{B} produced by a current I is uniform inside and vanishes outside the coil. An electromagnetic force \mathcal{E} of frequency ω_Ξ induced in the coil will result in a voltage

$$S = Q_\Xi \mathcal{E} \quad (\text{C.14})$$

across its terminals. If the coil axis is along the z direction, we can assume that

$$\Phi = \frac{\mu_0 A \mu_z(t)}{V_C} \quad (\text{C.15})$$

for a single magnetic dipole with $\mu_z(t) = \mu \cos(\omega_\Xi t)$. If we have a macroscopic magnetization \mathbf{M} , described by Eq. (2.12), \mathcal{E} is given by the Faraday law

$$\mathcal{E} = -\frac{\mu_0 n A V_S}{V_C} \frac{dM_z(t)}{dt} = -\mu_0 \eta_C n A \frac{dM_z(t)}{dt}, \quad (\text{C.16})$$

where V_S is the sample volume and $\eta_C = V_S/V_C$ is the filling factor of the sample in the detection coil¹. The index C is given to avoid confusion with the filling factor η of the sample in the resonator. In an experiment with amplitude modulation of the mw field, we can calculate the signal, in a first step without considering the noise \mathcal{N} , by inserting Eq. (C.7) in Eq. (C.16),

$$S = 0.25 \mu_0 Q_\Xi \omega_\Xi n A \eta_C a_0 M_0 = 0.25 \sqrt{\mu_0 L V_C} Q_\Xi \omega_\Xi \eta_C a_0 M_0. \quad (\text{C.17})$$

The constant factors have not been merged up to now to allow for a quantitative estimation of the minimum number of detectable spins later.

¹We get this simple relationship for η_C because of the assumption that the magnetic field produced by a current in the coil being constant over V_C .

C.3 Detector Noise

To determine the noise of the circuit, its parallel impedance is needed which can be calculated with good accuracy as a shunt resistance

$$R_P = Q_{\Xi}\omega_{\Xi}L. \quad (\text{C.18})$$

The Johnson noise, the main noise source at the terminals of the coil, in the frequency interval $\Delta\nu$ is now

$$\mathcal{N} = \sqrt{4kT\Delta\nu R_P} = \sqrt{4kT\Delta\nu Q_{\Xi}\omega_{\Xi}L}. \quad (\text{C.19})$$

When using a PSD for detection, $\Delta\nu = 1/\pi\tau_{\text{PSD}}$ is its bandwidth (fwhh), where τ is the filter time constant. To obtain the noise that is finally detected at the output of the PSD, the effect of the voltage follower and the preamplifier have to be considered as well. This can be done by simply inserting the noise figure F in Eq. (C.19) for each device. In a cascade of n electronic devices, each having a gain G_i and its own characteristic noise figure F_i , the total noise figure is given by

$$F = F_1 + \frac{F_2 - 1}{G_1} + \frac{F_3 - 1}{G_1 G_2} + \cdots + \frac{F_n - 1}{G_1 G_2 \cdots G_{n-1}}. \quad (\text{C.20})$$

It is easily seen that the noise figure of devices late in the chain can usually be neglected because they are divided by the product of the gains of all the previous devices. In our case, we have to consider the noise figure of the voltage follower F_{VF} and, because the voltage follower has a gain $G_{\text{VF}} = 1$, the noise figure of the rf preamplifier F_{PA} . The complete formula for the noise is

$$\mathcal{N} = \sqrt{4kT\Delta\nu Q_{\Xi}\omega_{\Xi}LF}. \quad (\text{C.21})$$

C.4 Signal-to-Noise Ratio

Eqs. (C.17) and (C.21) can now be combined to give a complete formula for the signal-to-noise (S/N) ratio ψ of this detection setup in a cw LOD EPR experiment with amplitude modulation of the mw field. We obtain

$$\psi = \frac{S}{\mathcal{N}} = \sqrt{\frac{\mu_0 V_C Q_{\Xi} \omega_{\Xi}}{64kT\Delta\nu F}} \eta_C a_0 M_0. \quad (\text{C.22})$$

We can rewrite this formula by using the relationship (2.13) as

$$\begin{aligned} \psi &= \frac{Ng^2\beta_e^2 B_0 \eta_C a_0 S(S+1)}{3kV_S T_S} \sqrt{\frac{\mu_0 V_C Q_{\Xi} \omega_{\Xi}}{64kT\Delta\nu F}} \\ &= \frac{\sqrt{\mu_0} \beta_e \hbar}{24k^{3/2}} \frac{Ng\omega_{mw} a_0 S(S+1)}{T_S} \sqrt{\frac{Q_{\Xi} \omega_{\Xi}}{T\Delta\nu V_C F}}. \end{aligned} \quad (\text{C.23})$$

The sample temperature T_S is not necessarily equal to the temperature T of the detection circuit, especially if parts of the detector are at room temperature.

References

- [1] N. BLOEMBERGEN and R. DAMON, *Phys. Rev.* **85**, 699 (1952).
- [2] G. WHITFIELD and A. REDFIELD, *Phys. Rev.* **106**, 918 (1957).
- [3] J. HERVÉ and J. PESCIA, *C. R. Ac. Sci. Paris* **251**, 665 (1960).
- [4] A. BASSOMPIERRE and J. PESCIA, *Compt. Rend.* **254**, 4439 (1962).
- [5] H. HERVÉ. *Paramagnetic Resonance*, page 689. Academic Press, San Diego, 1963.
- [6] J. PESCIA, *Ann. Phys.* **10**, 389 (1965).
- [7] P. LOPEZ and J. PESCIA, *Phys. Lett.* **38A**, 109 (1972).
- [8] G. ABLART, J. PESCIA, S. CLEMENT, and J. RENARD, *Solid State Commun.* **45**, 1027 (1983).
- [9] H. LEVANON, C. KWAN, and S. WEISSMAN, *Chem. Phys. Lett.* **6**, 19 (1970).
- [10] P. BUCCI, M. MARTINELLI, and S. SANTUCCI, *J. Chem. Phys.* **53**, 4524 (1970).
- [11] F. CHIARINI, M. MARTINELLI, L. PARDI, and S. SANTUCCI, *Phys. Rev. B* **12**, 847 (1975).
- [12] M. GIORDANO, M. MARTINELLI, L. PARDI, and S. SANTUCCI, *J. Phys. C: Solid State Phys.* **11**, 893 (1978).
- [13] A. SCHWEIGER and R. ERNST, *J. Magn. Reson.* **77**, 512 (1988).
- [14] I. NICHOLSON, F. ROBB, and D. LURIE, *J. Magn. Reson. B* **104**, 284 (1994).
- [15] A. SCHWEIGER and G. JESCHKE, *Principles of Pulse Electron Paramagnetic Resonance*. Oxford University Press, Oxford, 2001.
- [16] C. POOLE, *Electron Spin Resonance - A Comprehensive Treatise on Experimental Techniques*. John Wiley & Sons, New York, Second Edition, 1983.

- [17] L. BANCI, I. BERTINI, and C. LUCHINAT, *Nuclear and Electron Relaxation*. VCH, Weinheim, 1991.
- [18] C. PINZINO. *Foundations of Modern EPR*, page 758. World Scientific, Singapur, 1998.
- [19] R. KIRMSE and J. STACH, *ESR-Spektroskopie - Anwendungen in der Chemie*. Akademie-Verlag, Berlin, 1985.
- [20] A. ABRAGAM, *Principles of Nuclear Magnetism*. Oxford University Press, Oxford, 1961.
- [21] F. KNEUBÜHL, *Repetitorium der Physik*. B.G. Teubner, Stuttgart, 1994.
- [22] R. ERNST, G. BODENHAUSEN, and A. WOKAUN, *Principles of Nuclear Magnetic Resonance in One and Two Dimensions*. Clarendon Press, Oxford, 1987.
- [23] R. KARPLUS and J. SCHWINGER, *Phys. Rev.* **73**, 1020 (1948).
- [24] A. ASTASHKIN and A. SCHWEIGER, *Chem. Phys. Lett.* **174**, 595 (1990).
- [25] S. STOLL, G. JESCHKE, M. WILLER, and A. SCHWEIGER, *J. Magn. Reson.* **130**, 86 (1998).
- [26] J. HORNAK and J. FREED, *J. Magn. Reson.* **67**, 501 (1986).
- [27] G. JESCHKE. *New Concepts in Solid-State Pulse Electron Spin Resonance*. PhD thesis, ETH Zürich, No. 11873, 1996.
- [28] C. POOLE and H. FARACH, *Relaxation in Magnetic Resonance*. Academic Press, New York, 1971.
- [29] K. STANDLEY and R. VAUGHAN, *Electron Spin Relaxation Phenomena in Solids*. Hilger, London, 1969.
- [30] A. REDFIELD, *Phys. Rev.* **98**, 1787 (1955).
- [31] F. BLOCH, *Phys. Rev.* **70**, 460 (1946).
- [32] L. SINGER and J. KOMMANDEUR, *J. Chem. Phys.* **34**, 133 (1961).
- [33] J. LLOYD and G. PAKE, *Phys. Rev.* **92**, 1576 (1953).
- [34] N. BLOEMBERGEN and S. WANG, *Phys. Rev.* **93**, 72 (1954).
- [35] V. LIVSHITS, T. PÁLI, and D. MARSH, *J. Magn. Reson.* **134**, 113 (1998).
- [36] W. BECK, J. INNES, J. LYNCH, and G. BRUDVIG, *J. Magn. Reson.* **91**, 12 (1991).
- [37] J. HYDE. *Time-Domain Electron Spin Resonance*, page 1. Wiley, New York, 1979.

- [38] S. WEISSMANN, G. FEHER, and E. GERE, *J. Am. Chem. Soc.* **79**, 5584 (1957).
- [39] J. CASTLE, P. CHESTER, and P. WAGNER, *Phys. Rev.* **119**, 953 (1960).
- [40] T. WACKER, G. SIERRA, and A. SCHWEIGER, *Isr. J. Chem.* **32**, 305 (1992).
- [41] S. DUZBA, Y. KODERA, H. HARA, and A. KAWAMORI, *J. Magn. Reson. A* **102**, 257 (1993).
- [42] J. HYDE, W. FRONCISZ, and C. MOTTLEY, *Chem. Phys. Lett.* **110**, 621 (1984).
- [43] R.-A. EICHEL. *New concepts in two-dimensional pulse electron paramagnetic resonance spectroscopy*. PhD thesis, ETH Zürich, 2001.
- [44] F. CHIARINI, M. MARTINELLI, P. ROLLA, and S. SANTUCCI, *Phys. Lett.* **44A**, 91 (1973).
- [45] J. HYDE, P. SCZANIECKI, and W. FRONCISZ, *J. Chem. Soc. Faraday Trans. 1* **85**, 3901 (1989).
- [46] A. D. GIACOMO and S. SANTUCCI, *Nuovo Cimento* **63B**, 407 (1969).
- [47] J. SHIRLEY, *Phys. Rev. B* **138**, 979 (1965).
- [48] P. BUCCI and S. SANTUCCI, *Phys. Rev. A* **2**, 1105 (1970).
- [49] P. BUCCI, P. CAVALIERE, and S. SANTUCCI, *J. Chem. Phys.* **52**, 4041 (1970).
- [50] J. DAVIES, *Solid State Commun.* **20**, 433 (1976).
- [51] M. MARTINELLI, L. PARDI, C. PINZINO, and S. SANTUCCI, *Phys. Rev. B* **16**, 164 (1977).
- [52] M. GIORDANO, D. LEPORINI, M. MARTINELLI, L. PARDI, S. SANTUCCI, and C. UMETON, *J. Chem. Phys.* **88**, 607 (1988).
- [53] F. MOMO, A. SOTGIU, and R. ZONTA, *J. Phys. E* **15**, 893 (1982).
- [54] R. DAMON, *Rev. Mod. Phys.* **25**, 239 (1953).
- [55] G. ABLART and J. PESCIA, *Phys. Rev. B* **22**, 1150 (1980).
- [56] T. SATO, H. YOKOYAMA, H. OHYA, and H. KAMADA, *Appl. Magn. Reson.* **16**, 33 (1999).
- [57] T. STRUTZ, A. WITOWSKI, R. DE BEKKER, and P. WYDER, *Appl. Phys. Lett.* **57**, 831 (1990).
- [58] A. COLLIGIANI, M. LUCCHESI, and M. MARTINELLI, *Acta Medica* **22**, 251 (1990).
- [59] J. PESCIA. *Foundations of Modern EPR*, page 758. World Scientific, Singapur, 1998.

- [60] F. CIANFLONE, F. FRANZIA, and D. LEPORINI, *J. Magn. Reson.* **131**, 86 (1998).
- [61] D. LEPORINI, *Phys. Rev. A* **49**, 992 (1994).
- [62] I. PANAGIOTELIS, I. NICHOLSON, and J. HUTCHISON, *J. Magn. Reson.* **149**, 74 (2001).
- [63] V. ATSARKIN, V. DEMIDOV, and G. VASNEVA, *Phys. Rev. B* **52**, 1290 (1995).
- [64] V. ATSARKIN, V. DEMIDOV, and G. VASNEVA, *Appl. Magn. Reson.* **15**, 323 (1998).
- [65] M. GIORDANO, M. MARTINELLI, L. PARDI, S. SANTUCCI, and C. UMETON, *Solid State Commun.* **52**, 423 (1984).
- [66] M. GIORDANO, M. MARTINELLI, L. PARDI, S. SANTUCCI, and C. UMETON, *J. Magn. Reson.* **64**, 47 (1985).
- [67] A. COLLIGIANI, D. LEPORINI, M. LUCCHESI, and M. MARTINELLI. *Electron magnetic resonance of disordered systems*, page 16. World Scientific, 1991.
- [68] M. MARTINELLI, L. PARDI, C. PINZINO, and S. SANTUCCI, *Solid State Commun.* **17**, 211 (1975).
- [69] D. BOURDEL, F. RUIZ, G. ABLART, J. PESCIA, S. CLEMENT, and J. RENARD, *Solid State Commun.* **29**, 727 (1979).
- [70] B. VIGOUROUX, J. GOURDON, and J. PESCIA, *J. Phys. F* **6**, 1575 (1976).
- [71] G. RINARD, R. QUINE, J. HARBRIDGE, R. SONG, G. EATON, and S. EATON, *J. Magn. Reson.* **140**, 218 (1999).
- [72] H. YOKOYAMA, T. SATO, T. OGATA, H. OHYA-NISHIGUCHI, and H. KAMADA, *J. Magn. Reson.* **129**, 201 (1997).
- [73] H. YOKOYAMA, T. SATO, N. TSUCHIHASHI, T. OGATA, H. OHYA-NISHIGUCHI, and H. KAMADA, *Magn. Reson. Imag.* **15**, 701 (1997).
- [74] I. NICHOLSON, F. ROBB, S. MCCALLUM, A. KOPTIOUG, and D. LURIE, *Phys. Med. Biol.* **43**, 1851 (1998).
- [75] M. GIORDANO, M. MARTINELLI, L. PARDI, and S. SANTUCCI, *Mol. Phys.* **42**, 523 (1981).
- [76] S. STOLL, *Nutation-correlated EPR spectroscopy*. diploma thesis, ETH Zürich, 1996.
- [77] A. MARSHALL and F. VERDUN, *Fourier Transforms in NMR, Optical, and Mass Spectrometry*. Elsevier, Amsterdam, 1990.

- [78] D. HOULT and R. RICHARDS, *J. Magn. Reson.* **24**, 71 (1976).
- [79] Bruker Analytische Messtechnik GmbH, Karlsruhe. *ER Series User's Manual*, 1983.
- [80] A. SCHWEIGER, *J. Chem. Soc. Faraday Trans.* **91**, 177 (1995).
- [81] J. GRANWEHR, J. FORRER, and A. SCHWEIGER, *J. Magn. Reson.* **151**, 78 (2001).
- [82] R. BRAMLEY and J. STRACH, *Chem. Phys. Lett.* **79**, 183 (1981).
- [83] G. BORGIA, R. BROWN, and P. FANTAZZINI, *J. Magn. Reson.* **132**, 65 (1998).
- [84] W. PRESS, S. TEUKOLSKY, W. VETTERLING, and B. FLANNERY, *Numerical Recipes in C*. Cambridge University Press, Cambridge, Second Edition, 1992.
- [85] E. FORDHAM, A. SEZGINER, and L. HALL, *J. Magn. Reson.* **113A**, 139 (1995).
- [86] Y.-Q. SONG, L. VENKATARAMANAN, M. HÜRLIMANN, M. FLAUM, P. FRUNELLA, and C. STRALEY, *J. Magn. Reson.* **154**, 261 (2002).
- [87] R. BRÄNDLE, G. KRÜGER, and W. MÜLLER-WARMUTH, *Z. Naturforsch.* **25**, 1 (1970).
- [88] S. PFENNINGER. *Auflösungs- und Empfindlichkeitsverbesserung in der gepulsten EPR- und ENDOR-Spektroskopie*. PhD thesis, ETH Zürich, No. 9602, 1991.
- [89] J. FORRER, S. PFENNINGER, G. SIERRA, G. JESCHKE, A. SCHWEIGER, B. WAGNER, and T. WEILAND, *Appl. Magn. Reson.* **10**, 263 (1996).

Index

- B_1
 - cycle, 74
 - distribution, 58, 130
- Q_{Ξ} determination, 79
- T_1, T_2 , *see* relaxation time
- ω_{Ξ} determination, 79
- g factor, 7

- amplitude modulation, 27, 41, 52

- blind signal, 74, 110
- Bloch equations, 15
- Boltzmann distribution, 9
- boxcar averager, 58, 77

- coal sample, 88
- coherence, 10
- coil, 42, 55
- Cu(II), 96
- cw LOD EPR, 28, 97
 - excitation schemes, 37
 - setup, 52
 - signal-to-noise ratio, 62, 139

- data analysis, 76
- data collection, 58
- deadtime, 1, 25

- denoising, 82, 106
- detection
 - circuit, 29, 125
 - coil, 54
 - longitudinal, 2, 27
 - setup, 55
 - transverse, 2
- detection frequency, 93, 95
- detector, 43
 - noise, 139
 - sequence, 67
- diffusion, 19, 83
 - chemical reactions, 20
 - instantaneous, 19
 - spectral, 19
 - spin, 19
- dipole-dipole interaction, 8
- dolomite, 110, 114
- DPPH, 112, 114, 116

- effective field B_{eff} , 12
- ELDOR, 25
- electron Zeeman interaction, 8
- EPR measurements, 46
- ESEEM, 48
- exchange interaction, 8

- field sweep, 87
- Fredholm equation, 103
- Hamilton operator, 8
- harmonic oscillator, 29, 125
- Herasil, 91, 113
- Hervé-Pescia equation, 37
- hole burning, 24
- hyperfine interaction, 8

- imaging, 49
- inversion recovery, 23, 108
 - electron Zeeman resolved, 25
- IR-LOD T_1 , 109

- LCR circuit, 29
- line splitting, 90
- linewidth, 35
- lithium phtalocyanine, 93
- lock-in amplifier, 77
- longitudinal detection, 27
 - theoretical description, 30

- magnetic flux, 137
- magnetic induction, 137
- magnetic moment, 7
- magnetization, 9
 - time evolution, 13, 135
- master equation, 10
- matching, 56
- minimization algorithm, 101
- Mn(II)-doped NH_4Cl , 97
- moving average, 82, 106

- noise, 139
- nuclear quadrupole interaction, 8
- nuclear Zeeman interaction, 8
- number of spins, 63
- nutaton, 12
 - frequency, 12, 130
 - overdamped, 73
 - pulse, 69
 - transient, 61

- PEANUT, 130
- phase sensitive detector, 58
- pick-up coil, 42
- polarization measurement, 67
 - time resolved, 77
- probehead, 52
- PT-LOD EPR, 94
- pulse
 - high-turning angle, 69
 - ideal, 13
 - refocused nutation, 71
 - rotation angle, 13
 - train, 80
- pulse LOD EPR, 28
 - pulse-train excited, 94
 - setup, 52
 - transient-nutation excited, 87

- quantized field formalism, 31

- relaxation, 14
 - direct process, 17
 - longitudinal, 15

- Orbach process, 18
- phase-memory time T_m , 18
- Raman process, 17
- rotating frame, 15
- spin-lattice, 8, 14
- spin-spin, 14
- superoperator, 10
- temperature dependence, 17, 18
- transverse, 15, 18
- relaxation time, 14
 - determination of T_1 , 21
 - with cw LOD, 44
 - with pulse LOD, 43, 101
 - direct measurement, 116
 - distribution, 103
- resonant circuit, 55, 137
- resonator, 43
 - dielectric, 54, 130
- rotary echo, 70
- rotating frame, 11
- saturation, 12
 - factor, 13
 - methods, 21
 - recovery, 23, 108
- sensitivity, 62
- setup, 52
- shot repetition time, 64
- signal
 - B_1 dependence, 91
 - assuming fast relaxation, 34
 - assuming low modulation depth,
 - 38
 - dependence on saturation factor,
 - 35
 - LOD, 27
 - phase, 76
 - recording, 43, 75
 - signal-to-noise ratio, 62
 - simulation, 28
 - spectrometer, 52
 - spin, 7
 - bath, 20
 - temperature, 9
 - SR-LOD T_1 , 109
 - stimulated echo experiment, 24
 - stretched exponential, 102
 - TN-LOD EPR, 87
 - transient recorder, 57, 75
 - tuning, 55
 - voltage follower, 56
 - weight function, 132
 - zero-field splitting, 8

Acknowledgement

During my work at ETH, a large number of people helped me with their knowledge and experience, inspired me with their ideas, challenged me with their criticism, and shared their time with me not only during working hours. I would like to thank them for their support, their encouragement and their patience.

Prof. Dr. Arthur Schweiger, who suggested this project and made sure that it could be realized, for providing an excellent working environment, for his advice when I got stuck, and for not losing patience when not everything worked out fine right away.

Prof. Dr. Beat Meier for spontaneously agreeing to be co-examiner of this thesis, and for his very helpful comments.

Andreas Gehring, who showed me how to write publications and proposals for an audience with a different scientific background and different interests.

Carlos Calle for the enthusiasm to improve the computer service in the EPR group, for his private lesson on the W-band spectrometer, and for the proof that the only mess it requires to be productive is with computer cables.

Christoph Scheurer for getting the server fixed after I “added some features”, and for explaining me different system administration tasks.

Ferenc Simon for his critical remarks about the LOD setup.

Gunnar Jeschke for his advice in technical and theoretical questions, and for his feedback even after he had left ETH.

Gustavo Sierra to show me how to implement my own experiments on the home-built spectrometers and helping me every time I got stuck with one of these instrumental details. A special thank to him to inaugurate me into the subtleties of UNIX.

Igor Gromov for refloating more or less every electric device and identifying the weaknesses of any setup.

Jaap Shane for not just showing me how to use programs and spectrometers, but for patiently explaining me how they really work, where their limitations are and how to improve them.

Jeff Harmer who showed me how to analyze relaxation curves and how important it is to have an umbrella on a ski piste.

Jörg Forrer for introducing me into the secrets of EPR instrumentation, for building several “uuunglaubliche” setups (some of them really were), fixing things when I broke them, and explaining me the meaning of life.

Lorenz Liesum for teaching me about matched pulses and spin operators, for his help with the system administration, for many discussions about very general aspects of EPR, and for

being a great concert and opera guide.

Matthias Ernst for helping me with the server setup, for his troubleshooting when the network just did not work anymore, and for his application hosting service.

Michael Willer for explaining me very patiently the power of the spins, and for showing me how a spectrometer works and how to operate it.

Moritz “Sir Entropy” Kälin, my room mate in the new building, for answering all the small and not-so-small questions about science, economics, and MacOS, for showing me how bookkeeping works, for leaving a lot of messages from people who could not find me when I turned up late at the office, and for not caring about my uneven distribution of things on my desk – as long as I did not cross the border to his kingdom.

Peter Höfer from Bruker for very specific suggestions to improve the setup, and for discussions about his results with a similar setup, which helped me to get a better understanding of my own measurements.

Pol Schosseler, who taught me how to record cw EPR spectra and how to simulate them. He also showed me that sport – especially volleyball – is more important in life than EPR, and that EPR can be fun after all.

Rainer Bachmann for his LOD crash course, his suggestions for new or improved experiments with this detection technique, for caring about the X-band pulse spectrometer and for organizing all kinds of things for the benefit of the whole group.

Rüdiger Eichel for his help whenever I had a question about physics or some unusual computer problems that no one else even believed they exist, for having the beat, for his wild stunts on skis and board (“Wer kantet ist eine Memme”), and for not being frightened away by fire in the sky.

Sabine Van Doorslaer for helping to set up experiments and showing how to interpret EPR spectra, for not caring what the weatherman says when it comes to running or cycling, and for letting Ina rule the EPR group from time to time.

Stefan Stoll for the permission to use his PEANUT measurements of the dielectric ring resonator, for his help with simulation and with \LaTeX problems, and for keeping the cw spectrometer up and running.

Thomas Schulte-Herbrüggen, who allowed me to use his \LaTeX templates for my thesis.

Walter Lämmli for the literature service, for the maintenance of the chemistry lab where nothing was ever missing, and for reliably ordering and producing the chemicals needed for the experiments.

Yiqiao Song for performing some relaxation time analyses using Laplace inversion.

All the present and former members of the Schweiger group for many interesting conver-

sations, for their friendship, and for the great time we had together: Anna Ferretti, Cinzia Finazzo (for the best cappuccino at the Hönningerberg), Eric Hoffmann, Matthias Schuler, Rafail Rakhmatoulline, René Tschaggelar, Sophie Bonjour, and Zoltan Madi.

The electrical engineers Hansjürg Schmutz, Herbert Schmid, Jürg Keller, Markus Andrist, Paul Signer, Peter Nyffeler and Urban Meier for the teaching, the suggestions and the discussions of the different tasks of electronics I had to deal with during this work.

The mechanic engineers Willy Groth, Andreas Hunkeler, Bruno Lambillotte, Edi Peyer, Marco Vecellio and René Gunzinger for the precision work, for the uncomplicated troubleshooting, and for the flexible helium service.

And finally I would like to thank Andreas Arnold, Doris Kaufmann, Guido Grassi, Heinrich Willi, Irène Müller, Karl Burkhalter, Konrad Boss, Marie-Therese Werder, Markus Traber, Verena Baumann, and Walter Jaeggi for their continuous excellent service.

Curriculum Vitae

Personal Data

| | |
|---------------|-------------------|
| Name | Josef Granwehr |
| Date of Birth | December 24, 1971 |
| Citizen of | Gaiserwald, SG |
| Nationality | Swiss |

Education

| | |
|-------------|---|
| 1977 - 1983 | Primary School, Abtwil (SG) |
| 1983 - 1985 | Secondary School at the Katholische Kantons-Sekundarschule St. Gallen |
| 1985 -1992 | Grammar School at the Kantonsschule, St. Gallen |
| 1992 | Matura of type C (emphasis on mathematics and natural sciences) |

Studies

| | |
|-------------|--|
| 1992 - 1996 | Studies of chemistry, ETH Zürich |
| 1995 | Semester work on molecular dynamics in the group of Prof. W.F. van Gunsteren, supervised by P. Hünenberger |
| 1996 | Diploma thesis in physical chemistry, supervised by Prof. A. Schweiger and M. Willer |
| 1996 - 2001 | Ph.D. study in the research group of Prof. A. Schweiger in EPR spectroscopy, ETH Zürich |

Professional Experience

| | |
|-------------|---|
| 1996 - 2001 | System and network administration in the EPR working group at the Institute of Physical Chemistry, ETH Zürich |
| 1996 - 2001 | Teaching assistant in physical chemistry for lectures and laboratory courses, ETH Zürich |